Global Modeling and Assimilation Office
Annual Report & Research Highlights
2010-2011

NASA Goddard Space Flight Center ★ August 1, 2011

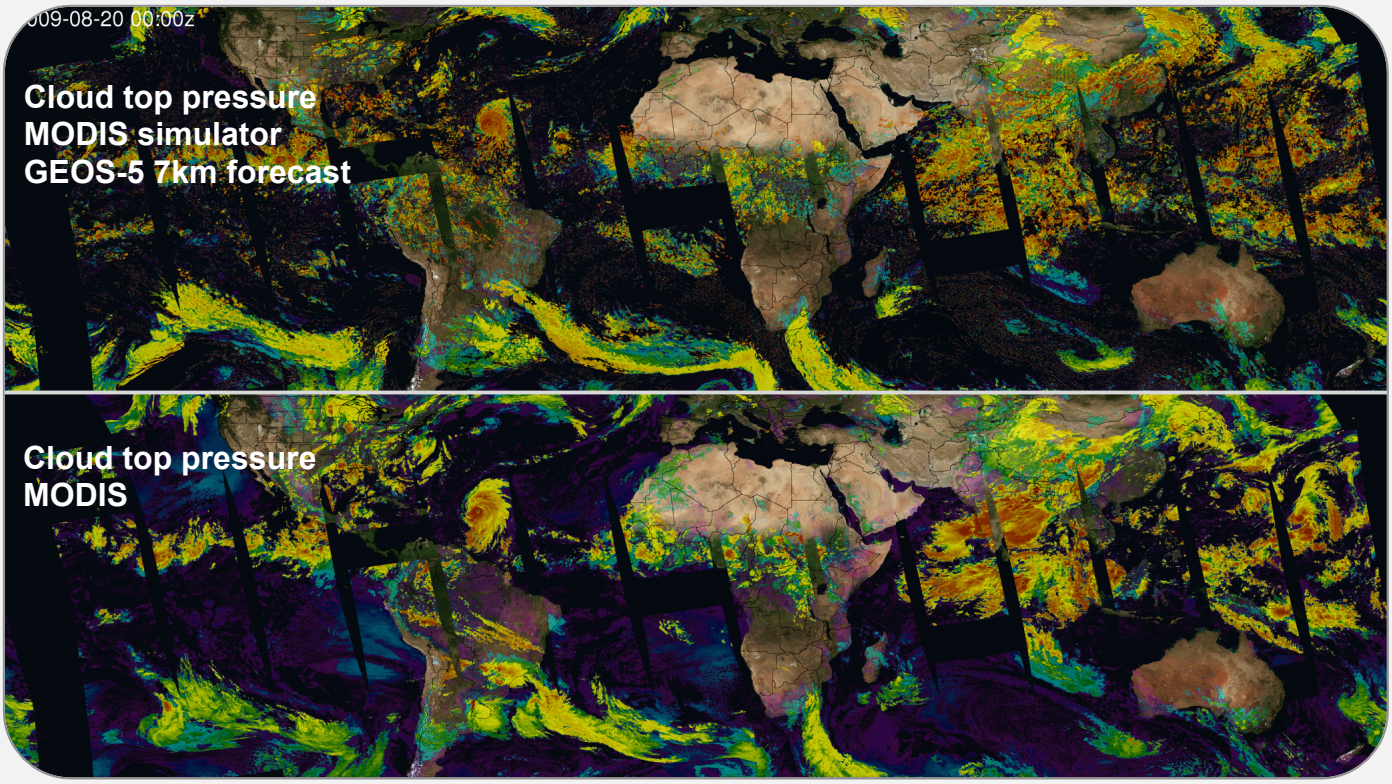

Table of Contents

January 2010 – June 2011 in review

During 2010-2011, the Global Modeling and Assimilation Office (GMAO) achieved significant advances in our GEOS-5-based systems, preparing for updated products for both weather and climate applications.

The successful collaboration with NOAA/NCEP in the development of the Gridpoint Statistical Interpolation (GSI) analysis has continued to be central to high quality products for NASA instrument teams and science groups who use GEOS-5 products. This year, we have made major contributions to GSI development, augmenting state and control vectors to support trace gases and aerosols, and ensuring that the evolution of the system will support 3DVar, 4DVar and a hybrid ensemble-variational assimilation.

While we have continued to use the GEOS-5 atmospheric data assimilation system (ADAS), version 5.2.0, at 1/2° × 2/3°× 72L for MERRA and products for NASA instrument teams, we have been advancing the 1/4° system that was first introduced in support of the Year of Tropical Convection (YOTC). One of our goals in these developments has been to improve the NWP skill score from our system and also to improve the simulation of tropical storms in readiness for our support of the Hurricane and Severe Storm Sentinel (HS3) Mission. Updates that incorporated the latest developments in the GSI allowed us to assimilate IASI and GPS-RO data, both of which made a substantial impact on the skill of 500 hPa forecasts. More recently data from the Advanced Scatterometer (ASCAT) on the MetOp satellite have been added. Developments have also allowed the real-time evaluation of observational impacts in the GEOS-5 system using the GEOS-5 ADAS adjoint tools. Of importance to many of the users of GEOS-5 data, the real-time aerosol products have continued to improve through the tuning and calibration of the biomass burning emissions from the Quick Fire Emission Dataset (QFED) that is derived from the MODIS Fire Radiative Power retrievals. This updated system, GEOS-5, version 5.7.2, will become the official production system in August 2011, with assimilated aerosol distributions provided alongside the regular meteorological products.

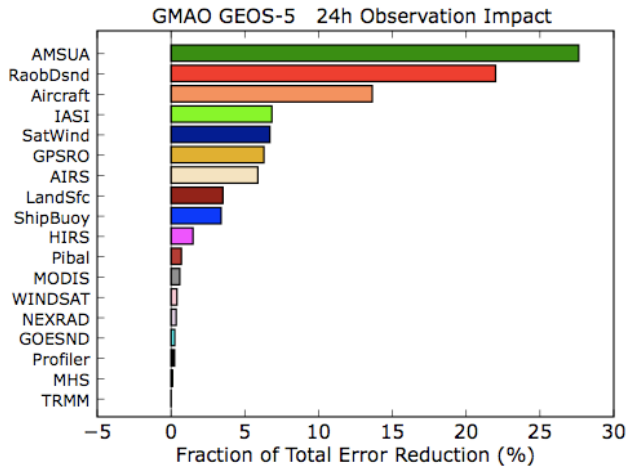

The adjoint of a data assimilation system provides a means of measuring the impact of observations on numerical weather forecasts. The figure here shows the overall impacts of the major observing systems assimilated in GEOS-5 in terms of their fractional contributions to the reduction of a global measure of 24-h forecast error over the period 10 Nov 2010 – 2 Jan 2011. The measure combines errors in wind, temperature and surface pressure with respect to the verifying analysis, in terms of energy per unit mass (J/kg). AMSU-A radiances have the largest overall impact, providing roughly 27% of the total error reduction due to the assimilation of all observations. Other observing systems known to be important for NWP, such as radiosondes and dropsondes (RaobDsnd), satellite winds and aircraft, also have large overall impacts.

The GEOS-5 analyses and forecasts, with aerosols and tagged tracers from regions of biomass burning, supported the Global Hawk Pacific (GloPac) field campaign in March 2010, the first Atmospheric Chemistry experiment with the Global Hawk. In August-September 2010, we then supported the Genesis and Rapid Intensification Processes (GRIP) experiment, a NASA Earth science field experiment conducted as a prelude to HS3 to better understand how tropical storms form and develop into major hurricanes. Augmenting our regular experimental weather forecast web pages, specialized sites, e.g.

http://gmao.gsfc.nasa.gov/projects/glopac/, were developed to support these field campaigns. In collaboration with the NASA Center for Climate Simulation (NCCS), GEOS-5 products have been made openly available on the NCCS data portal in addition to the regular access for NASA instrument teams through the Goddard Earth Sciences Data and Information Services Center (GES DISC).

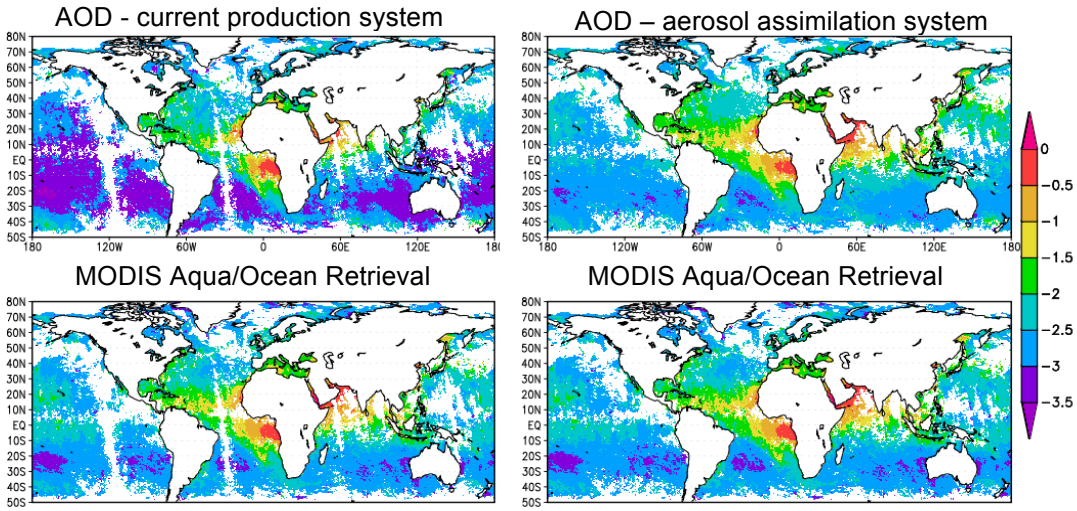

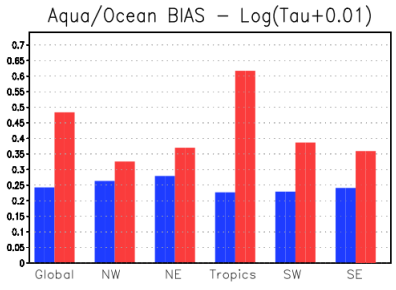

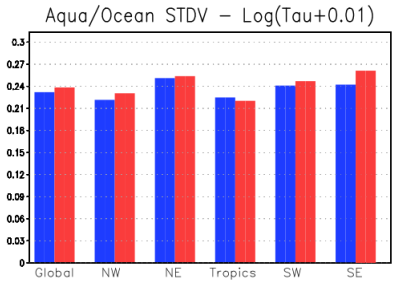

Innovation statistics from the current production

Innovation statistics from the aerosol assimilation

The aerosol data assimilation system has reached a level of maturity that it is now being tested for possible inclusion in an update to the current GEOS-5.7.2 production system. In the production system, aerosol distributions are determined by surface emissions and then subsequent transport in the coupled GEOS-5-GOCART model. Surface emissions for dust and sea-salt are dynamic, depending on the model's current surface winds. Biomass burning emissions are provided by the Quick Fire Emission Dataset (QFED), which is derived from MODIS Fire Radiative Power retrievals. The real-time aerosol products, which have been provided since spring of 2008 when GMAO supported the ARCTAS field campaign, have continued to improve through the tuning and calibration of these biomass-burning emissions. The realism is apparent in the plots of the assimilation variable, log(AOD+0.01), where AOD is the aerosol optical depth. The left-hand plots are from the production system and from MODIS on Aqua. The right-hand upper plot is from the assimilation system. The statistics of bias and standard deviation of the innovations show that the improvement in the assimilation product comes primarily from a reduction in the bias.

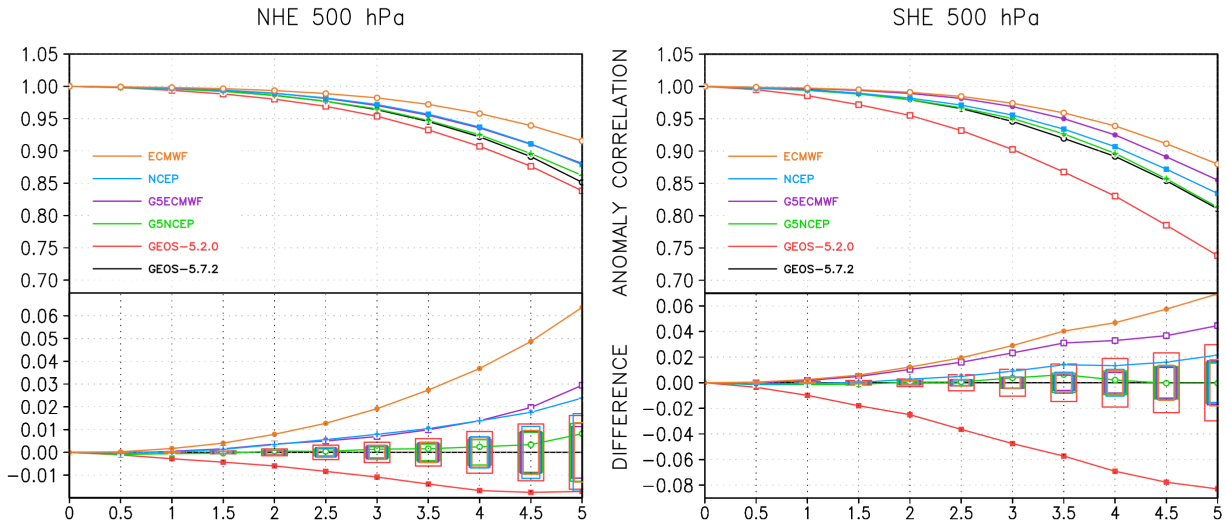

Our work to increase GEOS-5's NWP skill score has involved adding additional observations, especially GPSRO, tuning the background error statistics, and tuning some of the model moist physics parameterizations. As part of the process of looking at both model and analysis issues, we have also run forecasts initialized with analyses from both ECMWF and NCEP (denoted G5ECMWF and G5NCEP in the figures above). The above figures show the forecast skill measured by the 500 hPa height anomaly correlation for the Northern and Southern Hemisphere extratropics (left and right figures, respectively) in April 2011. The lower section of the plots is used to identify statistical significance. Any curve outside its colored bounding box is significantly different from the reference forecast (here the latest GEOS-5 system, GEOS-5.7.2) at the 95% level. In addition to the GEOS-5 forecasts, we show the latest systems from ECMWF and NCEP (GFS). Although the GEOS-5 forecast skill is lower than those centers, the skill has improved markedly over that from the previous production system, GEOS-5.2.0, which was used for MERRA.

Production of the GMAO's Modern-Era Retrospective Analysis for Research and Applications (MERRA) has continued, with products released only a few weeks behind real time. As of the end of June 2011, users had downloaded over 660 TB of data from the GES DISC. Monthly mean data have also been prepared for publication through the Earth System Grid node in the NCCS to facilitate the availability of MERRA data for model evaluations anticipated for the Fifth Assessment Report of the IPCC. A special collection of MERRA papers has been organized in the Journal of Climate, with many of the papers already available online at http://journals.ametsoc.org/page/MERRA.

An online atlas of climatological information from MERRA, including comparisons of basic climatological variables with data-only products and other reanalyses, is being maintained at http://gmao.gsfc.nasa.gov/ref/merra/atlas/. In addition to the MERRA atlas, we are also developing a more experimental atlas of climate and weather extremes for the Americas that focus on the tails of the distribution. The atlas includes such quantities as the number of extreme rainy days, the length of dry spells, and the standardized precipitation index at various time scales. The results from MERRA are compared with NOAA's recent Climate Forecast System Reanalysis (CFSR) and various station observations. This atlas, available at http://gmao.gsfc.nasa.gov/research/subseasonal/atlas/Extremes.html, is being developed as part of a VAMOS project on extremes, and involves participants from throughout the Americas.

MERRA has provided the basis for our approach of incremental development of an Integrated Earth System Analysis. Thus, MERRA-driven component reanalyses had been generated for the ocean and land surface to provide the initial conditions for our GEOS-5 seasonal- and decadal-forecast suite, and for ocean biology to provide air-sea flux estimates for the flux pilot project underway for the NASA Carbon Monitoring System project. The MERRA-Land reanalysis has corrected some of the deficiencies in the

land surface products from MERRA itself. As a prelude to performing coupled assimilations of atmospheric constituents and meteorology, MERRA analyses have been used to drive atmospheric chemistry and aerosol computations in GEOS-5. Now, a MERRA-Aerosol mini-reanalysis for 2007-2010 has been completed and a stream for 2003-2006 is underway. Results are being analyzed using a variety of satellite observations, some of which will be assimilated in conjunction with the physical atmospheric state in future versions of GEOS-5.

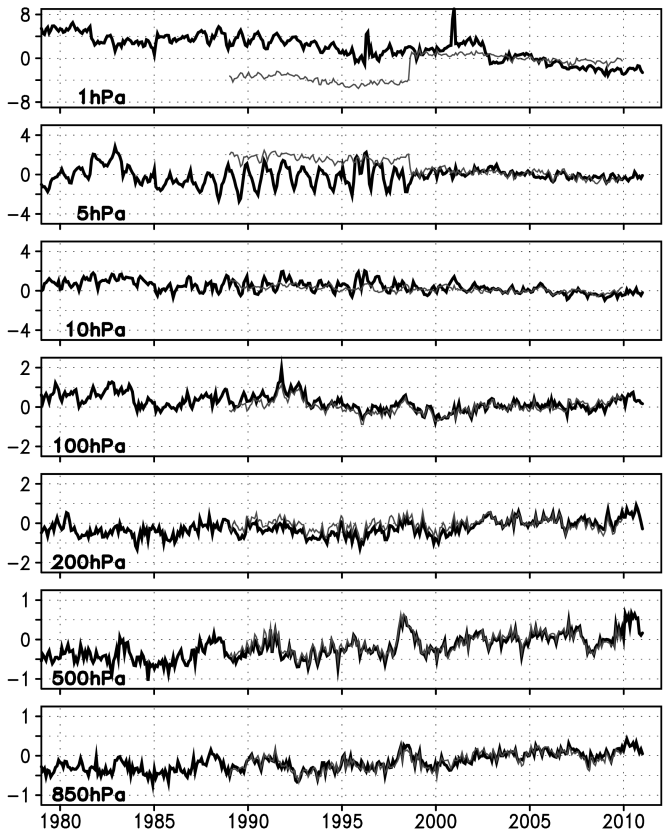

MERRA was undertaken by GMAO to place observations from NASA's Earth Observing System satellites in a climate context and to improve upon the hydrologic cycle represented in earlier generations of reanalyses. The papers in the MERRA Special Collection in the *Journal of Climate* evaluated the products from the viewpoint of several different applications. They also compared MERRA with other updated reanalyses (ERA-Interim and CFSR) to identify advances made in this new generation of reanalyses, as well as remaining deficiencies. We found that although there is little difference between the new reanalyses in many aspects of climate variability, substantial differences remain in poorly constrained quantities such as precipitation and surface fluxes. However, the latest reanalyses, including MERRA, do improve substantially upon the precipitation in the previous reanalyses. We also found that all reanalyses are still sensitive to observing system changes. Dealing with this sensitivity remains the most pressing challenge for the next generation of reanalyses. At left is a comparison of global mean temperature anomalies from MERRA (thick line) and ERA-Interim (thin line), computed relative to the 2000-2010 annual cycle for each.

The GEOS ocean data assimilation system, with a linked sea-ice assimilation system, has matured significantly over this past year. Ocean-ice reanalyses from 1960 to 2011 have been generated using an ensemble-based system in which the background fields are specified by integrating the GEOS-5 Atmosphere-Ocean General Circulation Model (AOGCM) with the atmosphere constrained by the MERRA fields. The GEOS-5 AOGCM includes the Modular Ocean Model, Version 4 (MOM4), developed at GFDL, and the Los Alamos sea-ice Model (CICE). These states are now being used to initialize seasonal predictions and decadal predictions that we will contribute to NOAA's National Multi-Model Ensemble (NMME) and decadal predictions that we will contribute to the Coupled Model Intercomparison Project Phase 5 (CMIP5).

Substantial progress has also been made in the GEOS land data assimilation system, with the assimilation of soil moisture, snow and GRACE terrestrial water storage. In particular, our snow assimilation research demonstrated that it is possible to improve fine scale estimates of snow amounts through the assimilation of coarse-scale satellite observations with a distributed ensemble Kalman filter. GMAO continues to lead

the development and implementation of the Level 4 Surface and Root Zone Soil Moisture product for the NASA Soil Moisture Active Passive (SMAP) Mission with the merger of SMAP observations into the GEOS land data assimilation system.

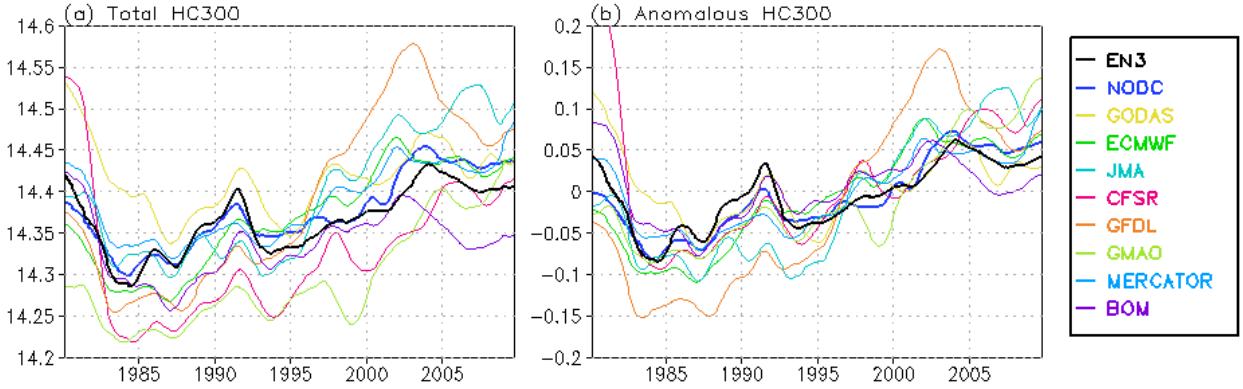

Upper ocean heat content (HC) is one of the key indicators of climate variability on many time-scales extending from seasonal to interannual to long-term climate trends. For example, HC in the tropical Pacific provides information on thermocline anomalies that is critical for the long-lead forecast skill of ENSO. The OceanObs09 Conference called for an intercomparison of ocean reanalyses (ORAs) to identify deficiencies in data assimilation schemes, and to provide a basis for development of real-time multi-model ensemble HC monitoring products. The GMAO GEOS ocean reanalysis was contributed to the ORA comparison conducted by NOAA/NCEP. Here we show the global average heat content, and corresponding interannual anomalies, in the upper 300 m of the ocean from 70°S to 70°N from the GMAO ocean analysis and other recent ocean reanalyses that are contributing to an ensemble of climate indices assembled by NOAA/NCEP.

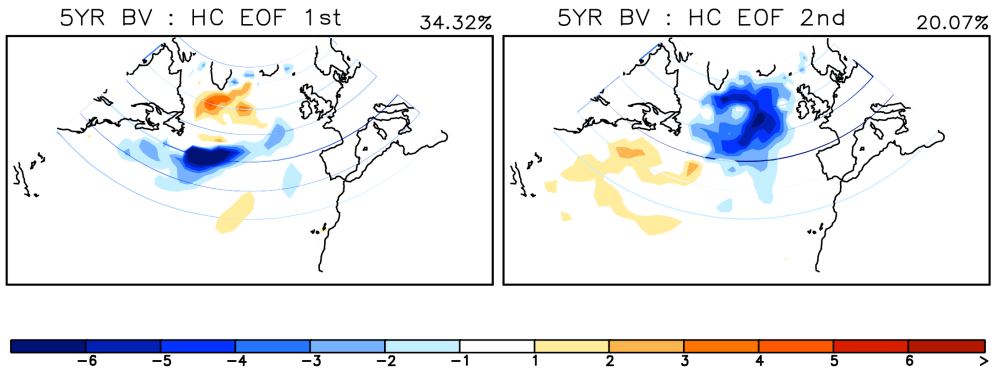

With the decadal prediction experiments, we are looking for predictability that arises from the internal variability rather than from climate trends. Climate variability on decadal timescales is strongly influenced by the ocean. One suspected source of decadal predictability is the Atlantic Meridional Overturning Circulation. The structures of the dominant EOFs of heat content in the upper 500 m of the North Atlantic Ocean from 5-year breeding simulations with the GEOS-5 AOGCM contain significant variance in the regions that relevant to multi-decadal variations in the Atlantic Meridional Overturning Circulation.

Advances have been made on many aspects of the GEOS-5 modeling system. In addition to the tuning of the moist physics modules to improve weather and climate simulations, including direct aerosol forcing, a stochastic Tokioka implementation of the convective parameterization was introduced to improve the

representation of the intensity and structure of tropical storms. The GEOS-5 AOGCM was enhanced with the CICE sea-ice model and routing of river runoff to the ocean. Simulations of the current climate demonstrate that the system is state of the art. A strategy is now being tested for generation of perturbations for ensemble climate predictions. The strategy, based on breeding for both seasonal and decadal timescales, appears to generate meaningful perturbations. The full CMIP5 decadal prediction suite is now underway, as are the retrospective forecasts needed for seasonal forecasts.

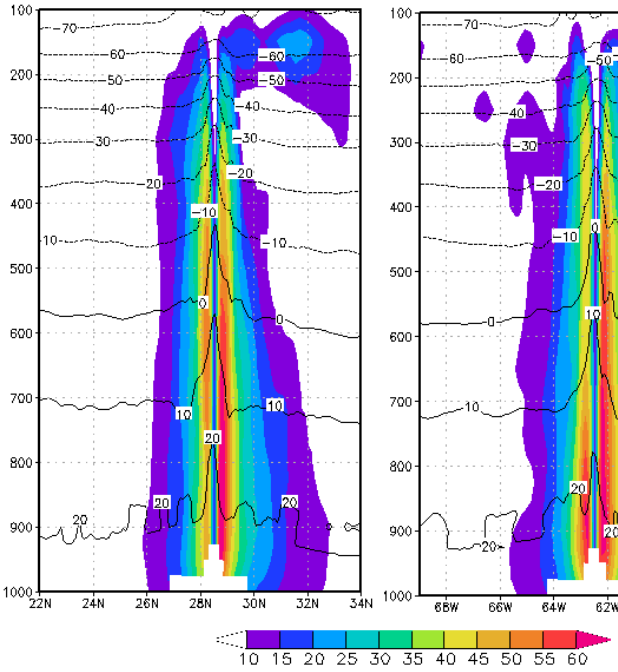

One of the areas of focus for the high-resolution versions of GEOS-5 is a better representation of tropical storms, both for the purposes of numerical weather prediction and also to support studies of weather-climate interactions. The figures to the left show the typical structure of tropical Atlantic hurricanes in a cube sphere simulation of approximately 10 km resolution. The left-hand figure shows the structure across 62.5°W and the right-hand figure the structure across 28.5°N. In addition to this realistic vertical structure, the Atlantic tropical storms display very realistic banded divergence and upper-level anticyclonic flow. [*Figures courtesy of Oreste Reale*] Simulations at 14 km have been used to look at the impact of climate variability on Atlantic hurricanes and show that this version of the model, forced by observed SST, is able to simulate the differences in tropical storm number and intensity between 2005 and 2006.

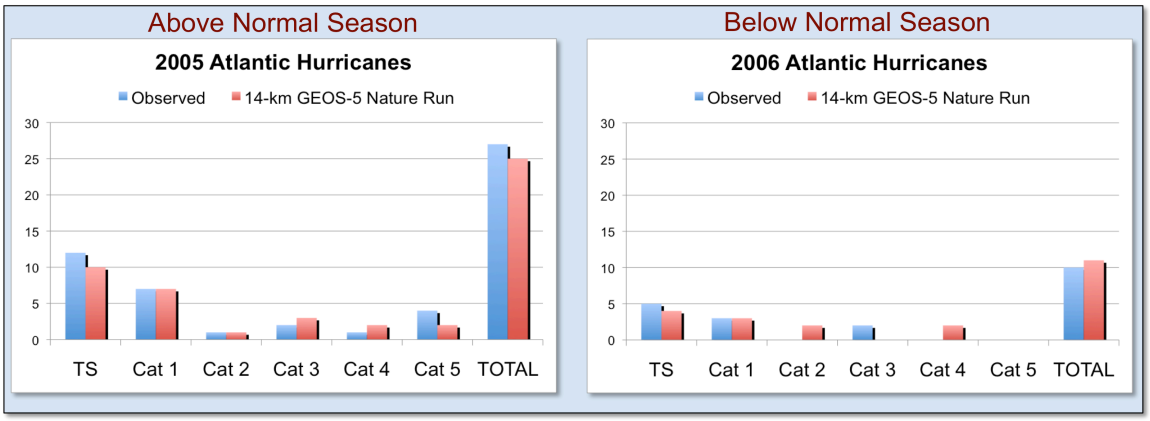

Other significant modeling developments have been in very high-resolution (cloud-permitting) global simulation capability and in an aerosol-cloud microphysics component that facilitates computation of aerosol indirect effects, both part of our strategy for the next-generation, non-hydrostatic system, GEOS-6. These developments have benefited from NASA's A-Train observations to evaluate the implementations and guide the tuning. In collaboration with NOAA/GFDL, the non-hydrostatic, cube-

sphere version of the finite volume dynamical core has been coupled to the other GEOS-5 components. Global simulations have been conducted at resolutions down to 3.5 km, with simulations of several years at 10 km. Simulations at 14 km have been used to look at the impact of climate variability on Atlantic hurricanes and show that this version of the model, forced by observed SST, is able to simulate the differences in tropical storm number and intensity between 2005 and 2006.

The current seasonal forecast system, based on the previous CGCMv1, successfully predicted La Niña conditions with the correct amplitude in the Fall of 2010 from forecasts initialized as early as March 2010. The tendency towards a recovery in early 2011 was predicted as early as the April 2010 forecast. Forecasts from early 2011 predicted El Niño conditions in the latter half of 2011. These have so far failed to emerge, showing that challenges still remain in seasonal climate prediction.

Other applications during this period have included attribution studies for the February 2010 snowstorm over the U.S. East Coast. Ensembles of simulations for winter 2010, designed to isolate the role of the North Atlantic SST versus that of the El Niño conditions that were present in the eastern Pacific, indicate that the 2010 anomalies over the U.S. were to a large extent driven by El Niño. The impact of the North Atlantic SST was primarily to contribute to the cooler temperatures along the U.S. east coast.

GMAO has participated in the flux pilot project of NASA's Carbon Monitoring System. In this pilot project, MERRA fields were used alongside satellite observations to constrain model estimates of marine and terrestrial carbon fluxes; these fluxes, alongside estimates of fossil-fuel and biomass-burning emissions, were then used as boundary conditions for GEOS-5 simulations. Evaluating the resultant CO_2 distributions with in-situ and space-based observations provides insight on atmospheric transport processes in nature and importantly on the internal consistency of the data-constrained flux estimates, which provides us with a stringent evaluation tool for coupled carbon models. Comparisons with in situ data showed that GEOS-5 is able to reasonably reproduce the seasonal cycle of CO_2 observed at remote surface stations; however, modeling observed diurnal variations remains a challenge. Work is ongoing to identify the role of specific processes involved and understand the relative roles of transport and flux uncertainty. This inter-center collaborative project helps GMAO contribute to preparations for NASA's future carbon observations, such as the Orbiting Carbon Observatory Version 2 (OCO-2) and the Active Sensing of CO_2 over Nights, Days and Seasons (ASCENDS) missions

Following are more detailed presentations of some of the research highlights from this period.

The Impact of Observation Interferences on the Assimilation of AIRS

Wei Gu and Ricardo Todling

Observations from the Atmospheric Infrared Radiance Sounder (AIRS) have been available since mid-2002. Of the available 2378 channels, a carefully selected 281-channel set is processed for data assimilation and numerical weather prediction. GEOS-5 employed an even more restrictive 148-channel set in the Modern-Era Retrospective Analysis for Research and Application (MERRA), including 86 long-wave temperature, 48 water vapor and 14 short-wave temperature channels. We present a diagnostic tool to help evaluate how channel interference relates to overlap of the Jacobians calculated in the assimilation of satellite radiances. The tool calculates *information content*, defined simply as the total error variance reduction due to the assimilation of observations scaled by the prescribed background error variance – a scaled version of the innovation error covariance projected back onto physical space via the background error covariance. In the case of AIRS observations, the information content can be partitioned into the components contributing to error reduction on temperature, specific humidity, and surface temperature on each model level due to each channel.

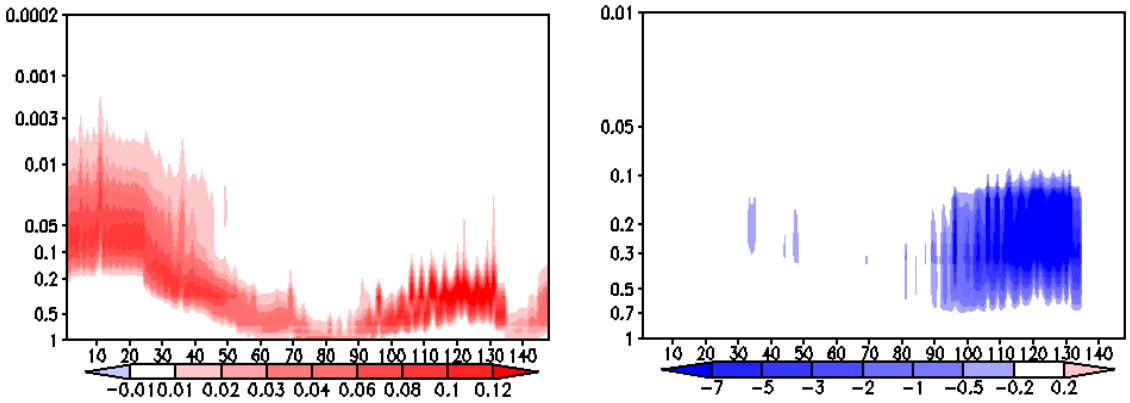

Figure 1: Profile-averaged temperature (left) and specific humidity (×10³) (right) Jacobians as a function of channel index and sigma level.

An illustration of the results is presented from evaluation of a GMAO operational analysis at 00 UTC on 13 May 2009. Figure 1 shows the averaged temperature (left) and specific humidity (right) Jacobians, representing radiance sensitivities with respect to each of these fields, as a function of channel index and vertical level, averaged over all 1231 AIRS clear-sky profiles available after quality control. The left-hand panel illustrates a typical situation of radiance observations from high-peaking temperature channels (1-48) having broader temperature sensitivities than those from low-peaking channels and near-surface temperature channels (49-86). Observations from water-vapor channels (87-132) have even larger temperature sensitivities than those from both long-wave (1-86) and short wave (133-148) temperature channels. The right-hand panel illustrates a typical situation of sensitivities with respect to specific humidity with the mid-to-high peaking water-vapor channels (92-132) having much larger sensitivities (on the order of 1000) than from other channels, including near-surface water vapor channels (87-91).

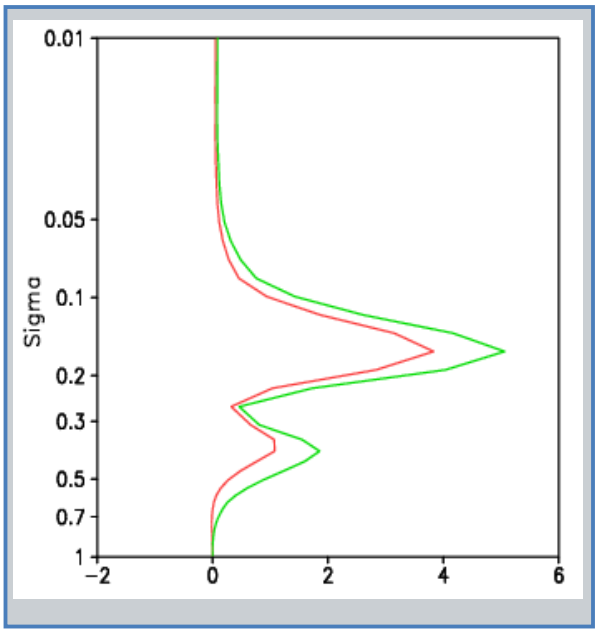

Figure 2: Profile-averaged fractional error reduction for temperature as a function of sigma level for when channel 27 is assimilated on its own (green curve) and for when it is assimilated with all other channels (red curve) (×10^{-5}).

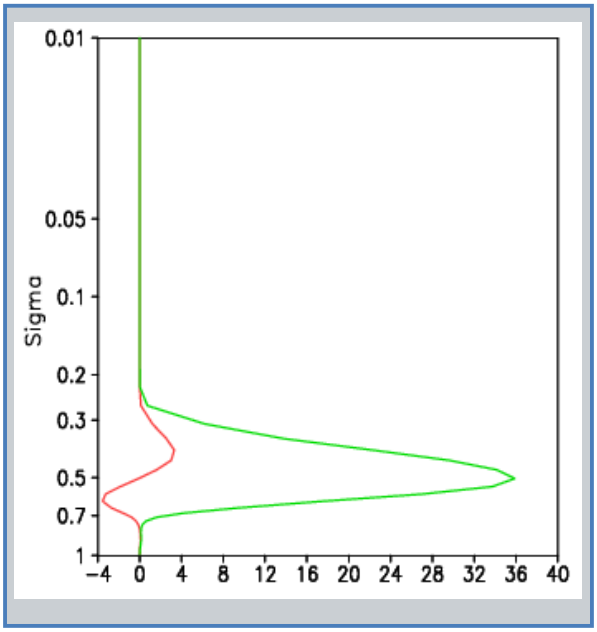

Figure 3: Same as Fig. 2, but for fractional error reduction of specific humidity from channel 128 (×10^{-5}).

Partitioning of the information content diagnostic allows definition of the fractional error reduction, i.e., the contribution of each channel to the analysis error reduction at each model level for each variable due to each AIRS channel. Figure 2 shows the profile-averaged fractional error reduction in the temperature field as a function of vertical level for channel 27 when it is assimilated in conjunction with all other channels (red curve), and when channel 27 is assimilated on its own (green curve). Both curves have relatively large positive values between levels 0.7 (700 hPa) to 0.1 (100 hPa), indicating the range of (positive) impact on the analyzed temperature field is similar. However, when all channels participate in the assimilation the various Jacobians (weighting functions) overlap with each other and result in a slight degradation of the error reduction (green curve). For temperature channels this small degradation is not significant. However, the situation is different for water-vapor channels.

Figure 3 shows the profile-averaged fractional error reduction in the specific humidity as a function of vertical level for channel 128. As before, the red curve shows the result when all other channels are assimilated together with channel 128, and the green curve shows the result when the channel is assimilated on its own. Here, there is clear improvement of the analysis (positive fractional error reduction) when channel 128 is assimilated by itself, but results are somewhat mixed when all channels are assimilated together. In the latter case, not only is the positive reduction smaller than in the former case, but there is also a negative contribution to the error reduction (between levels 0.7 to 0.5) not seen when the channel is assimilated alone. A detailed investigation has revealed that strong observation interferences from water vapor channels are due to large sensitivities in the radiances with respect to specific humidity, such as those seen in Figure 1 (right panel). Research is underway to reduce observation interferences for the various AIRS water-vapor channels by adjusting the background errors.

Measuring the Global Impact of ASCAT Observations

Ronald Gelaro

Near-surface wind vectors from the Advanced Scatterometer (ASCAT) on the MetOp satellite have been assimilated operationally in the global forecast system run by the Navy/FNMOC since July 2008 and, much more recently, in the global forecast systems run by NOAA/NCEP and NASA/GMAO since May 2011. A recent paper by Bi et al. (2011) describes the impact of these data in the NCEP Global Forecast System (GFS), based on observing system experiments (OSEs) with an earlier operational version of the GFS. Those authors found that assimilation of ASCAT observations slightly reduces the bias and standard deviation of the analyzed near-surface wind fields, and has a neutral or small positive impact on standard measures of forecast skill (e.g., anomaly correlation for 500 hPa height). Similar metrics produced with the GMAO system support these results.

The adjoint of a data assimilation system provides another means of measuring the impact of observations on numerical weather forecasts. Here we use the adjoint of GEOS-5 to examine the global impact of ASCAT winds on 24-h forecasts from 00 UTC during the period 10 Nov 2010 – 02 Jan 2011.

Figure 1a shows the overall impacts of the major observing systems assimilated in GEOS-5 in terms of their fractional contributions to the reduction of a global measure of 24-h forecast error. The measure combines errors in wind, temperature and surface pressure with respect to the verifying analysis, in terms of energy per unit mass (J/kg). The results show that AMSU-A radiances, which are both numerous and of known high quality, have the largest overall impact, providing roughly 27% of the total error reduction due to the assimilation of all observations. Other observing systems known to be important for NWP, such as radiosondes and dropsondes (RaobDsnd), satellite winds and aircraft, also have large overall impacts. In comparison, ASCAT winds provide a much smaller fraction (~2%) of the total error reduction. Because the current adjoint forecast model does not include moist physics, the impacts of moisture-related observations (e.g., from MHS and TRMM) are likely under-represented in these results. Nonetheless, the results in Figure 1a are consistent with our general knowledge of observing system impacts obtained from previous studies, and with the results reported by Bi et al. (2011).

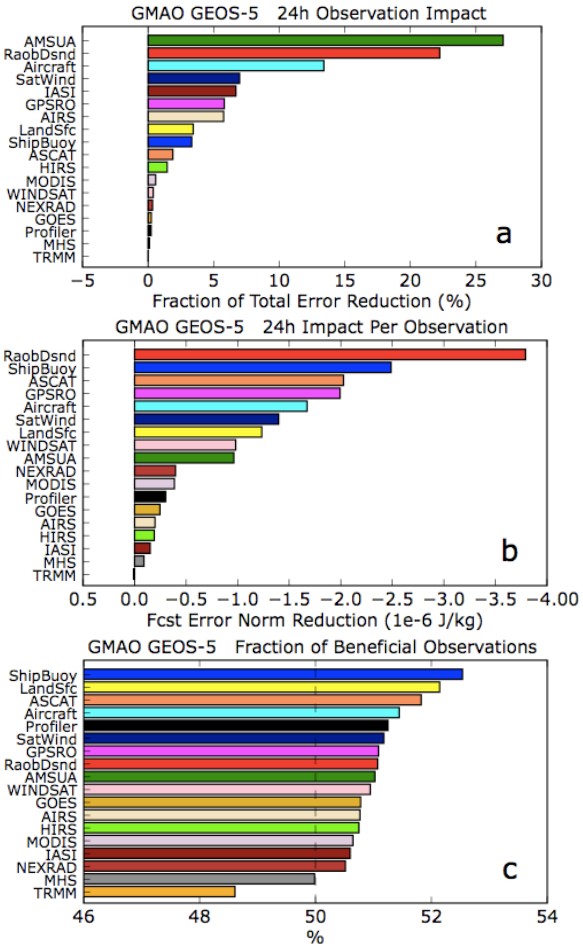

Figure 1: Impacts of various observation types on GEOS-5 24-hr forecasts from 00 UTC during the study period: (a) total impact, (b) impact per observation, and (c) fraction of beneficial observations.

There are far fewer observations from ASCAT (~17,000) assimilated in each GEOS-5 analysis than from, say, AMSU-A (~503,000) or radiosondes (~105,000). The impact per observation, shown in Figure 1b, provides a measure of the average influence of individual observations of a given type on the forecast. Results are expressed in terms of the average reduction in the error measure per observation, so that

negative values indicate a positive impact. Note that ASCAT winds provide one of the largest positive impacts per observation. A large impact per observation usually reflects the high quality of the observations, their location in otherwise data-sparse regions, or both. ASCAT observations also have one of the highest percentages of beneficial impacts, with roughly 52% of these data improving the 24-h forecast on average (Figure 1c).

Figure 2 shows the time-averaged spatial distribution of observation impacts from ASCAT winds assimilated at 00 UTC. Large forecast error reductions (blue) occur due to assimilation of these data over the North Pacific and South Atlantic Oceans, with smaller, but overall positive, impacts in other mid-latitude locations in both hemispheres. As with all data types, ASCAT observations in some locations degrade the forecast on average (red). However, the results clearly reflect the positive overall impact of ASCAT.

The results shown here indicate that ASCAT surface winds provide a high-quality source of information for global NWP. While not discussed here, it is expected that ASCAT observations can have a substantial impact on forecasts of individual weather events such as tropical cyclones. This is a subject of ongoing study.

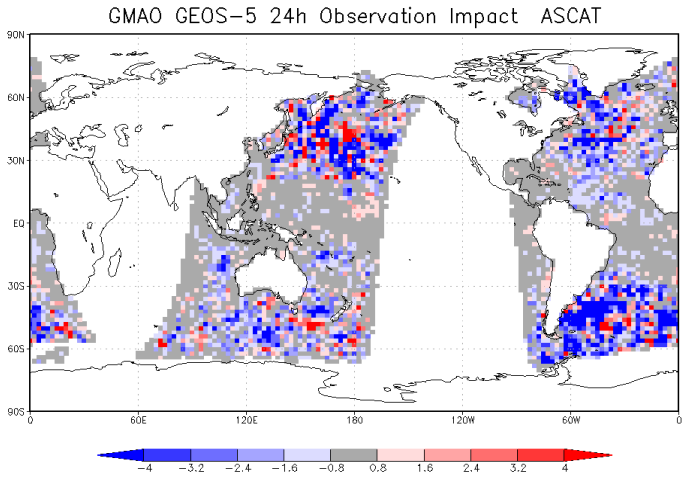

Figure 2: Average impact of ASCAT observations on GEOS-5 24-hr forecasts from 00 UTC during the study period. Results represent 2° × 2° gridded average values. The units are 10^{-5} J kg^{-1}.

References:

Bi, L., J. A. Jung, M. C. Morgan and J. F. Le Marshall, 2011: Assessment of assimilating ASCAT surface wind retrievals in the NCEP global data assimilation system. *Mon. Wea. Rev.*, in press.

Using a Bi-Conjugate Gradient Minimization Algorithm for 3D and 4D Variational Data Assimilation

Amal El Akkraoui, Ricardo Todling and Yannick Trémolet (ECMWF)

A preferred minimization for strong constraint 4DVar currently uses a Lanczos-based Conjugate Gradient (CG) algorithm. This requires the availability of the square-root of the background error covariance matrix. In the context of weak constraint 4DVar, this requirement might be too restrictive for the formulations of the model error term. It might therefore be desirable to avoid a square-root decomposition of the augmented background term (sqrt(B)). In this respect, an appealing minimization scheme is the double CG minimization employed, for example, in the Grid-point Statistical Interpolation analysis (GSI). However, this procedure cannot easily take advantage of the preconditioning using the eigenvectors of the Hessian, readily available in the Lanczos-based CG. Alternatively, this could be exploited by considering a Bi-Conjugate Gradient (Bi-CG) algorithm, which by construction is suitable for non-symmetric matrices.

Throughout this work, the mathematical formulation of the Bi-CG was examined along with the Lanczos-biorthogonalization procedure by which the left- and right-Hessian eigenvectors are calculated for use in the preconditioning. Implementation of the scheme was done in the context of GSI, and in the 3DVar framework. Three minimization strategies were also compared in GSI: the double CG (with an added re-orthogonalization step for improved performance), the sqrt(B) Lanczos-based CG, and the new Bi-CG algorithm.

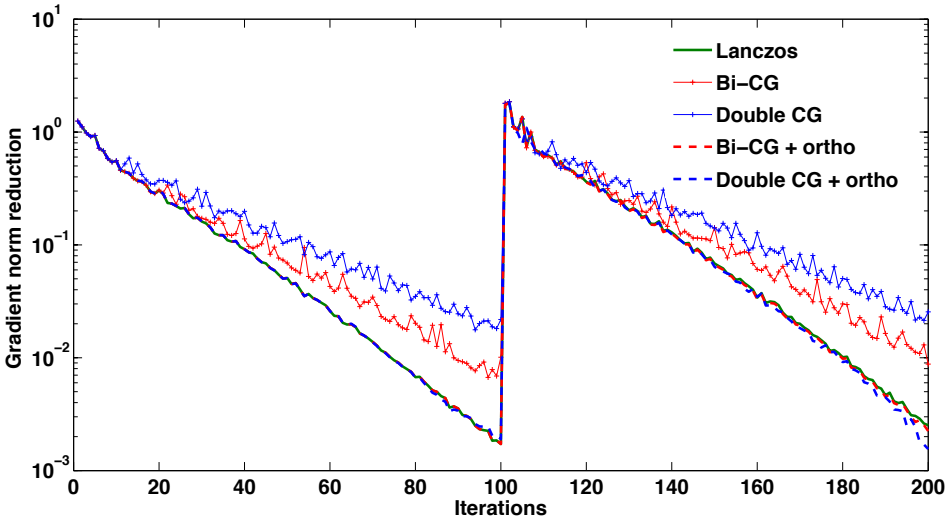

Figure 1: The effect of adding a re-orthogonalization step on the minimization of the BiCG and the Double CG.

Figure 1 shows a 3DVar minimization with two outer loups carried with the Lanczos-based CG (green line), the BiCG (red crossed line), and the Double CG (blue crossed line). Since the loss of orthogonality is a common feature of Conjugate Gradient methods, an additional step of re-orthogonalization of the gradients was added to the BiCG (red dashed line) and the Double CG (blue dashed line). This results in the three algorithms converging with the same rate and to the same solution. Despite the additional computational cost, the importance of re-orthogonalization is shown to be fundamental, especially for the BiCG scheme.

Furthermore, a Lanczos bi-orthogonalization process was implemented in the BiCG algorithm to calculate the Hessian eigendecomposition. When using the eigenvectors for preconditioning, the BiCG behavior is comparable to that of the Lanczos-CG algorithm. Figure 2 shows the minimization of the BiCG and the Lanczos-based CG when the second outer loop is preconditioned with 20 eigenvectors of their respective Hessians. Both schemes construct the same approximation of the Hessian with the same number of eigenvectors, and benefit in the same way of the reduction of the condition number.

Based on these results, the BiCG is currently available as a minimization option in GSI. This work also highlights the importance of correcting for the loss of orthogonality in Conjugate Gradients methods and serves as an opportunity to work on the optimization of the Lanczos-based CG algorithm. Finally, the results of the preconditioning of the minimization with eigenvectors of a nonsymmetric Hessian are encouraging and enable GSI applications to employ general formulations of weak-constraint 4DVar using the BiCG.

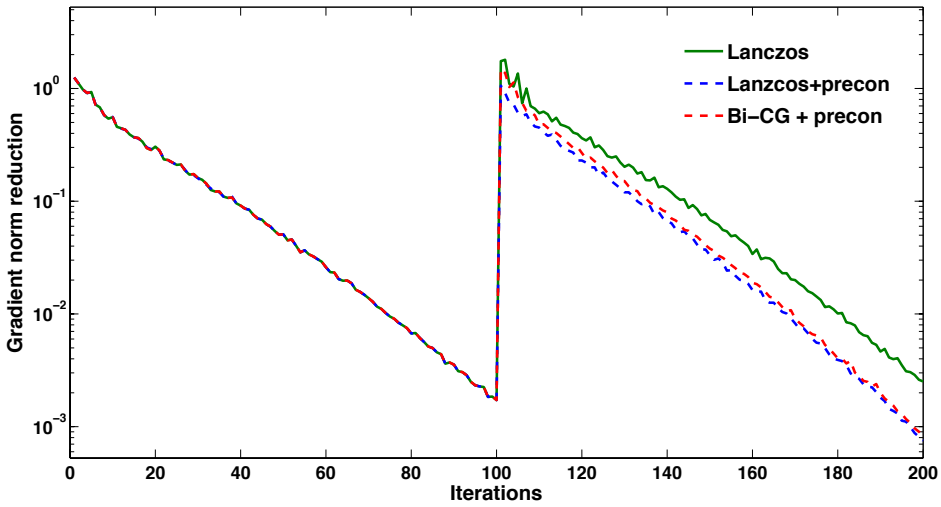

Figure 2: The BiCG and the Lanczos precondtioned with 20 eigenvectors of their respective Hessians.

Publication:

El Akkraoui, A., Y. Trémolet, and R. Todling, 2011: Preconditioning of variational data assimilation and the use of a Bi-Conjugate Gradient Method. *Quart. J. Roy. Meteorol. Soc.* (submitted).

The Simulation and Assimilation of Doppler Wind Lidar Measurements in Support of Future Instruments

Will McCarty, Ronald Errico and Ronald Gelaro

Doppler Wind Lidar (DWL) measurements will be available over the globe with the launch of the Aeolus mission by the European Space Agency in 2013. Another DWL mission, 3D-Winds, was recommended in the NRC's decadal survey as a tier-3 mission. With a new observation platform, existing heritage measurements are typically utilized for pre-launch preparation. However, this approach cannot be used for DWL as these observations have no spaceborne heritage. To compensate, simulated observations can be used to develop the techniques necessary to maximize the utility of the observations post-launch.

There are a number of ways to simulate and utilize observations for this purpose. At the GMAO, the simulation and assimilation of DWL observations utilize the OSSE framework developed in-house. This OSSE consists of a realistically simulated global observing system, including conventional observations and satellite radiances. The framework has then been expanded to include DWL observations for the Aeolus mission simulated using the Lidar Performance Analysis Simulator (LIPAS, Marseille and Stoffelen, 2003) developed at the Royal Netherlands Meteorological Institute (KNMI). Simulated observations are used in the Goddard Earth Observing System (GEOS) data assimilation system, with and without DWL observations, to consider the impacts on the analyses and forecasts.

Figure 1 shows, using two different color scales, the difference in RMS by including and excluding the simulated DWL observations in the OSSE framework. The coarser color scale shows clearly that the largest impacts are seen in the tropics. The mass field is well sampled globally, so the wind fields in the mid-latitudes and polar regions can be inferred through mass-wind balance. Since balance assumptions become invalid in the tropics, this is where the addition of wind measurements has the largest positive impact. The finer color scale is used to show the extra-tropical regions, where the impacts are smaller, yet still remain generally positive. While there are small areas of negative impact, they are not comparable to the broad spatial extent of the areas of positive impact.

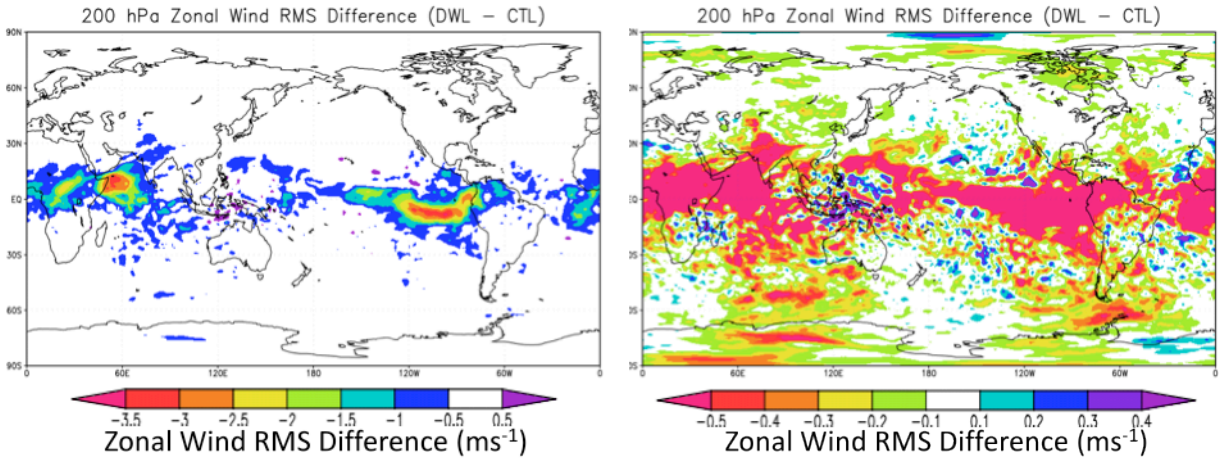

Figure 1: Difference in the 200 hPa zonal wind RMS between the control (no DWL) and experiment (with DWL). Negative (positive) values indicate a reduction (increase) in RMS error by the addition of DWL measurements to the OSSE framework. The same fields with different color scales are shown, and the finer scale (right) saturates at the values that appear in the coarser scaling (left). The results shown are for 0000 UTC and 1200 UTC analyses.

The differences in the Southern Hemisphere are larger, as expected, because there are fewer conventional observations than in the Northern Hemisphere. The satellite orbit tracks south and west of Australia and

South America are quite clear, consistent with the Aeolus orbits for 0000 and 1200 UTC analysis periods. The satellite tracks are less prominent in the Northern Hemisphere because of the large volume of conventional observations at those analysis times. The analyses, both with and without DWL measurements, draw closely to radiosondes at these times as they have lower observational error than the DWL measurements. Though not shown, the moisture and temperature analyses were also seen to improve consistently aloft, with the magnitudes being neutral near the surface. The largest impacts were again seen in the tropics.

The DWL instrument on Aeolus is capable of two different observation types. The first set of observations is capable of measuring in clear-sky as the backscatter measured is based on Rayleigh scattering. The second measures a sharper signal based on Mie backscatter from larger particles such as clouds and aerosols. The overall number of observations for each type decreases towards the surface as clouds attenuate the signal from the lidar. In the upper- troposphere, the Rayleigh measurements are seen to be more numerous and of higher quality. In the mid-troposphere, they have similar quality, but there are far more Rayleigh observations than Mie observations. Near the surface, there are more Mie observations, and they are more accurate than the Rayleigh observations.

Figure 2 shows the latitudinally-averaged difference in zonal wind RMS. The DWL experiment, which uses both the Rayleigh and Mie observations, corresponds to the latitudinal averages of the field shown in Figure 1. Also shown are experiments utilizing the OSSE framework with only the Rayleigh or Mie observations. In this field, it is seen that the Rayleigh-only experiment and the DWL experiment follow each other very closely, showing that the bulk of the positive impact is coming from these observations. The Mie-only experiment is far more neutral outside of and has less positive impact within the tropics.

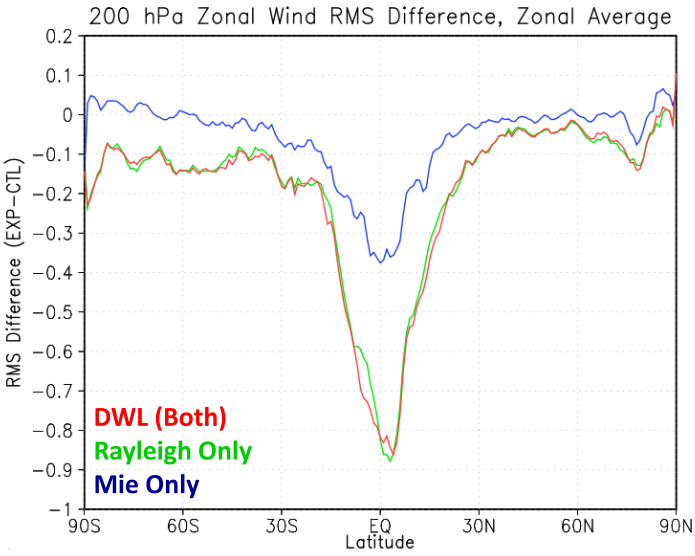

Figure 2: The latitudinally-averaged difference in the 200 hPa zonal wind RMS between the control (no DWL) and experiment (with DWL). Shown is the DWL experiment (red), as well as experiments utilizing only the Rayleigh (green) and Mie (blue) observations.

It was recently determined that there would be significant changes in instrument design to the Aeolus mission. As a result, these experiments will need to be redone upon the delivery of an updated instrument simulator from KNMI. It should also be noted that these results are already known to be overstated as a result of a lack of clouds within the *nature run* in which the OSSE framework is based (McCarty et a., 2011).

Reference:

Marseille, G. J., and A. Stoffelen, 2003: Simulation of wind profiles from a space-borne Doppler wind lidar. *Quart. J. Roy. Meteor. Soc*., **129**, 3079-3098.

Publication:

McCarty, W., R. Errico, and R. Gelaro, 2011: Cloud Coverage in the Joint OSSE Nature Run. *Mon. Wea. Rev*. (submitted).

MODIS Cloud Data Assimilation at GMAO

Arlindo da Silva and Peter Norris

The current horizontal resolution of GEOS-5 NWP and climate simulations, although much increased, is still not sufficient to resolve individual clouds, which regularly have scales of 1 km or less. This is the basis for GCM cloud parameterization routines in general, and of our development of an advanced statistical cloud parameterization for GEOS-5 in particular. The parameterization characterizes the statistical properties of cloud within a model gridcolumn using distributions of sub-gridscale total moisture in each model layer and using a copula function to correlate these distributions in the vertical (see Norris et al., 2008). As in the earlier work of Norris and da Silva (2007), we are developing practical methods to constrain our statistical parameterization with satellite-retrieved cloud data, in particular, by trying to extract statistical information from high-resolution satellite data that constrains the layer moisture distributions and the copula cloud overlap model. The MODIS instruments on the Terra and Aqua satellites provide a wealth of high-resolution cloud retrievals (cloud optical thickness in 1 km pixels and cloud top pressure in 5 km pixels) that suit this purpose very well. This type of parameter constraint or parameter estimation is a form of cloud data assimilation, having the ability to correct biases both in the moisture state variables and in the empirical constants of the cloud parameterization.

Existing cloud assimilation schemes are often based on tangent linear models, which, in the case of the cloud routines, is problematic because cloud free regions have essentially zero sensitivity to infinitesimal temperature of moisture perturbations and therefore cannot be made cloudy by the observation of clouds. To address these sorts of issues we take a novel approach using Markov Chain Monte Carlo methods to allow finite (but reasonable) departures from the background state into regions of control parameter space with higher posteriori probability, such as into regions that simulate cloud in the presence of cloudy observations.

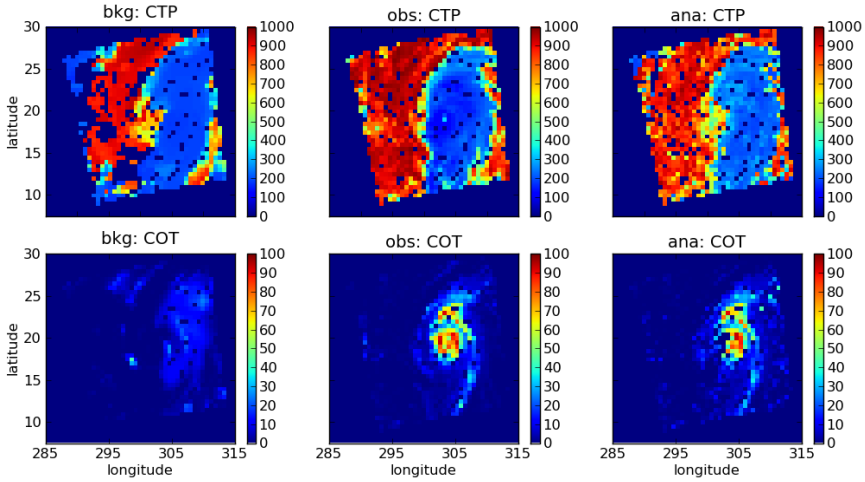

Cloud Top Pressure [hPa] and Cloud Optical Thickness for a MODIS granule over Hurricane Bill (Aug 19, 2009, 1720z), projected onto the GEOS-5 1/2 x 2/3° grid. The middle panels show actual MODIS retrievals, the left and right panels, simulated retrievals — (Left) a poor background state, (Right) the analysis after assimilation of the observations. Clearly the analysis is much improved.

References:

Norris, P. M. and A. M. da Silva, 2007: Assimilation of satellite cloud data into the GMAO Finite-Volume Data Assimilation System using a parameter estimation method. Part I: Motivation and algorithm description, *J. Atmos. Sci.*, **64**, 3880-3895.

Norris, P. M., L. Oreopoulos, A. Y. Hou, W-K Tao, X. Zeng, 2008: Representation of 3D heterogeneous cloud fields using copulas: Theory for water clouds. *Q. J. R. Meteorol. Soc.,* **134,** 1843-1864. doi:10.1002/qj.321.

Development and Validation of an Observing System Simulation Experiment System at the GMAO

Ronald Errico and Nikki Prive

The ability to conduct meaningful Observing System Simulation Experiments will allow NASA to evaluate the utility of competing instruments and designs for sources of new earth-system observations. They will also provide a new diagnostic tool to investigate properties and behaviors of the GMAO's data assimilation systems. As for any simulation, an OSSE's utility is determined by its validity. This, in turn, depends on the realism of the simulated observations it ingests, principally on their implicit and explicit errors.

Some of the primary metrics for OSSE validation are observation increments (omf) statistics. Although these are potentially complex functions of simulated observation errors, a technique was developed to expedite tuning of the simulated observation errors added as part of the OSSE. Essentially, based on earlier experiments, the approximation is made that the background error components to omf variances are relatively unaffected by reasonable changes to the observation error model. Thus, the latter can be quickly tuned by simply evaluating differences between corresponding previous OSSE and real-data assimilation omf statistics.

The means of omf are qualitatively similar for the corresponding OSSE and real-data results suggesting that model biases in the OSSE context are appropriate. Variances of omf for individual instrument channels or observation pressure levels are generally within 10% of the real data values, which is within the sampling accuracy. For most observation types, horizontal correlations of omf are also realistic. Although it is also possible to tune the latter to better match results with real data, this may be undesirable until it can be clearly demonstrated that this tuning is not masking mismatches of background errors as observation errors instead.

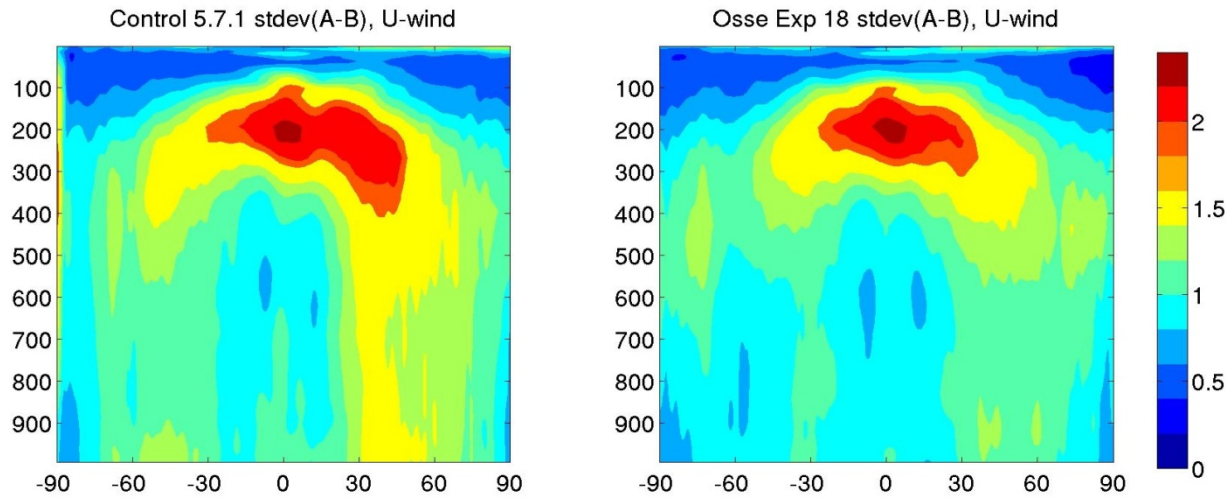

Figure 1: Square roots of zonal means of temporal variances of analysis increments of the eastward wind component for January, as functions of height and latitude. Those produced by the assimilation of real observations are shown left and simulated ones are shown right for one of the tuning experiments.

A number of other improvements to the OSSE system have been implemented. Locations of simulated winds derived from tracking satellite imagery are now consistent with locations of clouds in the nature run (previously, locations of such observations for real observations on the corresponding day were used). The topography used by the DAS has been changed to be closer to that used in the nature run. More

realistic surface property specification is used for determining surface emissivity over land. This includes vegetation index and fraction, snow cover and temperature, and soil moisture content. A good simulation of the errors associated with the surface emissivity model used to create the simulated radiance observations, however, still remains to be developed.

In earlier tuning experiments it was noticed that some explicitly correlated random observation error appeared to be required for reasonably matching several metrics in OSSE and real-data results. For satellite radiances and cloud track winds, the explicitly added observational errors are therefore horizontally correlated. This is accomplished by projecting spherical harmonic functions onto a global grid using spectral coefficients that are randomly valued such that the expected power spectra correspond to those for Gaussian-shaped correlation functions on the sphere. For AIRS, the added errors are also correlated between channels, and explicit errors for some conventional observations (e.g., sounds and cloud-track wind) have vertical correlations.

Parameters for the horizontal error correlation model are tuned using a partly automated process that appears efficient. Not only are horizontal correlations of omf better matched in OSSE and real-data results, but variances of analysis increments are also. The latter is an important metric since it measures the total "work" performed by the analysis system in altering the background fields provided it.

An example result from one of the tuning experiments appears in Figure 1. It shows measures of the analysis increment in OSSE and real-data results for the zonal wind component. Although the two results have similar structure, the OSSE values are 10-15% weaker in many locations. Without adding the horizontally correlated errors, however, this weakness is doubled. It is an even greater improvement compared to published results for previous OSSE frameworks.

Another important validation metric is an estimate of the Kalman gain implied by the OSSE results. Here, it is approximated by the difference of background and analysis error variances normalized by the former variances. The errors are determined explicitly, by comparison with the nature run fields as truth. This requires carefully projecting the latter onto the analysis grid so that only the scales actually analyzed are evaluated and so that interpolation errors do not contaminate the metric. Since this metric cannot be as accurately estimated in the real-data context, its evaluation here simply regards its reasonableness: Do the OSSE values indicate that the DAS is improving the background estimates of the state in all the regions expected.

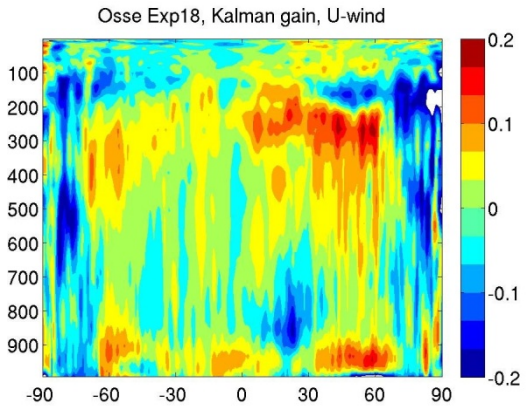

Figure 2: Zonal averages of estimated Kalman gain (difference between background and analysis error variances normalized by the former) for the zonal wind component, averaged zonally as a function of latitude and pressure for the month of July.

An example of this metric produced for one of the tuning experiments appears in Figure 2 for the zonal wind. In past experiments, for most of the globe below 700 hPa, this metric has been strongly negative, indicating in particular that the low-level cloud track winds were degrading forecasts in the OSSE compared with the improvements measured in real-data experiments. Here, most of that unrealism has been removed. Tuning experiments that are currently running are expected to perform even better.

It is expected that a useful baseline validated OSSE will be available during the summer of 2011. In anticipation, this OSSE capability is already being extended to additional observing instruments and types (such as IASI). The appropriate incorporation of these should be greatly facilitated by the new software for automating the otherwise tedious process of modeling the associated explicit observation errors to be added.

Observational Constraints on the width of the PDF for GEOS-5 Total Water using AIRS Data

Andrea Molod

An important element of the suite of physical parameterizations in the GEOS-5 Atmospheric General Circulation Model (AGCM) is the scheme used to model cloud processes. As part of any GCM's parameterization of cloud processes such as condensation and re-evaporation, an assumption must be made about the sub-grid scale distribution of total water or a related quantity. The GEOS-5 scheme assumes that total water is governed by a "top-hat" probability distribution function (PDF), requiring as input the two parameters that govern the distribution: the value of the mean and the width of the "top-hat". The values of these parameters, in particular the width parameter, and the variations with altitude and geographical location, are not presently constrained by observations. The work described here uses data from the Atmospheric Infrared Sounder (AIRS) aboard the Aqua spacecraft to guide the choice of the width of the PDF and its variation with height.

For the "top-hat" distribution of total water used in GEOS-5, there is a straightforward connection between the width of the PDF and the critical relative humidity, RH_{crit}, used for condensation and evaporation. The top-hat PDF is shown schematically in Figure 1. If condensation is assumed to occur in the areas of the grid box that are supersaturated, the critical condition for condensation can be expressed as:

$$q^* \le \overline{q_T} + \sigma \rightarrow \frac{q_T}{q^*} = 1 - \sigma \rightarrow RH_{crit} \equiv 1 - \sigma,$$

where q_T is the total water in a grid box, q^* is the saturation specific humidity, and σ is the half-width of the top-hat PDF.

Figure 1: Schematic of three different "top-hat" PDFs. Distribution half-width of the widest distribution is denoted by σ, and the stippled region is the total condensate. For the two narrower PDFs in red and in blue, there is no condensate.

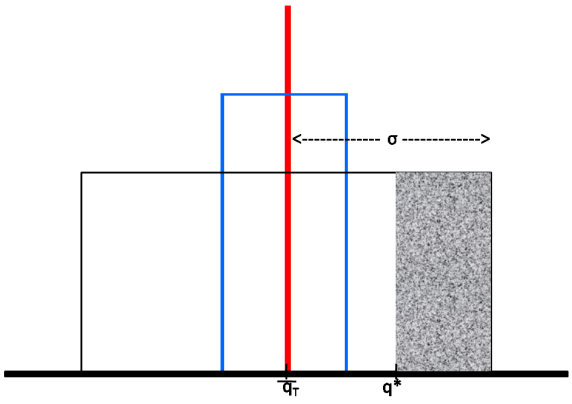

AIRS Data and the RH01 Diagnostic: AIRS data were obtained from the Goddard DAAC: http://acdisc.sci.gsfc.nasa.gov/daac-bin. The Level 3 monthly mean product was chosen, providing, among other fields, monthly mean cloud fraction and relative humidity using AIRS, AMSU (Advanced Microwave Sounding Unit) and HSB (Humidity Sensor for Brazil) radiances for the retrieval (Aumann et al., 2003). Data are available on a $1^\circ \times 1^\circ$ grid at 12 pressure levels. The AIRS monthly mean relative humidity and cloud fraction fields were used to compute an RH01 diagnostic, defined here as the relative humidity of grid boxes sampled when the cloud fraction exceeds zero but is less than 10%. This is assumed here to represent the relative humidity in grid boxes where the cloud drops are recently formed or are about to re-evaporate. That is, grid boxes for which the relative humidity is close to its critical value (RH_{crit}) as described in the GCM conceptualization of grid scale condensation defined earlier. Although the upper limit of 10% of cloud cover is arbitrary, the resulting profiles are not sensitive to the difference among choices of thresholds between 1 and 10%, and the 10% threshold provides the largest sample of grid boxes. The RH01 diagnostic computed from AIRS data is meant as a general guideline for the GCM value of RH_{crit}. Profiles of RH01 are shown in Figure 2. The month to month differences in the global profiles are small, as seen in panel a), and there are distinct differences between the land (red) and ocean (blue) profiles in all geographic regions, particularly near the surface.

The increase of RH_{crit} near the surface relative to the values aloft is equivalent to narrower PDFs near the surface. This can be interpreted as the result of an efficient turbulent mixing process that homogenizes the total water distribution. The smaller values near the surface over land are interpreted as a result of the increased land surface heterogeneity. The general vertical profile shape is similar to a tanh function, and a tanh-shaped RH_{crit} profile has been used in simulations with GEOS-5. The land/ocean contrast, whereby the RH_{crit} values over land surfaces are smaller than those over oceans, was also part of the specified profiles. In an ongoing study, the AIRS RH01 profiles will be used as part of the development of a set of state-dependant RH_{crit} profiles for the AGCM.

Figure 2: a) Globally averaged profiles of AIRS-derived RH01 for each month of the year over ocean (group with larger values near the surface) and land surfaces. The horizontal axis is relative humidity in percent; the vertical axis is pressure in hPa. b) As for a), but July profiles only are shown. The black curve is the global mean RH01, blue is the mean over oceans, red is the mean over land. c) As for b), but for tropical latitudes only, and d) for extratropical regions.

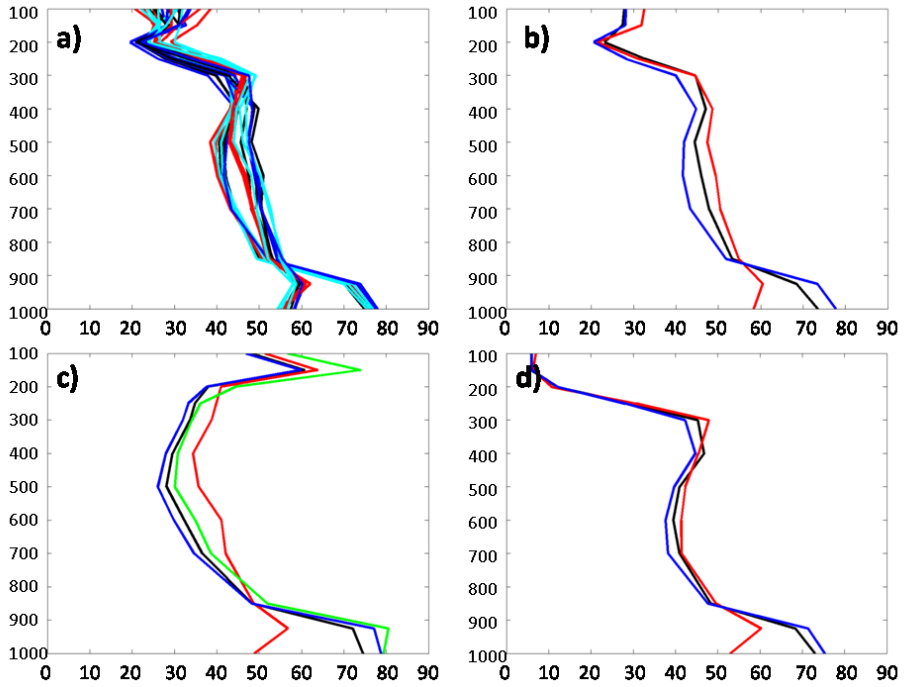

Reference:

Aumann, H. H., M. T. Chahine, C. Gautier, M. Goldberg, E. Kalnay, L. McMillin, H. Revercomb, P.W. Rosenkranz, W.L. Smith, D. Staelin, L. Strow, and J. Susskind, 2003: AIRS/AMSU/HSB on the Aqua mission: Design, science objectives, data products, and processing systems, IEEE15 *Trans. Geosci. Remote Sens*., **41**, 253-264.

GEOS-5 Coupled Climate Modeling

Yury Vikhliaev, Max Suarez, Andrea Molod, Bin Zhao and Jelena Marshak

The GEOS-5 Atmosphere-Ocean General Circulation Model (AOGCM) is designed to simulate climate variability on a wide range of time scales, from synoptic time scales to multi-decadal climate change. It has been tested in coupled simulations and data assimilation mode. Its main components are the atmospheric model coupled to the catchment land surface model, both developed by the GMAO (the GEOS-5 AGCM), and MOM4, the ocean model developed by NOAA's Geophysical Fluid Dynamics Laboratory. Every time step, these two components exchange fluxes of momentum, heat and fresh water through a "skin layer" interface. The skin layer module includes parameterization of the diurnal cycle and a sea ice model (CICE from DOE's Los Alamos National Laboratory). All components are coupled together using the Earth System Modeling Framework (ESMF).

The performance of the GEOS-5 AOGCM was evaluated through a multi-decadal coupled climate simulation with the atmospheric component at a resolution of 2.5° longitude × 2° latitude × 72 layers, and the ocean component in a 1° × 50 layer configuration with a refinement to 1/3° in the equatorial region. The simulation demonstrated a stable, realistic mean climate and inter-annual climate variability. The mean atmospheric state simulated by the AOGCM is similar to the atmospheric state simulated by the GEOS5 AGCM forced by the observed sea surface temperature (SST). Errors in the coupled simulation primarily have the same structure as errors in the uncoupled simulation, but usually with larger magnitude. These errors include: too strong surface wind stress in high latitudes; too strong cloud radiative forcing in low latitudes, and too weak cloud radiative forcing in high latitudes; errors in precipitation typical of most state-of-the-art climate models, e.g., a strong double Inter-Tropical Convergence Zone (ITCZ).

On the ocean side, the upper ocean circulation and surface climate reach equilibrium in several decades, while the deep ocean circulation still exhibits a drift after 150 years of integration. SST is an important measure of the realism of the model climate, since it is used by the atmospheric component as a boundary condition.

As Figure 1 shows, the sea surface temperature from the 150-year simulation is quite realistic. The dominant errors are typical for state-of-the-art climate models. For example, the warm SST bias near the eastern boundaries of the oceans is due to deficiencies in simulating the orientation of the wind stress as well as lack of resolution of the coastal upwelling. Errors in the regions of western boundary currents result from deficiencies in simulating the strength of the western boundary currents and the separation location. These types of errors are typically reduced with the increased resolution.

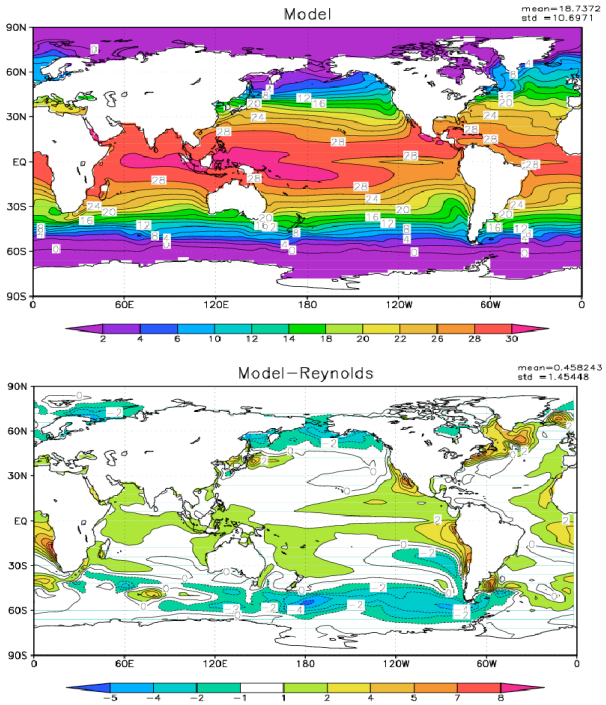

Figure 1: Sea surface temperature (top) from the GEOS-5 AOGCM simulation, and the bias relative to the Reynolds climatology (bottom).

The leading mode of global SST variability is shown in Figure 2. This mode exhibits the prominent El Niño - Southern Oscillation (ENSO) pattern, which varies on inter-annual time scales. Compared to observations, the model El Niño pattern is narrower and extends further into the western Pacific. In addition to the dominant signal in the equatorial Pacific, the model also captures the

co-variability in the sub-tropical Pacific. Comparison between the model and observed time series of the leading SST mode shows that model ENSO has a reasonable time scale and irregularity with, however, a tendency to have slightly higher frequency than observed.

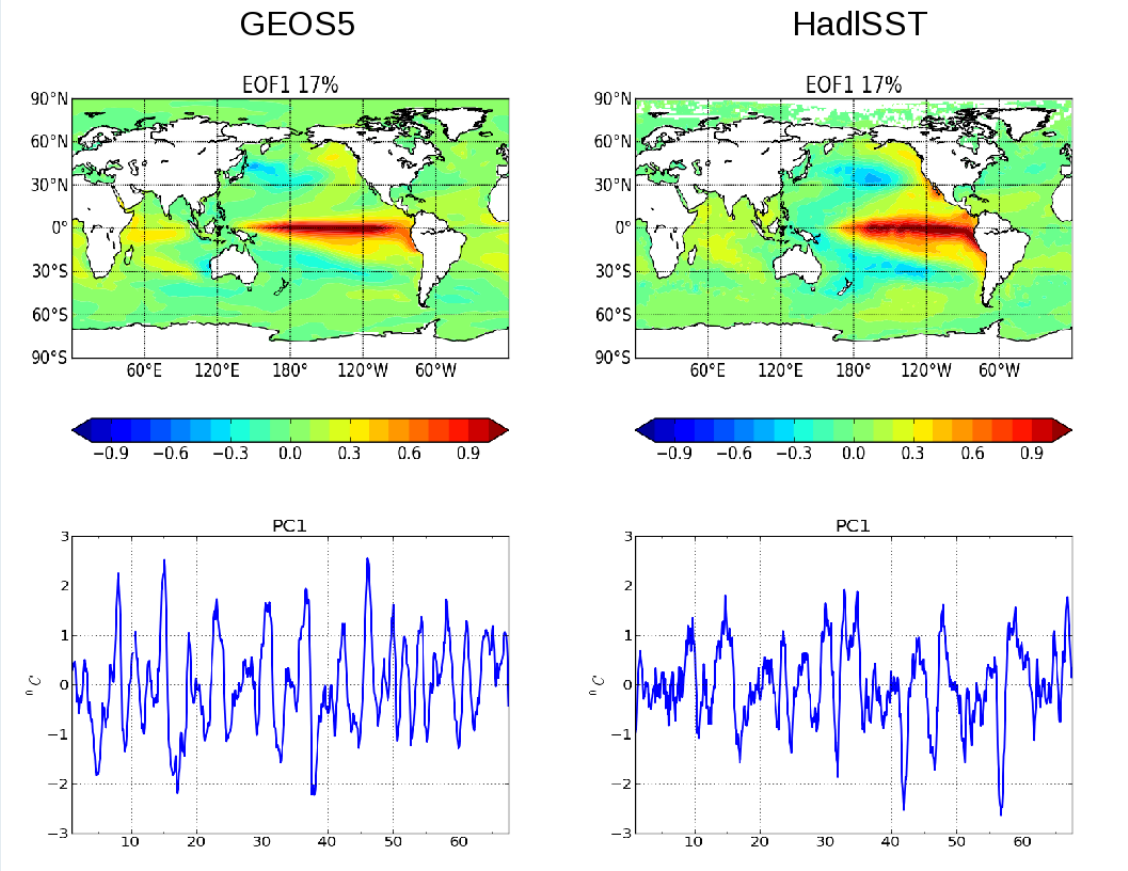

Figure 2: The leading mode of global SST variability from the GEOS-5 AOGCM (left) and the Hadley Center (right). Top panels show the leading empirical orthogonal functions of the global SST. Bottom panels show corresponding principal components.

Overall, the performance of the model is comparable to the performance of state-of-the art coupled climate models being used for the next IPCC assessment report. The errors are typical of most climate models. These errors will be addressed during further development of the GEOS-5 AOGCM, including increased resolution. The model now routinely runs on the supercomputing clusters at the NASA Center for Climate Simulation (NCCS) and the NASA Advanced Supercomputing Division (NAS). Projects underway with the GEOS-5 AOGCM include weakly coupled ocean-atmosphere data assimilation, seasonal climate predictions, and decadal climate prediction tests within the framework of Coupled Model Intercomparison Project (CMIP5). The decadal climate prediction experiments are being initialized using the weakly coupled atmosphere-ocean data assimilation based on MERRA. The results of these experiments will be distributed through the NCCS Earth System Grid node.

Flow-Adaptive Ocean Data Assimilation into a High-Resolution Global Coupled Model

Christian Keppenne and Guillaume Vernieres

Data assimilation refers to the process of using a numerical model to interpolate in space and time between sparse and inexact observations. Under certain reasonable assumptions, the Kalman Filter can calculate the optimal weights with which to weigh the estimates of the state of a dynamical system (in our case, the climate system), provided on the one hand by the model and on other by the observations, to arrive at the optical state estimate.

One version of the GMAO ocean data assimilation system uses an ensemble Kalman Filter (EnKF) in which the time propagation of the background error covariance called for by the Kalman Filter is approximated using a relatively small number of model integrations. Our current system estimates background error covariances from the distribution of a relatively low resolution ensemble of MOM4 ocean models (at 1° horizontal resolution) coupled to an ensemble of GEOS-5 AGCMs (at 2° resolution) and uses this information to update the state of a higher-resolution coupled atmosphere-ocean model (AOGCM with 1/2° ocean and 1° atmosphere). While the use of an ensemble of lower resolution models to estimate the background covariances achieves very significant savings, the system still requires 1840 computer processors.

The dual resolution approach enables us to utilize the EnKF for a global assimilation of synoptic scale ocean data into the GEOS-5 AOGCM. However, the 1/2° ocean model is much too coarse to resolve the Western Boundary Currents or the ocean mesoscale. For this we will use a version of the AOGCM comprised of a 1/16° ocean with a 1/4° atmosphere. A minimum of 1920 processors will be required to run the high resolution AOGCM and the dual resolution EnKF will be too computationally expensive to use with it. Besides, assuming this approach could be used effectively, it would only provide large-scale background error covariance information and thus would not help constrain the mesoscale, assuming there are observations to do so.

We have developed a new spatially adaptive flow estimation (SAFE) methodology to function as a cost-effective flow-adaptive alternative to the EnKF. SAFE determines error covariance information from the local joint spatial distribution of model state variables and does not require that multiple model copies be run concurrently. The local covariance information is optionally complemented with temporal background error covariance estimates obtained by sampling the model state vector at regular intervals along a single model trajectory.

The SAFE methodology includes iterative data adaptive algorithms to optimally estimate the error of each assimilated observation and the geometry of the region which each observation is allowed to influence. The error estimates are a function of how well each observation can be explained by other nearby observations. The adaptively derived geometrical information reflects how well each observation explains neighboring data.

We have conducted the initial tests of the SAFE methodology with an AOGCM configuration of a 1/8° ocean and a 1° atmosphere. Following a cold start of the coupled model, we have assimilated surface temperature, salt and sea-ice extent into the coupled model daily. The upper panel in Figure 1 shows the details of the model surface temperature field in the Kuroshio region after 7 months. The middle panel shows the corresponding observations from Reynolds. The corresponding SST analysis from the 1/2° production ocean analysis is shown in the lower panel. (The production analysis starts in 1960 and assimilates *in situ* data in addition to the surface data processed here with the higher-resolution AOGCM.) Figure 2 shows the details over the eastern equatorial Pacific. Interestingly, tropical instability waves are adequately represented in the 1/8° SAFE analysis while they are smoothed out in the 1/2° analysis.

The rapid convergence of the 1/8° ocean analysis to the Reynolds analysis indicates that the SAFE methodology is working as expected and is ready to be applied with the 1/16° eddy-resolving ocean model.

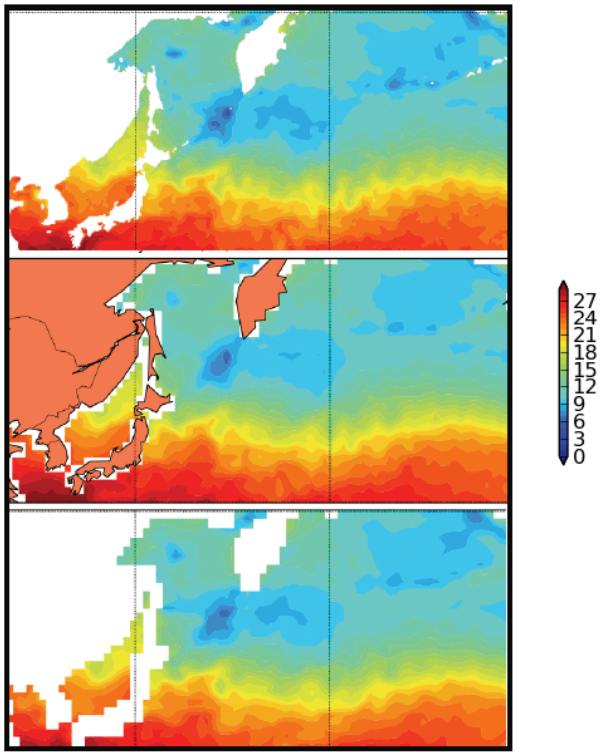

Figure 1: (Top panel) Detail of the 1/8° ocean analysis of SST on 1 August 2007 after 7 months of daily data assimilation. (Middle panel) The corresponding observed SST from Reynolds. (Bottom panel) The corresponding SST from our 1/2° ocean reanalysis.

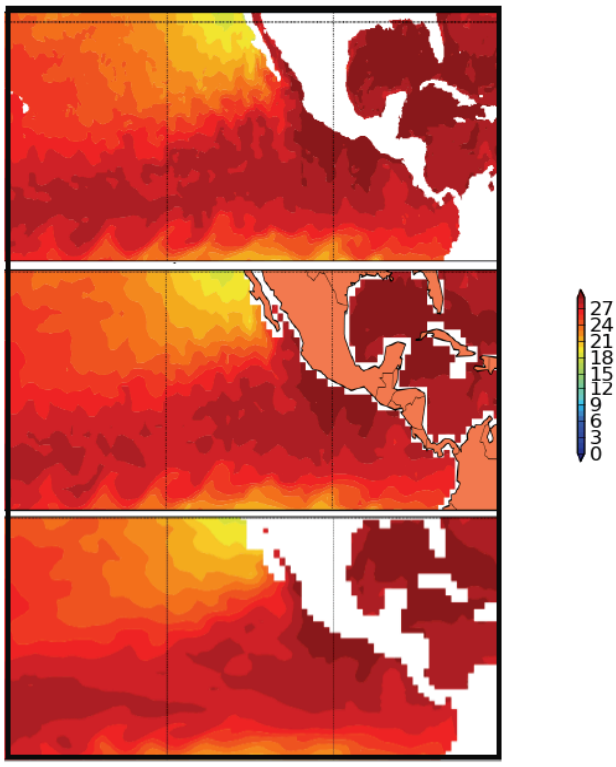

Figure 2: As for Figure 1, but for the eastern equatorial Pacific.

The Contributions of Precipitation and Soil Moisture Observations to the Skill of Soil Moisture Estimates in a Land Data Assimilation System

Qing Liu, Rolf Reichle, Rajat Bindlish (USDA), Michael Cosh (USDA), Wade Crow (USDA), Richard de Jeu (VU University Amsterdam), Gabriëlle De Lannoy, George Huffman (Code 613.1) and Thomas Jackson (USDA)

Knowledge of the amount of moisture stored in the soil is important for many applications related to the water, energy and carbon transfers between land and atmosphere, including the assessment and prediction of floods and droughts. However, global observations of soil moisture have not been available at the spatial and temporal resolution and with the accuracy necessary to meet applications requirements. Enhanced estimates of soil moisture conditions can be obtained by merging satellite observations of soil moisture with soil moisture estimates from a numerical model of land surface processes that is forced with observation-based precipitation data. The resulting enhanced soil moisture estimates are thus based on two sources of information: (i) direct observations of soil moisture from satellite and (ii) observations of the precipitation forcing that drives soil moisture dynamics.

Relative to baseline soil moisture estimates from MERRA, this study investigates soil moisture skill derived from (i) land model forcing corrections based on large-scale, gauge- and satellite-based precipitation observations and (ii) assimilation of surface soil moisture retrievals from the Advanced Microwave Scanning Radiometer for the Earth Observing System (AMSR-E).

Three precipitation products were used to correct the MERRA precipitation towards gauge- and satellite-based observations. Specifically, we used the NOAA Climate Prediction Center Merged Analysis of Precipitation (CMAP) pentad product ("standard" version), the Global Precipitation Climatology Project (GPCP) Version 2.1 pentad product, and the NOAA Climate Prediction Center (CPC) daily unified precipitation analysis over the United States.

Two different surface soil moisture retrieval products were assimilated into the Catchment model: (i) the operational NASA Level-2B AMSR-E "AE-Land" product (version V09) archived at the National Snow and ice Data Center (NSIDC) and (ii) the AMSR-E Land Parameter Retrieval Model (hereinafter LPRM) product (EASE grid version 03) developed at the VU Amsterdam.

Soil moisture skill is assessed using in situ observations in the continental United States at 37 single-profile sites within the Soil Climate Analysis Network (SCAN) for which skillful AMSR-E retrievals are available. Skill is assessed in terms of the anomaly time series correlation coefficient R.

Figure 1 shows that the average skill of the AMSR-E and MERRA surface soil moisture estimates is comparable. Adding information from precipitation observations increases soil moisture skills for surface *and* root zone soil moisture. Assimilating satellite estimates of *surface* soil moisture also increases soil moisture skills, again for surface *and* root zone soil moisture. Adding information from both sources (precipitation and soil moisture observations) increases soil moisture skills by almost the sum of the individual skill contributions, which demonstrates that precipitation corrections and assimilation of satellite soil moisture retrievals contribute important and largely independent amounts of information.

We repeated our skill analysis against measurements from four USDA Agricultural Research Service ("CalVal") watersheds with high-quality distributed sensor networks that measure soil moisture at the scale of land model and satellite estimates. As expected, the skill of the satellite, model, and assimilation estimates is higher when assessed against the multi-sensor CalVal observations than when skill is assessed against single-profile SCAN measurements (not shown). The relative skill contributions by precipitation corrections and soil moisture retrieval assimilation, however, remain unchanged (not shown). This corroborates the results, shown in Figure 1, which were obtained with a larger network of single-profile sensors.

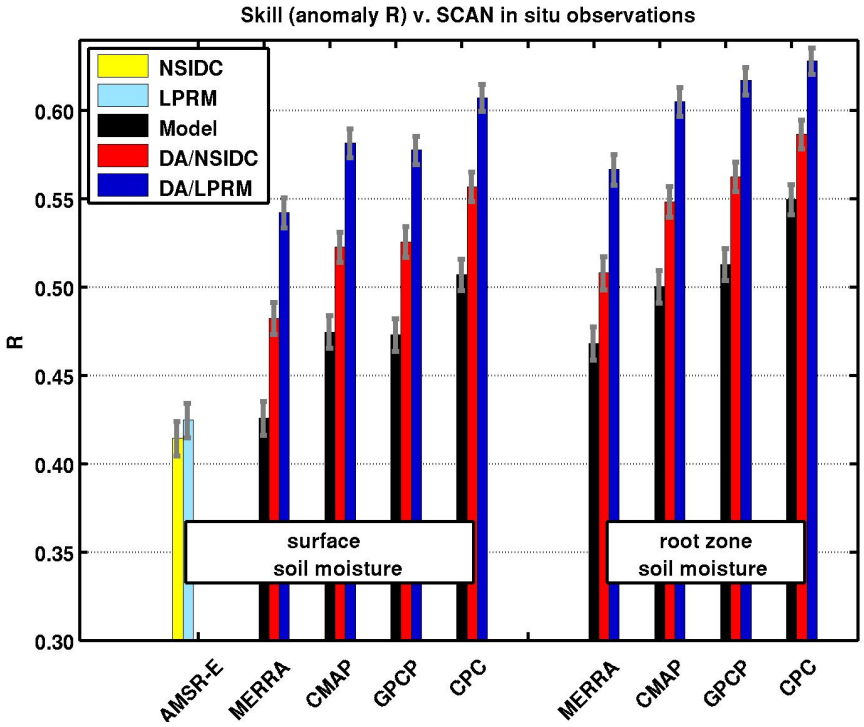

Figure 1: Average time series correlation coefficient R with SCAN in situ surface and root zone soil moisture anomalies for estimates from two AMSR-E retrieval datasets (NSIDC and LPRM), the Catchment model forced with four different precipitation datasets (MERRA, CMAP, GPCP, and CPC), and the corresponding data assimilation integrations (red bars: DA/NSIDC and blue bars: DA/LPRM). Average is based on 37 SCAN sites for surface and 35 SCAN sites for root zone soil moisture. Error bars indicate approximate 95% confidence intervals.

Publication:

Liu, Q., R. H. Reichle, R. Bindlish, M. H. Cosh, W. T. Crow, R. de Jeu, G. J. M. De Lannoy, G. J. Huffman, and T. J. Jackson, 2011: The contributions of precipitation and soil moisture observations to the skill of soil moisture estimates in a land data assimilation system, *J. Hydromet.*, (in press), doi:10.1175/JHM-D-10-05000.

Satellite-scale Snow Water Equivalent Assimilation into a High-resolution Land Surface Model

Gabriëlle De Lannoy, Rolf Reichle, Paul Houser (GMU), Kristi Arsenault (GMU), Niko Verhoest (UGent) and Valentijn Pauwels (UGent)

Snow is an important component of the land system because its occurrence is spatially and temporally discontinuous, and because of its strong impact on the land surface water and energy balance, weather and climate. Land surface models often poorly represent complex snow processes. Enhanced estimates could be expected from assimilation of satellite observations of the snowpack. Satellite observations of the amount of water stored in the snowpack (or snow water equivalent; SWE) can be obtained from passive microwave sensors, but they are only available at relatively coarse resolutions. In a synthetic study, several assimilation and downscaling techniques are explored to update fine-scale snow estimates using coarse-scale SWE retrievals in an ensemble Kalman filter framework.

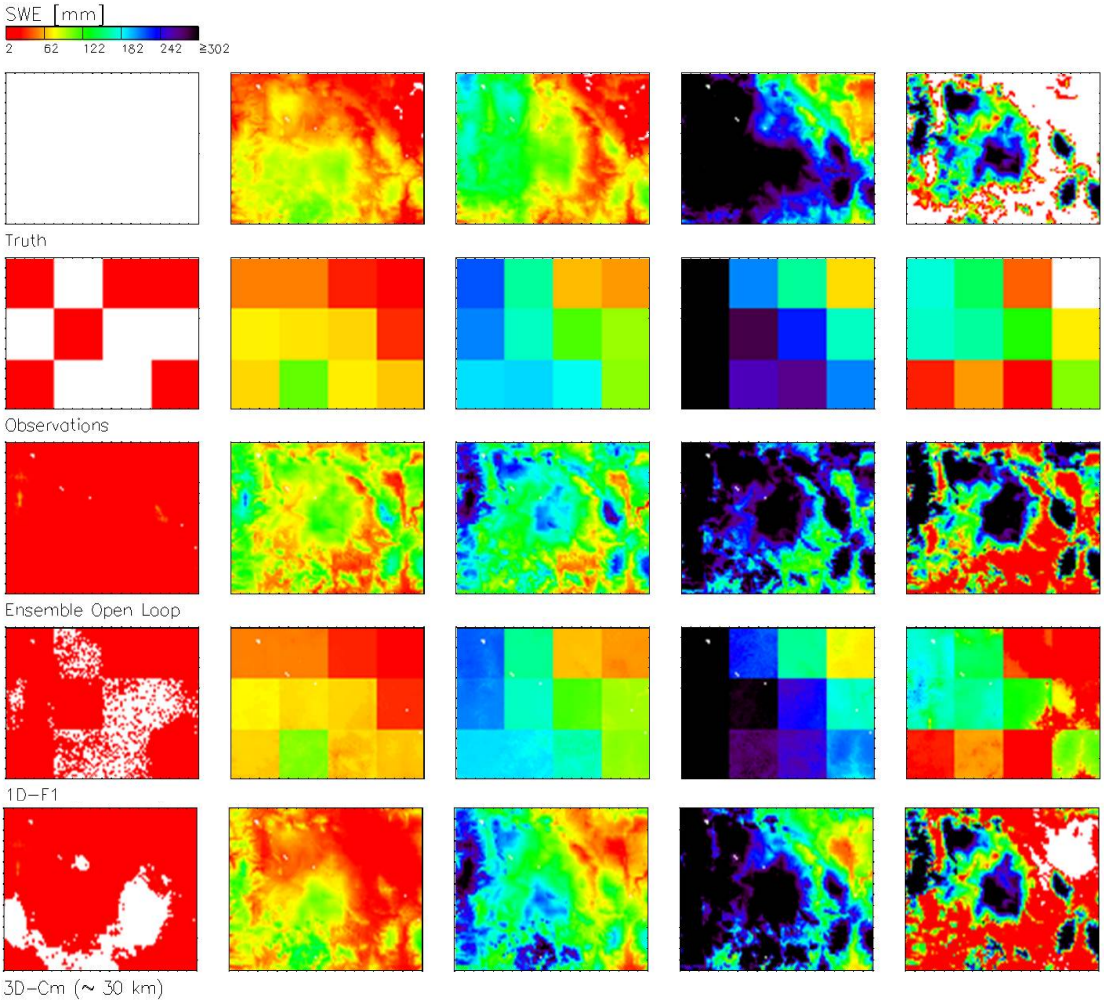

Figure 1: (left to right) Snapshots of SWE fields for 15 Oct 2002, 30 Nov 2002, 15 Jan 2003, 28 Feb 2003, and 15 Apr 2003. (top to bottom) Truth, synthetic observations, ensemble mean open loop forecasts, and analyses obtained with several filter approaches. The spatial correlation length in the forecast perturbations is indicated in parentheses

This study explores a one-dimensional (1D) (or point-wise independent) filter and a variety of three-dimensional (3D) (or spatially distributed) filters to assimilate coarse-scale (~25 km) SWE observations over a small study domain in Northern Colorado, US. The truth is generated at the fine scale (~1 km) by forcing the Noah model with North American Land Data Assimilation System (NLDAS) data. Synthetic observations are generated through aggregation of these fine-scale simulations and addition of observation error. A degraded open loop model integration is simulated by forcing the Noah model with coarse Global Data Assimilation System (GDAS) data and imposing different types of spatially correlated random perturbations.

Figure 1 shows (top row) the "true" reference simulation, (2^{nd} row) the degraded model simulation and (3^{rd} row) the synthetic coarse-scale observations, as well as the analyses for three different assimilation and downscaling techniques.

In the "1D-F1" approach, the coarse-scale observations are trivially disaggregated to the fine scale before data assimilation and are then assimilated at the fine scale with a 1-dimensional ensemble Kalman filter. As can be seen in Figure 1 (4^{th} row), the 1D-F1 filter pushes the analyses to the coarse observation value, which improves the spatial mean SWE estimation but removes most of the sub-pixel spatial variability. Furthermore, significant fine-scale observation bias is introduced.

The best approach is to assimilate the coarse-scale observations directly with a 3D filter and a properly defined observation operator and forecast error correlation structure. For all 3D filters using the coarse observations it is found that the analyses are best when the spatial forecast error correlation length is equal to or larger than 20–30 km, which corresponds to the dimension of the coarse observation pixels and also to the approximate correlation length of the precipitation error field. The results degrade significantly for shorter correlation lengths. When each fine-scale grid point is updated using 3D assimilation of a single overlying coarse observation, the spatial mean SWE field can be improved over that of the observations or open loop simulations alone, and the spatial sub-pixel variability can be enhanced slightly (not shown). With the additional inclusion of surrounding coarse-scale observations (3D assimilation using multiple coarse-scale observations, "3D-Cm") there is a significant improvement in estimating the sub-pixel variability (bottom row in Figure 1). Furthermore, artificial boundaries in the analysis field, caused by the boundaries in the coarse observations, are completely removed.

It is shown that coarse-scale, synthetic satellite estimates of SWE can improve both the fine-scale SWE spatial mean and variability estimation over the open loop simulations, and the 3D assimilation analyses are always better than either the model simulations or observations alone.

Publication:

De Lannoy, G.J.M., R.H. Reichle, P.R. Houser, K. Arsenault, N.E.C. Verhoest, V.R.N. Pauwels, 2010: Satellite-scale snow water equivalent assimilation into a high-resolution land surface model. *J. Hydromet.*, doi:10.1175/2009JHM1192.1, **11**(2), 352-369.

Assimilation of Terrestrial Water Storage from GRACE in a Snow-dominated Basin

Barton Forman, Rolf Reichle and Matthew Rodell (Code 614.3)

Passive microwave (e.g. AMSR-E) and visible spectrum (e.g. MODIS) measurements of snow states have been used in conjunction with land surface models to better characterize snow pack states, most notably snow water equivalent (SWE). However, both types of measurements have limitations. AMSR-E, for example, suffers a loss of information in deep/wet snow packs. Similarly, MODIS suffers a loss of temporal correlation information beyond the initial accumulation and final ablation phases of the snow season. Gravimetric measurements, on the other hand, do not suffer from these limitations. In this study, gravimetric measurements from the Gravity Recovery and Climate Experiment (GRACE) mission are used in a land surface model data assimilation (DA) framework to better characterize SWE in the Mackenzie River basin located in northern Canada. Comparisons are made against independent, ground-based SWE observations, state-of-the-art modeled SWE estimates, and independent, ground-based river discharge observations.

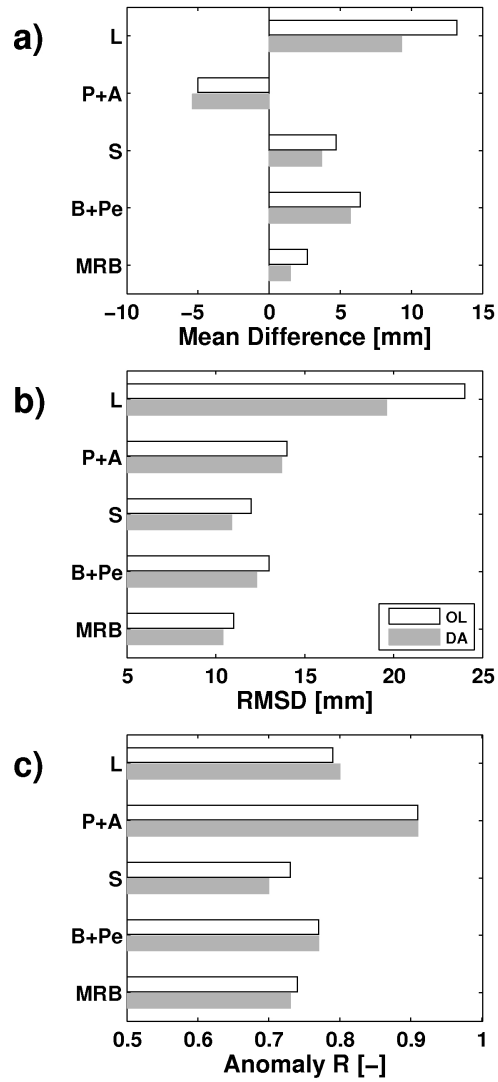

Figure 1: SWE statistics of a) MD, b) RMSD, and c) anomaly R for open-loop (OL; white) and data assimilation (DA; light gray) results relative to Canadian Meteorological Centre SWE estimates via Sturm el al. [2010]. Differences in anomaly R are not statistically different.

Figure 1 shows the improvements in SWE estimation in the GEOS-5 Catchment land surface model resulting from the assimilation of GRACE terrestrial water storage information. The white bars represent model results without assimilation whereas the gray bars represent results with assimilation. Each of the labels on the y-axis of each subplot represents a different studied sub-basin. As shown in Figure 1a, the assimilation of GRACE data significantly reduces the mean difference (MD) between the model and independent observations, particularly in the Liard basin (labeled L in Figure 1) where the greatest amount of snow accumulation occurs. The MD is improved in the majority of the sub-basins. Similarly, the root mean squared difference (RMSD) shown in Figure 1b is reduced as a result of the DA framework. The greatest reduction occurs in the Liard basin with smaller reductions occurring in the other sub-basins. The correlation coefficient of the SWE anomalies (i.e., the average seasonal cycle has been removed to better highlight interannual variability) suggests a slight degree of degradation resulting from assimilation, but further analysis shows there is no statistically significant difference on a 5% confidence interval. That is, one must conclude that there is no difference in the anomaly correlations between results with or without assimilation. In summary, the assimilation of

GRACE terrestrial water storage information into the Catchment land surface model reduces the MD and RMSD in SWE estimates without adversely impacting its ability to estimate interannual variability.

Additional work was conducted to analyze modeled river discharge estimates against ground-based gauging stations. The findings (results not shown) suggested the assimilation of GRACE observations causes little of no change in the MD and RMSD of modeled river discharge; however, small, statistically significant improvements in the anomaly correlations were found. Improvements in the modeled river runoff anomalies are attributed to a redistribution of the water mass from the snow pack during the accumulation phase into the subsurface during the subsequent ablation and runoff phase. This redistribution of water mass by the DA framework effectively retains water mass within the hydrologic basin for a longer period of time, which results in small but statistically significant improvements in modeled estimates of river discharge.

Results presented here suggest improved SWE estimates, including improved timing of the subsequent ablation and runoff of the snow pack. Additionally, use of the DA procedure has the potential to add vertical and horizontal resolution to the coarse-scale GRACE measurements as well as downscale the measurements in time. Such findings offer better understanding of the hydrologic cycle in snow-dominated basins located in remote regions of the globe where ground-based observation collection is difficult, if not impossible. This information could ultimately lead to improved freshwater resource management in communities dependent on snow melt as well as a reduction in the uncertainty of river discharge into the Arctic Ocean**.**

This work is a first step in GMAO towards utilizing space-based gravimetric measurements for the purpose of improved freshwater resource characterization where snow is a significant contributor to the hydrologic cycle. Future experiments could include visible and passive microwave measurements from existing instruments such as MODIS and AMSR-E to further downscale the GRACE observations in time and space while simultaneously disaggregating the GRACE observations into individual, vertical components of TWS. Finally, additional improvements could be achieved through refining the GRACE measurement error model, investigating the effects of different horizontal error correlation lengths within the land surface model forcings, determining a more optimal GRACE measurement scale, utilizing a more optimal GRACE averaging kernel, and enhanced constraining of post-glacial rebound model estimates used during GRACE preprocessing.

URL: http://gmao.gsfc.nasa.gov/research/landsurface/tws.php

Publication:

Forman, B.A., R.H. Reichle, and M. Rodell, 2011: Assimilation of Terrestrial Water Storage from GRACE in a Snow-dominated Basin. *J. Geophys. Res.,* (in review).

Reference:

Sturm, M., B. Taras, G.E. Liston, C. Derksen, T. Jonas, and J. Lea, 2010: Estimating Snow Water Equivalent Using Snow Depth Data and Climate Classes. *J. Hydromet.,* **11**, 1380-1394.

The Impact of ENSO and the AO on Winter Temperature Extremes in the Southeast United States

Young-Kwon Lim and Siegfried Schubert

Interannual variations of the winter mean temperature and the number of days of temperature extremes were investigated for the southeast U.S. to identify the relative influence of El Niño/Southern Oscillation (ENSO) and the Arctic Oscillation (AO).

The temperature data used in this study are from the Cooperative Observer Program of National Weather Service for the December, January, February (DJF) winter seasons from 1951 to 2008. The station data encompass Florida, Georgia, Alabama, South Carolina, and North Carolina. After gridding the station data, seasonal means and the extreme indices were calculated at each grid point for all 58 winters. The values for each year were then averaged over the southeast U.S. domain. The resulting year-to-year variation is plotted in Figure 1, with the AO and Southern Oscillation (SO) indices obtained from NOAA's Climate Prediction Center. The top and middle panels reveal the extent to which the seasonal mean temperature anomalies co-vary with these two indices. The top panel suggests a substantial link to the AO index (correlation is 0.59). The middle panel shows that the temperature anomalies also appear to have some coherence with the SO index, but only for the period before 1980 (correlation is 0.36 before 1980). After 1980, the correlation with the SO index drops to 0.07, suggesting that ENSO had essentially no impact on the mean temperature anomalies for the recent 28 years. The correlation coefficient for the entire 58 years is 0.20, which is not significant at the 5% confidence level. Here we have chosen to compute the correlations separately for the periods 1951-1980 and 1981-2008 because the coherent variation between SO and the temperature anomalies appears to weaken after the early 1980s. The strong out-of-phase relationship between warm and cold extreme indices also appears to break down beginning in the early 1980s (Figure 1c). This separation also allows the estimation of the correlation for the generally negative phase of AO before 1980. Compared with the SO index, the AO index exhibits better agreement with the seasonal temperature anomalies. In particular, the correlation coefficients are greater than 0.6 for both the earlier (0.62) and the later (0.63, compared with 0.07 for the SO) period.

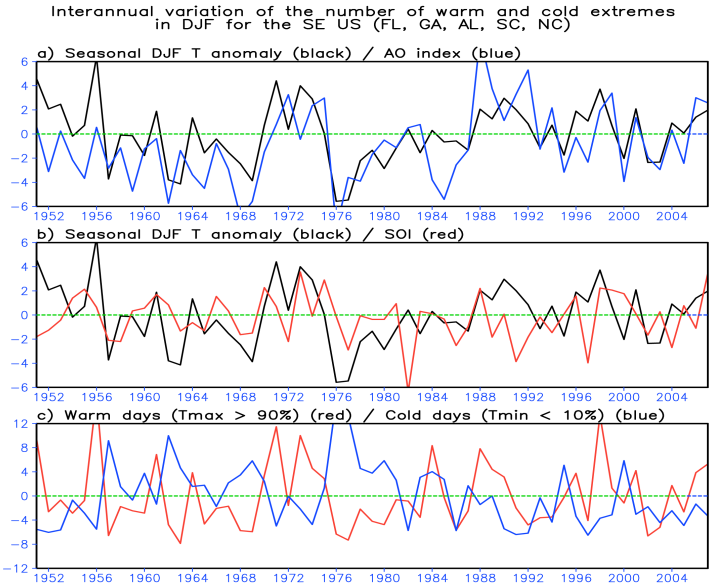

Figure 1: Year-to-year variation of the winter temperature anomaly area-averaged over the southeast U.S. (black line) in the top and middle panel, Arctic Oscillation (AO) index (blue line) (multiplied by 3) in the top panel, and Southern Oscillation (SO) index in the middle panel for the period of 1951 to 2008. The positive SO index indicates La Niña phase, whereas the negative SO the El Niño phase. The bottom panel represents the year-to-year variation of the warm extreme indices (red line) and cold extreme indices.

The indices of the warm and cold extremes are defined as the anomalies in the DJF counts of the warm and cold days, respectively. A day was determined to be extremely warm (cold) if the daily maximum (minimum) temperature exceeds (falls below) the 90th (10th) percentiles of daily maximum (minimum) temperature within a 5-day moving window over the 1951 to 2008 period. The bottom panel in Figure 1 shows the interannual variation of the warm (red) and cold (blue) extreme indices. The warm extreme time series fluctuates with nearly opposite phase to the cold extreme time series prior to 1980 (correlation is -0.67). After 1980, the strong negative relationship between these two time series diminishes (correlation is 0.13), as seen in several years (e.g., 1984, 1986, 1991, 1992, 1994, and so on) that exhibit the same-signed anomalies of warm and cold extreme indices in those years. The generally accepted idea that El Niño gives rise to a colder climate whereas La Niña causes a warmer climate in this region does not appear to apply after about 1980.

We analyze the extremes and the impact of ENSO and AO further by fitting the extreme indices to the Generalized Extreme Value (GEV) distribution. Separate fits were produced for the years with positive (the 19 years with AO index greater than 0.1) and negative (the 36 years with AO index less than -0.1) AO phases. Similarly, separate fits were produced for the 19 El Niño (negative SO index), and the 16 La Niña (positive SO index) years, as well as for the full 58-year period. Figures 2a and 2b depict the PDF estimates as a function of the AO phase. It is clear that the PDF curve for warm extremes is shifted to the right in the positive AO phase compared with the negative AO, indicating more frequent warm extreme events in the positive AO phase (Figure 2a). The tail of the distribution is also heavier, indicating a greater chance of very large positive extremes during the positive AO phase. In contrast, Figure 2b shows that cold extreme events are more likely in the negative AO phase, as indicated by the fact that the blue curve (negative AO) is shifted further to the right (and with a heavier tail) compared to the positive AO phase.

ENSO also turns out to have a substantial impact on the warm extremes. Figure 2c shows that La Niña (positive SO index) plays a significant role in causing more frequent warm extremes compared with El Niño (negative SO index). This is in contrast with the cold extremes for which the two distributions are not statistically distinguishable, especially for the tail of the distribution. The other three PDF differences in Figures 2a, 2b, and 2c are significant.

In summary, the analysis reveals that both the winter mean temperature anomalies and the number of days of extreme cold are most closely linked to variations in the AO especially in the more recent years (1981-2008). In contrast, the number of days of extreme warmth are linked to both ENSO and the AO. It is anticipated that these results will contribute to the assessment of on-going high-resolution GEOS-5 model simulations of extremes over the United States.

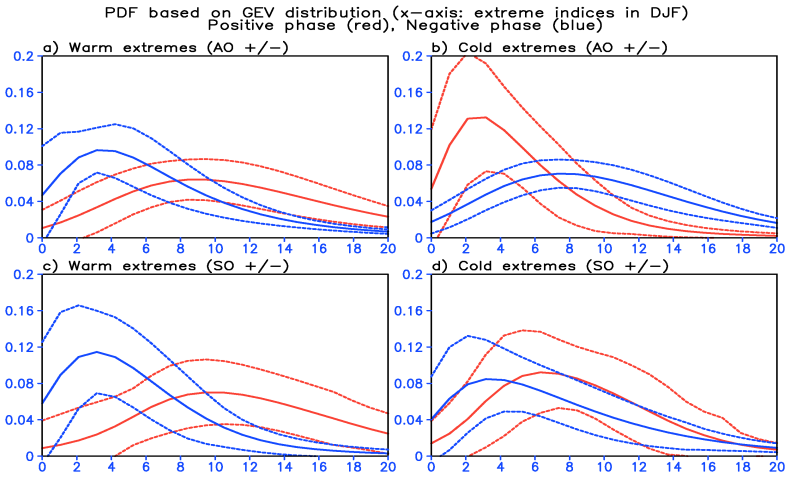

Figure 2: Probability distribution function (PDF) (solid lines) warm extreme indices (left panel) and cold extreme indices (right panel) for different AO +/- and SO +/- phases. The PDF curve for positive (negative) phase is red (blue). Dashed curves denote the 95% confidence interval. The abscissa denotes the extreme indices value, the ordinate the probability.

Attribution of the Extreme U.S. East Coast Snowstorms of 2010

Yehui Chang, Siegfried Schubert and Max Suarez

This study examines the cause of the extreme snowstorm activity along the U.S. east coast during the winter of 2009/10 with a focus on the role of sea surface temperature (SST) anomalies associated with a mature El Niño and a persistent negative North Atlantic Oscillation (NAO). The study employs the GEOS-5 atmospheric general circulation model (AGCM) run globally at high resolution (0.25° and 0.5°) and forced with specified observed or idealized SST. The simulations consist of 50-member ensembles of three-month long simulations (initialized December 1) aimed at assessing the roles of the Pacific and Atlantic SST anomalies. Comparisons are made with the winter of 1999/2000 – a period that is characterized by SST anomalies that are largely of opposite sign.

Anomalies in Simulation and in MERRA. Figure 1 shows the 250 hPa height, precipitation and surface temperature anomalies computed as the difference between the two Februaries (2010-2000). The ensemble mean model results are compared with what actually occurred as estimated from MERRA. The height response is characterized by what is, to a large extent, a well-known response to El Niño, with an anomalous trough over the North Pacific, a positive height anomaly over Canada, and a negative anomaly over the United States. An unusual aspect of the response is the extension of the anomalies eastward across the Atlantic and into Europe, a region not typically associated with a strong ENSO signal. The single instance from MERRA shows generally similar features, though noisier and with larger amplitude. In particular, there is a short wave (wave number 5 - 6) anomaly that extends from Asia across the Pacific and is absent from the ensemble mean. The Southern Hemisphere also shows considerably more wave structure than the model results. Nevertheless, the basic structure of the height anomalies that occur over North America, the Atlantic and Europe, are quite consistent with the model ensemble mean anomaly patterns.

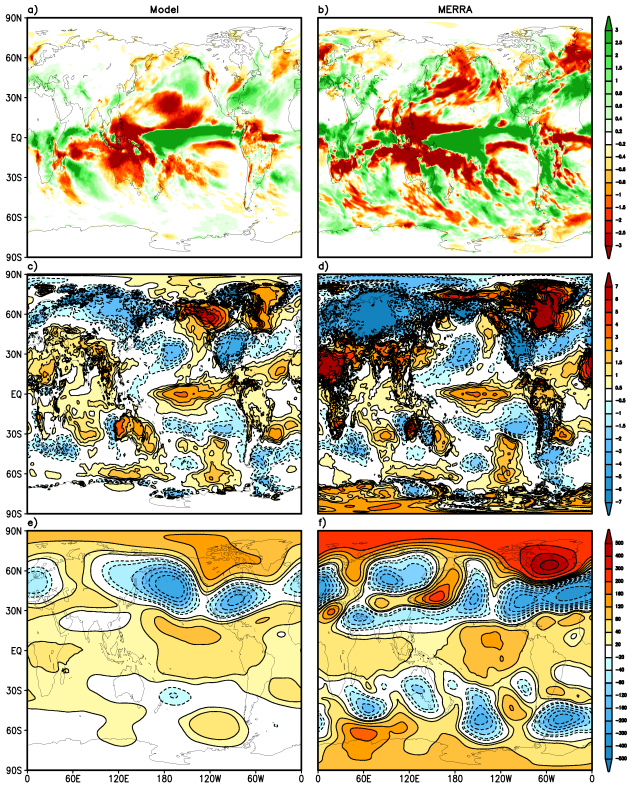

Figure 1: Left panels: Fifty- member ensemble mean of GEOS-5 hindcasts run at 0.25°x0.25° lat/lon resolution. The results are the differences between February 2010 and February 2000. Top: the precipitation differences (mm/day). Middle: the surface temperature differences (°C). Bottom: the 250mb height differences (meters). Right panels: the corresponding MERRA results.

The precipitation anomalies from the ensemble-mean model simulations and MERRA also show very consistent features. There is a clear ENSO response in the Pacific, with enhanced precipitation in the central tropical Pacific and reduced precipitation to the north and south and to the west over the region of the warm pool. Focusing on the Northern Hemisphere, both also show enhanced precipitation in the southeastern U.S., extending northward along the east coast – suggesting enhanced storm activity in this region. The positive precipitation anomalies extend eastward from the U.S., across the Atlantic and into southern Europe and

Asia. Other regions of reduced precipitation include the west coast and Great Lakes regions of the U.S., the east coast of Greenland, the Greenland Sea, and Norway.

The surface temperature differences reflect the February 2010 positive SST anomalies in the tropical Pacific associated with an evolving El Niño, and the negative anomalies of 1999/2000 associated with a La Niña. The North Atlantic SST differences resemble the tri-polar structure associated with the Atlantic Multi-decadal Oscillation with (during 2010) positive SST anomalies in the high latitudes, negative anomalies in the middle latitudes and positive anomalies in the subtropics. This is also associated with a persistent negative phase of the NAO during 2010. During 2000 the North Atlantic SST anomalies are less well defined although they also show a tendency to be of opposite sign to those during the 2009/2010 winter.

The precipitation differences over the eastern U.S. are positive, reflecting a more active storm track during 2010. Also, the surface temperature differences reflect colder conditions during 2010 that extend over much of the continental U.S. We next isolate the impacts of the North Atlantic SST by running a third set of simulations in which the SST fields in the Atlantic (between 10°S to 75°N) are switched between the two winters. In order to facilitate further experimentation, we first repeated the above runs at 0.5° resolution. The results (not shown) indicate that the basic features of the responses are essentially unchanged at the somewhat coarser resolution. The full set of runs is described in Table 1.

Attribution – Isolating the Impacts. Using these runs, we isolate the impact of the North Atlantic SST by computing:

$$NAtl\ Impact = \{(B\text{-}A) - (D\text{-}C)\}/2. \quad (1a)$$

Furthermore, the North Atlantic SST impacts are different during 2000 (the La Niña year) and 2010 (the El Niño year). This is quantified as:

$$NAtl\ Impact_{2000} = (C\text{-}A) \quad (1b)$$
$$NAtl\ Impact_{2010} = (B\text{–}D). \quad (1c)$$

The runs also allow us to isolate the impacts of ENSO by computing:

$$ENSO\ Impact = \{(B\text{-}A) + (D\text{-}C)\}/2. \quad (2a)$$

Furthermore, the ENSO impacts can be differentiated according to the sign of the North Atlantic SST. This is quantified as:

$$ENSO\ Impact_{(negNatl)} = (B\text{–}C) \quad (2b)$$
$$ENSO\ Impact_{(posNatl)} = (D\text{-}A). \quad (2c)$$

The results (Figure 2) highlight the dominance of the ENSO impact over the United States on both the surface temperature (the cooling associated with El Niño) and precipitation (enhanced precipitation along the east coast). The main impact of the North Atlantic SSTs is to reduce the precipitation west of the Appalachians, and cool the eastern U.S. It is noteworthy that the impact of the North Atlantic SST on surface temperature over the U.S. is strongly dependent on the phase of ENSO, with cooling during the El Niño year (2010), and warming during the La Niña year (2000).

The results show that the model is able to reproduce the main features of the observed changes including the enhanced storminess along the east coast. Experiments that attempt to isolate the role of the North Atlantic SST indicate that the anomalies over the U.S. are to a large extent driven by El Niño, while the impact of the North Atlantic SST is primarily to contribute to the cooler temperatures along the U.S. east coast.

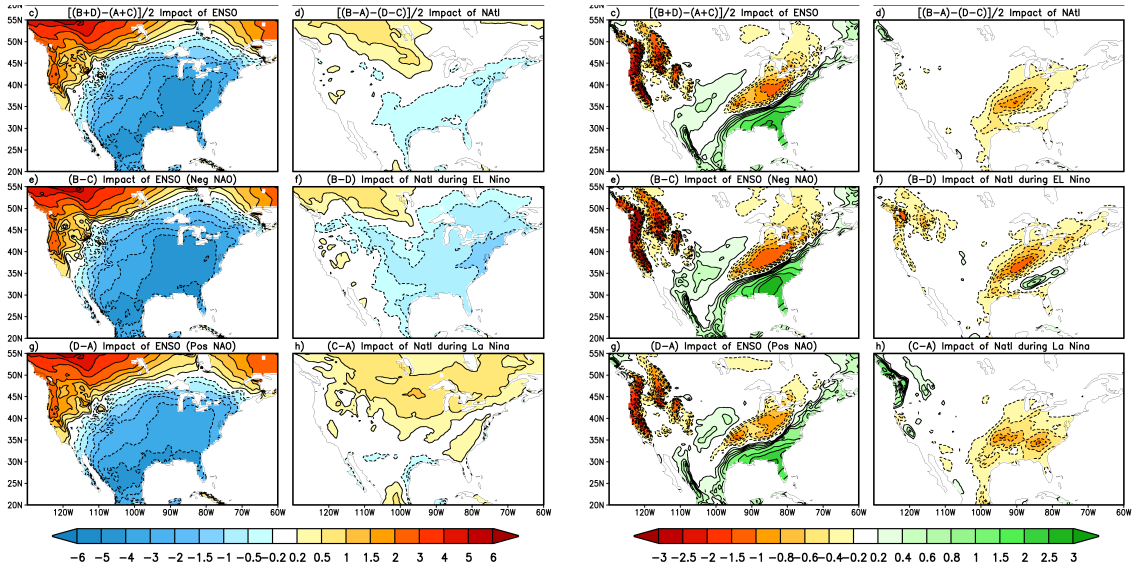

Figure 2: Left six panels: The impact of various SST forcing on February surface temperature (°C) over the U. S. The left-most panels show the impact of ENSO and how that varies depending on the sign of the North Atlantic SST. The next set of three panels shows the impact of the North Atlantic SST and how that varies with ENSO phase. The right-most 6 panels are the same as those on the left but for precipitation (mm/day). See text for details.

***Table 1**. The GEOS-5 hindcast experiments. The "Switched NA" runs have the SST fields in the Atlantic (between 10°S to 75°N) switched between the two winters.*

Resolution	Initial Date		SST
	Dec 1, 1999	Dec 1, 2009	
0.25°	A´	B´	Observed
0.50°	A	B	Observed
0.50°	C	D	Switched NA

Publication:

Chang, Y., S. Schubert, and M. Suarez, 2011: Attribution of the extreme U.S. East Coast snowstorm activity of 2010. *J. Climate* (in press).

MERRA Observing System Studies

Michael G. Bosilovich, Franklin R. Roberson (MSFC) and Junye Chen (UMd/ESSIC)

The Modern-Era Retrospective analysis for Research and Applications (MERRA) represents the integration of many diverse Earth observations into a model, yielding data with consistent format across weather and climate time scales. There are several advantages to the methodology. First, the model component can produce ancillary variables not easily observed, but strongly guided by the assimilated observations. Second, we can learn a great deal about the model biases due to the confrontation of model and observations during the assimilation process. Here, our goal is to exploit the breadth of MERRA output to characterize the model biases to better understand the MERRA data and its use in weather and climate studies, ultimately contributing to the next generation of reanalysis data assimilation.

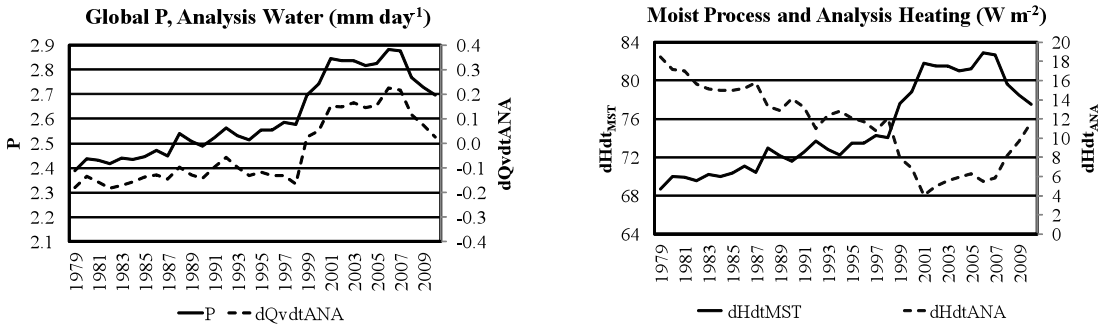

Figure 1: Annual mean time series of (a) precipitation and water vapor analysis increment from the water budget and (b) atmospheric latent heating (MST) and heating analysis increment from the energy budget.

Included in MERRA diagnostics are complete budget terms for the water and energy cycles. Bosilovich et al. (2011) evaluate the global energy and water budgets of MERRA, finding several improvements over the previous generation of reanalyses. However, the time series analysis shows that the changing observing system has a noticeable effect on budgets. Figure 1 shows the time series of the water budget's precipitation and the analysis increment, and the energy budget's atmospheric latent heating along with the heating increment. These increments are computed from the difference between model forecasts and observations, and they change in time, as newer observing systems become active, and as older satellites are decommissioned. The addition of the Advanced Microwave Sounding Unit (AMSU) is noticeable in 1999 and 2001, changing the sign of the water increment and affecting precipitation (i.e., latent heating) and other water, heat and radiative fluxes. As some instruments are removed in the late 2000s, the increments revert to prior levels.

In a companion study, Robertson et al. (2011) used Principal Component Analysis (PCA) to investigate the evolution of the water vapor increments. The first dominant mode resembles the timing of major satellite observing system changes (Figure 2). Specifically, the jumps in precipitation at the introduction of the Special Sensor Microwave Imager (SSMI) at the end of 1987 as well as AMSU in 1999 are both apparent. Projecting MERRA fluxes onto the PCs of the leading modes of the assimilation increment, which are dominated by these artifacts, enabled their

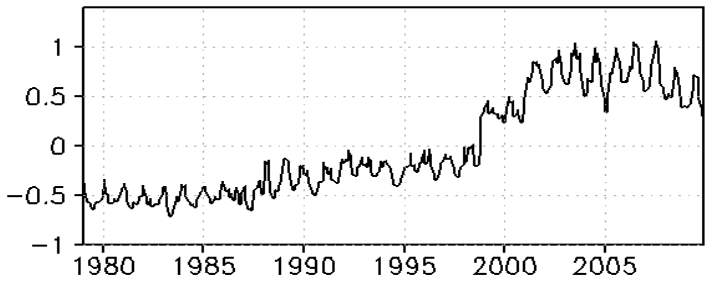

Figure 1: Principal component (PCs) for modes 1 of the vertically-integrated moisture increment, ANAq. The fractional variance explained for this mode is 18%, referring to departures from the monthly varying annual mean defined by the period 1979-2009.

removal from the original data. For precipitation, this procedure results in an anomaly time series that is free of the spurious jump/trend and that much more closely follows the observed anomaly time series (Figure 3). This correction has been applied to other terms of the water and energy cycles as well.

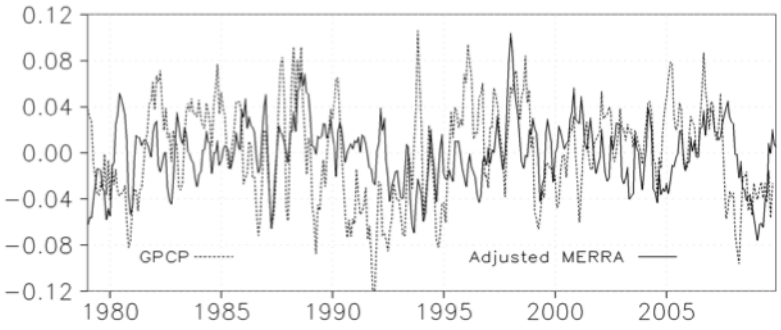

Figure 3: MERRA precipitation anomalies adjusted due to the analysis increment EOF (solid) compared to GPCP merged satellite observational data (dotted), averaged over +/- 60°. Units are mm day^{-1}.

In addition to the satellite data, radiosonde observations play a significant role in the reanalysis, and on occasion they can have detrimental impacts. For example, a lone radiosonde in central Africa (station Bangui) changed its instrument in 1995, resulting in lower values of specific humidity compared to the history of the station. This leads to significant anomalous features across central Africa in MERRA. Table 1 shows some statistics generated by the assimilated observations from MERRA (specifically the observation minus forecast and observation minus analysis). In computing Contextual Bias and Effective Gain from the reanalysis, we can see the change of the station in the resulting analyses (Table 1). This shows that the analysis does not agree with this station's 12Z specific humidity after 1995. We are pursuing further analysis with this diagnostic to better assess the observing system assimilated for the reanalysis, and hope to improve the observation quality for the next reanalysis.

Ultimately, the assimilated data (temperature, wind and humidity) are reliably reproduced in reanalyses. Figure 4 shows the anomaly time series of brightness temperatures in the lower troposphere from an MSU/AMSU merged product. MERRA reproduces the observed variability very well.

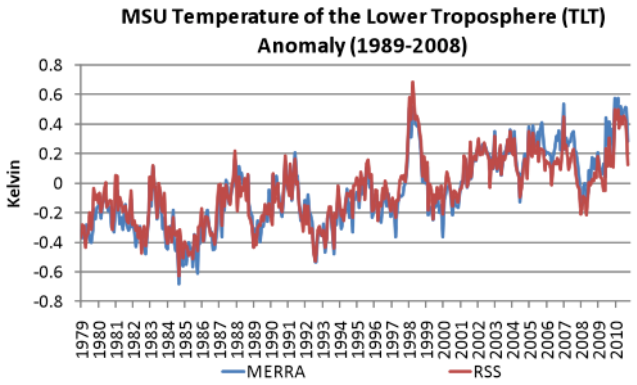

Figure 4: MSU brightness temperature weighted for the lower troposphere (TLT) from Remote Sensing Systems (RSS) compared to MERRA TLT. The anomaly is taken from the mean annual cycle of the base period, 1989-2008.

Table 1. *Contextual bias (CB) and Effective gain (EG) computed for Bangui Africa 850 hPa temperature and specific humidity. Note the increase in CB of 12Z specific humidity observation after 1995.*

850mb	(CB/EG)	12Z		00Z	
q	79-95	0.05	*0.43*	-0.02	*0.43*
	96-09	0.17	*0.56*	-0.02	*0.51*
T	79-95	-0.03	*0.80*	-0.01	*0.79*
	96-09	0.00	*0.80*	0.02	*0.77*

Publications:

Bosilovich, M.G., F.R. Robertson, and J. Chen, 2011: Global Energy and Water Budgets in MERRA. *J. Clim. MERRA Special Issue* (in press).

Robertson, F. R., M. G. Bosilovich, J. Chen, and T. L. Miller, 2011: The Effect of Satellite Observing System Changes on MERRA Water and Energy Fluxes. *Clim. MERRA Special Issue* (in press).

An Effort to Minimize the Inhomogeneities in MERRA

Junye Chen, Michael G. Bosilovich and Franklin Robertson (MSFC)

The latest generation of reanalyses, such as MERRA, shows major improvements over the previous generation of reanalyses. However, because of changes in the observing system over time, temporal homogeneity remains one of the most challenging issues for reanalyses, especially for research studies focused on climate trends.

In order to use MERRA products in climate change trend research, it is necessary to identify the impacts of observing system changes on the reanalysis and homogenize the product over time. In this project, we aim to minimize the inhomogeneity in MERRA by augmenting it with several reanalysis segments, each being performed for a period of about one year when a major observing system change happens. Each of these reanalysis segments will be similar to the corresponding segment of original MERRA, except that the new observation data type introduced at that time is excluded. These reanalysis segments are termed the Reduced Observing System Segment (ROSS) experiments. By comparing each ROSS with the original MERRA stream, impacts of the changes in observing system will be identified and patches produced to minimize those impacts. With the patches, the MERRA data in the period before each ROSS run will be adjusted to offset the difference caused by the observing system change. That is, MERRA data in earlier periods will be homogenized to match the more recent MERRA data, which should be of better quality with most recent advanced set of observations.

Two ROSS experiments have been conducted to date. In the first ROSS, SSM/I data was withheld from July 1987 to August 1989 to identify the impact of the introduction of SSM/I radiances and surface wind retrievals in July 1987. In the second ROSS, NOAA-15 data was withheld over the period from September 1998 to December 2000 to address the impact of the introduction of ATOVS instruments onboard the NOAA-15 satellite in late 1998.

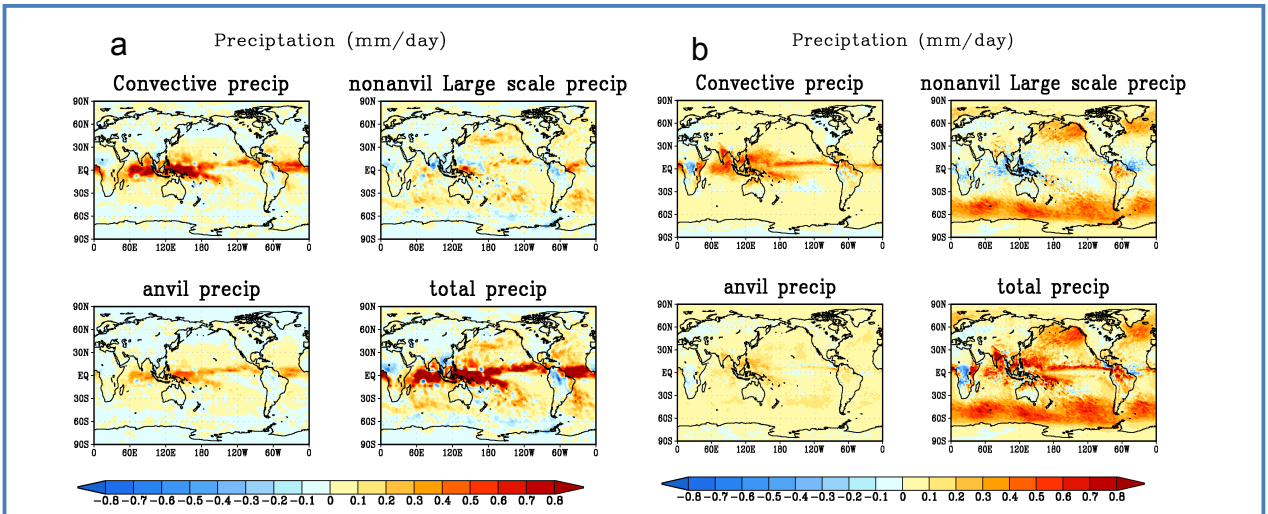

Figure 1: The mean impacts on precipitation in MERRA from the introduction of (a) SSM/I and (b) NOAA-15.

Comprehensive analysis has been conducted on both ROSS experiments. We found significant impacts from SSM/I and NOAA-15 in almost all variables, although the impacts not evenly distributed in space and are not of the same level for all variables. The responses of moisture and dynamical processes to the introduction of new observation types are closely related, but the changes in different variables are not linearly related. There are also significant differences between the impacts from these two satellites. For

example, the change of precipitation caused by SSM/I data mainly occurs in the tropical convective regions as convective precipitation (Figure 1a, upper left). There are much smaller, although noticeable positive changes in non-anvil large-scale precipitation and anvil precipitation (Figure 1a, upper right and lower left). On the other hand, the impact of NOAA15 is significant in both convective precipitation (Figure 1b, upper left) and non-anvil large-scale precipitation (Figure 1b, upper right). The different impacts in precipitation imply different mechanisms and adjustments in the model to the two different data types.

We also tested the first order homogenization based on the difference between monthly spatial patterns from the original MERRA data and two ROSS experiments. The two jumps in the MERRA time series associated with the introduction of SSM/I and NOAA-15 observations are essentially removed as shown, for example, in the zonal mean precipitation time series (Figure 2) and global mean precipitation time series (Figure 3). It is worthwhile to mention that the artificial trend in the original precipitation time series is largely diminished after the adjustment, because both jumps removed are positive. Clearly, even this sort of simple correction could be of benefit to studies of trends using MERRA. In the coming few months, more ROSS experiments will be produced and a more sophisticated adjustment method will be developed so that the homogenization outcome will be significantly improved.

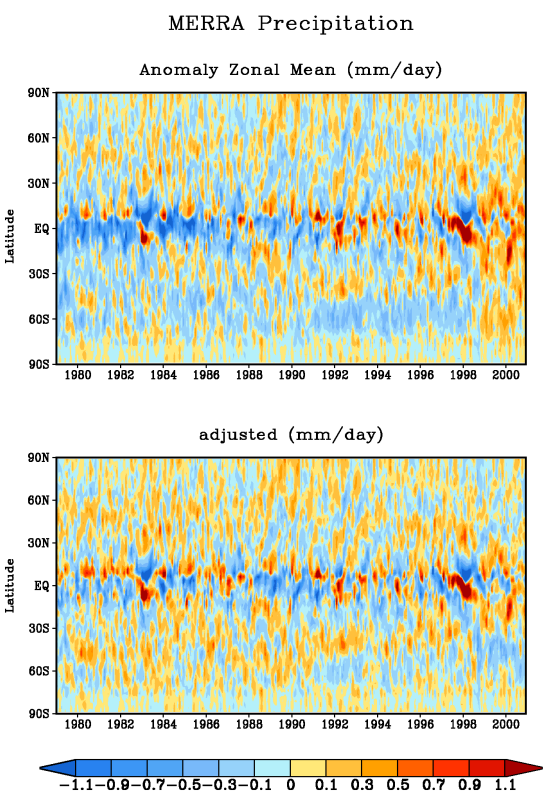

Figure 2: (Upper) The time series of zonal mean anomaly of the original precipitation product from MERRA; (Lower) the adjusted precipitation anomaly time series based on two ROSS experiments.

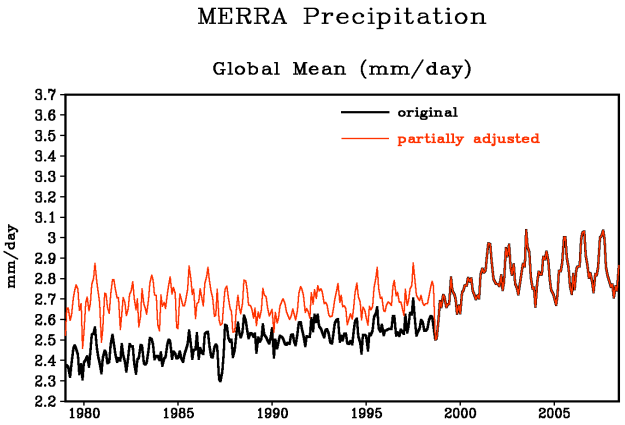

Figure 3: The original global mean precipitation (black) and the adjusted global mean precipitation (red) based on two ROSS experiments.

GLACE-2: The Second Phase of the Global Land-Atmosphere Coupling Experiment

Randal Koster, Sarith Mahanama, and 21 contributors from multiple institutions

GLACE-2, the second phase of the Global Land-Atmosphere Coupling Experiment, is aimed at quantifying, across a broad suite of state-of-the-art forecast models, the subseasonal (out to 60 days) forecast skill associated with the initialization of land surface state variables. GMAO scientists coordinated the international experiment and took the lead in processing the results. They also provided two of the submissions to the experiment; one using the original NSIPP forecast system and other using the new GEOS-5 system. First results from the experiment were presented in Koster et al., 2010. Here we report on two new results.

In GLACE-2, the same numerical experiment, one specifically designed to isolate soil moisture initialization impacts on subseasonal forecast skill (as measured against real observations), was performed with eleven independent forecast systems. Participants in GLACE-2 performed two series of 2-month, 10-member ensemble forecasts covering a wide range of boreal warm-season start-dates: 10 start dates per year (April 1, April 15, May 1, ... August 15) for each of the years 1986-1995. The two series differed from each other only in the nature of their land surface initialization: in Series 1, land conditions (particularly soil moisture) were initialized to realistic values based on an offline integration of historical meteorological forcing, and in Series 2, realistic land surface initialization was not utilized. Forecasted 15-day precipitation and air temperature averages were compared to the corresponding observations, with skill measured as the square of the correlation coefficient between them; by subtracting the forecast skill obtained for Series 2 from that obtained for Series 1, we isolated the impacts of soil moisture initialization on the skill. All forecasts performed in GLACE-2 were true forecasts in that they made no use of information from the forecast period itself.

Demonstration of the Need for Adequate Monitoring Networks. Figure 1 provides, for air temperature forecasts, a joint look at the limitations imposed by underlying model predictability and by the accuracy of the initialization. Each plotted dot in the scatter plot corresponds to a 2°×2.5° grid cell that is at least 90% land. The abscissa assigned to a given dot is determined from its underlying model consensus predictability (a derived measure of the degree to which atmospheric chaos will necessarily foil a forecast; see Koster et al., 2011 for details), and the ordinate is determined from the local rain gauge density (a surrogate for the accuracy of the land moisture initialization). The size and color of the dots are keyed to the land-derived skill uncovered by the GLACE-2 experiment for air temperature forecasts at 30-45 days. The salient result from the figure is the strong impact of both underlying model predictability and gauge density on the ability to extract true skill from the experiments. As expected, skill appears only where the background predictability is sufficiently large. For the most part, skill also appears only for higher values of gauge density – the plots suggest that a density of about 10 gauges per 2°×2.5° cell is needed to produce the larger values of skill in the forecasts. (Similar suggestions of gauge density impact are also seen in corresponding scatter plots for precipitation [not shown], though the signal is weaker.)

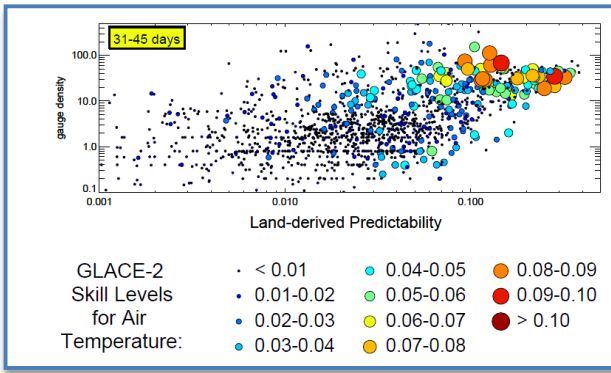

Figure 1. Air temperature forecast skill at 31-45 days as a function of background consensus predictability (x-axis) and gauge density (y-axis). Each dot corresponds to a 2°x2.5° land grid cell; the size and color of the dot (see legend) reflect the land-derived air temperature forecast skill computed for the location by GLACE-2.

Such a plot shows correlation rather than causation; it does not prove that higher densities are responsible for higher forecast skill. Even so, Figure 1 strongly supports the idea that if precipitation (and perhaps air temperature, for verification) were monitored more comprehensively during the 1986-1995 period, additional air temperature forecast skill might indeed have been computed in GLACE-2 at many of the grid cells for which the land-derived predictability is high but the gauge density is low. This result underscores the importance for the forecasting problem of observational networks, both in terms of rain gauge networks and, for present-day, satellite-based observations of precipitation and soil moisture.

Wet versus Dry Initialization. GLACE-2 can begin to address the question of wet/dry asymmetry in prediction – to what degree can anomalously wet conditions contribute more to a forecast than anomalously dry conditions, or vice-versa? The top panel of Figure 2 shows the land-derived skill for air temperature prediction at the 30-day lead (Days 31-45) in the continental United States for exactly half of the start dates considered: those for which the initial soil moisture at the local grid cell lies in the lower half of all the values realized (i.e., the times for which the local soil is initialized anomalously dry, in a median sense). The bottom panel shows the corresponding skill for the wettest start dates. The distinction is clear: dry initial conditions lead to greater skill in the north central United States, whereas wet initial conditions lead to more skill toward the southwest. This distinction is more than just anecdotal; this GLACE-2 result is fully consistent with known hydrologic concepts regarding wet/dry asymmetry. Due to the shape of the soil moisture-evaporation relationship, evaporation in the north central U.S. varies with soil moisture more for drier conditions than for wetter conditions, whereas the reverse is true for the southwest. See the Koster et al. (2011) paper indicated below for more information.

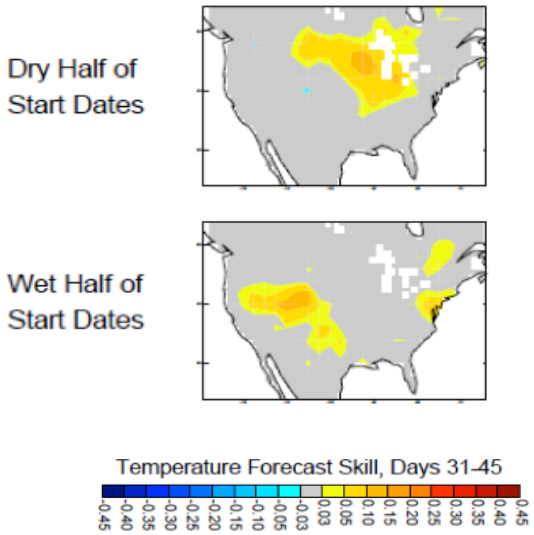

Figure 2: Differences in skill generated for dry (top panel) and wet (bottom panel) initializations.

URL: http://gmao.gsfc.nasa.gov/research/GLACE-2/

Publications:

Koster, R.D., S.P.P. Mahanama, and 21 co-authors, 2010: Contribution of land surface initialization to subseasonal forecast skill: First results from a multi-model experiment. *Geophys. Res. Lett.*, **37**, L02402, doi:10.1029/2009GL041677.

van den Hurk, B., F. Doblas-Reyes, G. Balsamo, R.D. Koster, S. Seneviratne, and H. Camargo Jr., 2011: Soil moisture effects on seasonal temperature and precipitation forecast scores in Europe. *Climate Dynamics* (*in press*).

Koster, R.D., S.P.P. Mahanama, and 21 co-authors, 2011: The second phase of the Global Land-Atmosphere Coupling Experiment. *J. Hydromet*. (*in press*).

Advances in the Analysis of Seasonal Streamflow Prediction

*Randal Koster, Sarith Mahanama, Ben Livneh**, Dennis Lettenmaier** and Rolf Reichle*
**Dept. of Civil Engineering, University of Washington

In this project, we quantify the individual contributions of snow and soil moisture initialization to seasonal forecast skill in a streamflow forecast system using (i) multi-decadal naturalized streamflow measurements covering much of the United States, (ii) a suite of state-of-the-art land surface modeling systems (the GMAO catchment, VIC, Noah, and Sacramento land surface models (LSMs)), and (iii) true forecast (hindcast) experiments.

The four models were first integrated in a control simulation (CTRL) over the period 1920 through 2003 on a 0.5° grid covering the contiguous U.S. (CONUS) using an hourly, observations-based, surface meteorological forcing data set. Three sets of forecast experiments (Exp1, Exp2, and Exp3) were then performed with each LSM, experiments designed to quantify the degree to which streamflow can be predicted at various leads assuming no skill in the seasonal prediction of meteorological forcing.

In Exp1, 83 separate 1-year forecast simulations (one for each year of the period 1920-2002) were run after being initialized on January 1 with the January 1 snowpack and soil moisture states produced by CTRL for the year in question. To represent a lack of knowledge of meteorological forcing during the forecast period, the LSM was integrated over the forecast year with the climatological seasonal cycle of diurnal forcing determined from the CTRL forcing files; thus, any skill generated in the forecasted streamflows is attributable to the initialization alone. The 1-year forecasts of Exp1 were then repeated with February 1 initializations, with March 1 initializations, and so on through December 1, for a total of 996 1-year forecasts (83 forecast years, with 12 start dates per year).

Exp2 is identical to Exp1, except that soil moisture was initialized on the forecast start date to the climatological distribution of soil moisture on that start date; thus, in Exp2, no forecast skill was derived from soil moisture initialization, but relied solely on snow initialization for skill.

Analogously, Exp3 is identical to Exp1, except that snow amounts were initialized to the climatological fields on the given start date; thus, Exp3 relied solely on soil moisture initialization for forecast skill.

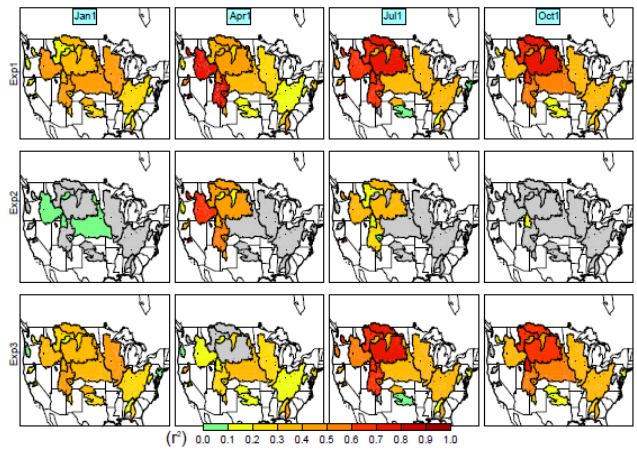

Figure 1: Skill (measured as r^2 against naturalized observations) of multi-model ensemble 3-month streamflow forecasts at 0-month lead, for four start dates (columns) and the three experiments (rows). Gray shading indicates that skill levels are not significant at the 95% confidence level.

Forecast skill as a function of lead and start date. An extension of the original experiment (which was discussed in the 2009 annual report) allows the quantification of the seasonal variation of soil moisture and snow contributions to forecast skill. In Figure 1, the 23 basins for which we have naturalized streamflow data are color-coded according to the skill levels obtained for forecasted average streamflow in the first three months following the forecast start date, with results for Exp1, Exp2, and Exp3 shown in the first, second, and third rows, respectively. Snow initialization dominates the skill contributions for April 1 starts, but soil moisture initialization dominates in the other seasons, sometimes to a very large extent. Figure 2 shows, for a representative basin (the Arkansas River Basin upstream of Ralston), how skill decreases with increasing lead time for each of the 12 start dates. This figure shows that for this basin, November

initializations contribute to skill at leads of several months, whereas June initializations provide little skill even at 1-month lead.

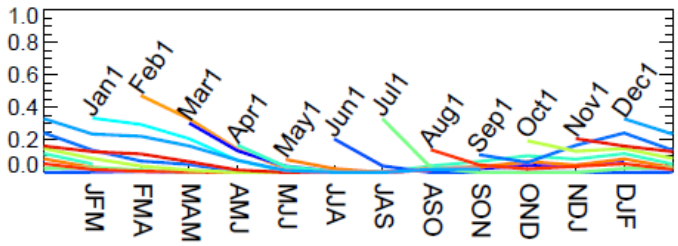

Figure 2: Skill (r^2) of 3-month forecasts produced in Exp1 for the Arkansas River upstream of Ralston, as a function of start date and lead. Curves of a single color provide results for forecasts of a specific start date. The leftmost point on a curve indicates a zero lead for the forecast; points farther to the right on the curve (except for the wrap-around at the end of the year) indicate a longer lead time.

Estimation of skill attainable in ungauged basins. Geographical and seasonal variations in forecast skill were examined in the context of two assumed first-order controls: the land surface's water content, W, at the start of the forecast period and the precipitation, P, during the forecast period. A higher interannual standard deviation of W (σ_W) implies a greater impact of initial conditions on interannual streamflow variations, and thus, under the assumption that W can be estimated reasonably well through offline land modeling, higher prediction skill. In contrast, under the assumption that precipitation is unpredictable during the forecast period, a higher standard deviation of P (σ_P) implies lower streamflow prediction skill. We indeed find evidence (not shown here) that the skill levels generated in our experiments tend to increase with the ratio σ_W/σ_P.

This has relevance for the estimation of potential skill levels outside the basins with long streamflow measurement records. The CTRL simulation allows the estimation of σ_W over CONUS, and σ_P over CONUS can be estimated from precipitation datasets. The left panels in Figure 3 show the distribution of σ_W/σ_P for JFM (top) and AMJ (bottom); again, higher values of the ratio indicate a stronger potential for accurate streamflow prediction. The right panels show the corresponding skill levels achieved using the CTRL grid cell streamflows as "synthetic truth". The strong first-order agreement in the fields supports the idea that we have identified reasonable spatial distributions of higher skill potential.

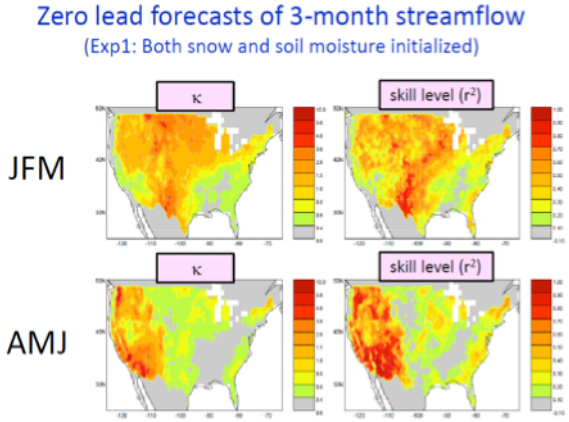

Figure 3: Top left: spatial field of σ_W/σ_P for JFM. Top right: spatial field of skill levels achieved in forecast experiments using a "synthetic truth": the grid cell runoffs generated in the CTRL simulation. Bottom panels: same, but for AMJ.

Publications:

Koster, R.D., S.P.P. Mahanama, B. Livneh, D. Lettenmaier, and R. Reichle, 2010: Skill in streamflow forecasts derived from large-scale estimates of soil moisture and snow. *Nature Geoscience*, doi:10.1038/NGEO944.

Mahanama, S.P.P., B. Livneh, R.D. Koster D. Lettenmaier, and R. Reichle, 2011: Soil moisture, snow, and seasonal streamflow predictability in the United States. *J. Hydromet. (submitted)*.

Improving the Consistency of Ocean Color Data: A Step toward Climate Data Records

Watson Gregg and Nancy Casey

The state of ocean biology, represented by chlorophyll and observed globally by ocean color sensors, is an important indicator of climate change. Although there have been several efforts to document changes in ocean chlorophyll observed by satellite, nearly all are limited to a single sensor (McClain et al., 2004; Gregg et al., 2005; Behrenfeld et al., 2006; Polovina et al., 2008). Observing climate change requires multiple, successive missions, since the operational lifetime of any sensor is finite (typically about 10 years). There are fewer efforts attempting to document changes across two missions (Gregg et al., 2002; 2003; Antoine et al., 2005; Kahru and Mitchell, 2008). This is a much greater challenge, because all of the ocean color missions flown to date (and also proposed) differ greatly in design, capability, and sampling. Yet it is this challenge that must be met if we are to successfully observe climate change using satellite sensors.

Previous efforts describing changes using two or more ocean color sensors have assumed that consistency in processing algorithms is sufficient to produce consistency in observations, and any deviations between the two observations are derived from natural variability. This assumption has not been tested, however, and it remains an assertion inherent in the methods.

Two ocean color missions, the Sea-viewing Wide Field-of-view Sensor (SeaWiFS) and the Moderate Resolution Imaging Spectroradiometer (MODIS) on the Aqua satellite overlap for the period 2003 through 2007. Both sensors are processed by NASA using the same pre- and post-launch calibration and algorithms. In a diagnostic comparison of the chlorophyll from these two sensors, Morel et al. (2007) found consistency over moderate to high ranges of the chlorophyll concentration spectrum, but deviations at the low end. We explore here how these differences translate into the representation of global and large scale regional biology, and in decadal trends. We substitute MODIS data for SeaWiFS when it became available in 2003 to test for the quality of temporal consistency, which is needed for satellite data to ensure unbiased interpretation of climate change.

We additionally investigate the ability of a new approach to satellite ocean color data, the Empirical Satellite-In situ Data (ESRID) algorithm (Gregg et al., 2009), to reduce the discrepancies between the two sensor data sets. Previously, ESRID was shown to improve the bias of SeaWiFS data and reduce the need for post-launch re-calibration. Here we apply the approach to two sensor data sets, SeaWiFS and MODIS, in an attempt to improve their consistency and promote their use as ocean biology Climate Data Records (CDRs).

Two ocean color missions, SeaWiFS and MODIS, overlap in time and are processed with consistent methods. Global annual median chlorophyll from SeaWiFS and MODIS differ by 12.2%. These discrepancies exceed the maximum observed interannual variability globally and in every major oceanographic basin. Estimates of trends are affected as well. For 1998-2007 the SeaWiFS global trend is -2.6% (not statistically significant). Substitution of MODIS for SeaWiFS in 2003-2007 produces a significant trend of -18%. A new approach that incorporates in situ data improves the consistency of the two sensor data sets. The global difference is -0.6% and the 10-year trend of SeaWiFS and MODIS agrees with standalone SeaWiFS (-3.3%, not significant). In oceanographic basins where sampling biases are small the differences are less than the maximum observed interannual variability. The approach improves the consistency of multiple successive ocean color missions and represents a step toward scientifically reliable Climate Data Records.

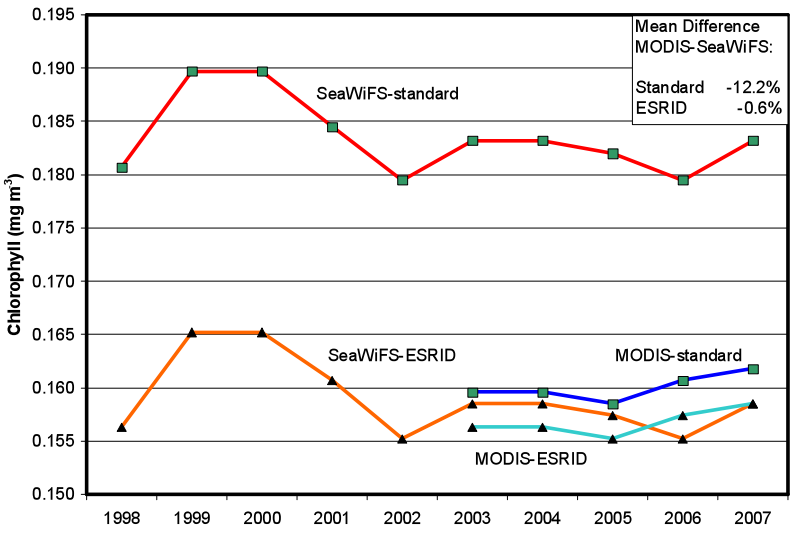

Figure 1: Global annual median chlorophyll for SeaWiFS and MODIS using the standard consistent processing method and ESRID. The mean difference between MODIS and SeaWiFS for 2003-2007 is shown.

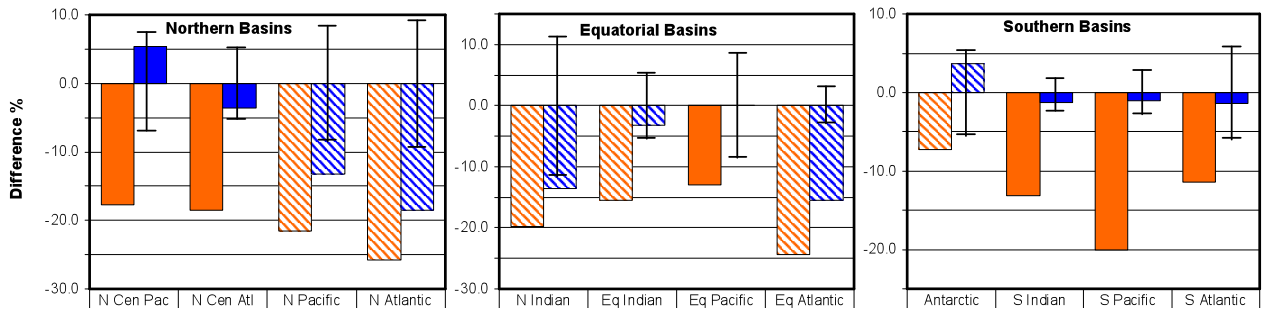

Figure 2: Mean of global annual median difference in chlorophyll between MODIS and SeaWiFS for the period 2003-2007. The "error" bars indicate the maximum interannual variability observed in the SeaWiFS record. Hatched bars indicate basins where >25% of the observations by one sensor were not observed by the other sensor for at least one month during 2003-2007, suggesting sampling bias.

URL: http://gmao.gsfc.nasa.gov/research/oceanbiology/

Publication:

Gregg, W.W. and N.W. Casey, 2010. Improving the consistency of ocean color data: A step toward climate data records. *Geophys. Res. Lett.*, **37**, L04605, doi:10.1029/2009GL041893.

Russian Heat Wave and Fires in the Summer of 2010: Application of the GEOS-5 Data Assimilation and Modeling System

Arlindo da Silva and Anton Darmenov

The extreme fire events that took place in Russia in the summer of 2010 presented a unique opportunity to test the capabilities of the GEOS-5 data assimilation and modeling system to simulate this and similar large scale fires. By evaluating the model performance against independent data sources such as aerosol optical thickness (AOT) retrieved from MODIS and MISR instruments, and visibility measured by WMO stations, we identified that the major discrepancies between the observed and modeled aerosol loadings can be explained by deficiencies in the used biomass burning emissions. Assimilation of AOT data helped reduce the modeled AOT bias and improved the PM2.5 surface concentrations.

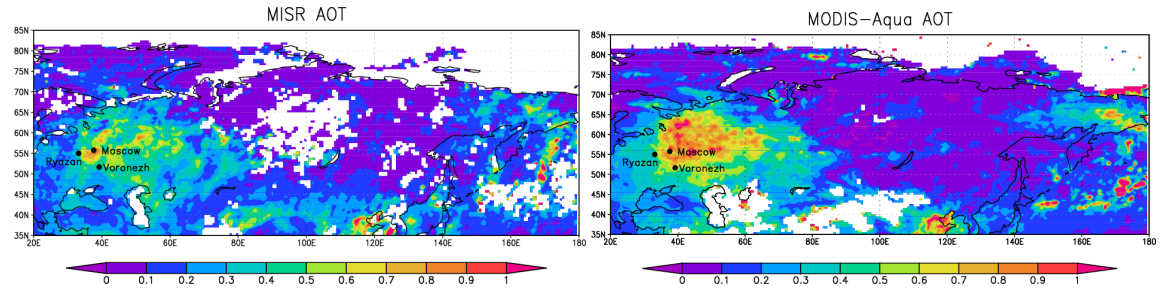

Figure 1: The Moscow and Far Eastern regions were among the affected by the fires as can be seen by the elevated AOT values observed over these regions. Shown are the time averaged (20 July – 20 August, 2010) AOT retrieved from MISR (left) and MODIS/AQUA (right).

We performed two modeling experiments designed to evaluate the performance of the coupled GEOS-5/GOCART and the GEOS-5 Aerosol Assimilation System (GAAS). The experiments were performed at 0.5° × 0.625° horizontal resolution as intermittent replay runs forced with the MERRA fields, thus ensuring realistic transport of the aerosol and chemical species. QFED v2.1 daily mean biomass burning emissions with prescribed diurnal cycle were used in the two model runs.

The densely populated Central Federal District (referred to as central region from now on) was in particular heavily affected by the smoke and pollution from the fires (Figure 1). The observed time-averaged AOT values for the period 20 July – 20 August 2010 in the Moscow area were about 0.7-0.8.

Modeled AOTs are shown in Figure 2. Comparing the results from the GEOS-5/GOCART run against the satellite retrievals, one can see that the model underestimated the aerosol loading by a factor of 2-3 in the central region. The main reason for the observed discrepancies can be explained by weak biomass burning emissions. Assimilation of bias-corrected neural net retrievals (NNR) of Aqua AOT data into the model had a positive impact and improved significantly the modeled AOT fields (Figure 2b) and helped decrease the negative impact of the weak fire emissions.

The modeled PM2.5 surface concentrations also benefited from the assimilation of AOT observations and suggested that the Moscow area was affected by unhealthy pollution levels over a period of several weeks (Figure 2c). An examination of the observed (WMO stations) visibility and the GAAS results showed that during episodes with high levels of pollution the model produced higher than the reported visibility (Figure 2d), which would suggest that the modeled PM2.5 concentrations were under-predicted.

The results presented here are encouraging with regards to the positive impact of the assimilation of aerosol data on the modeled aerosol fields. Despite the apparently week biomass burning emissions, the GAAS aerosol data assimilation system was able to produce realistic aerosol loadings at the surface and in the vertical column. The use of refined biomass burning emissions should further improve the agreement between the model and the observations and help establish GEOS-5 as a tool that is well suited to model and study fires and their effects on a regional and global scale.

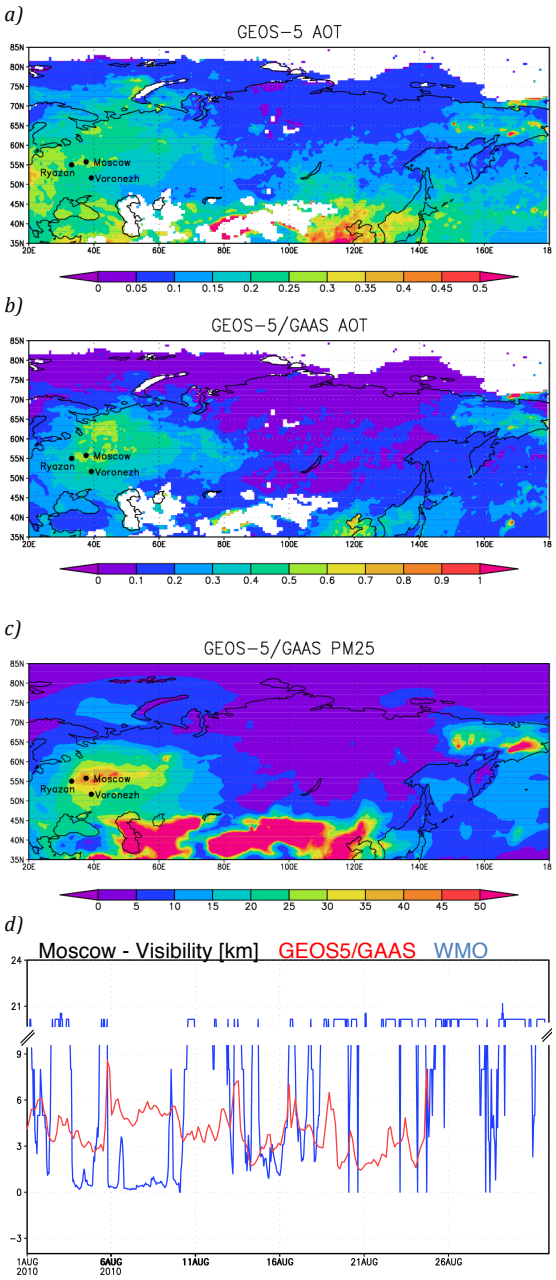

Figure 2: Time averaged (20 July – 20 August 2010) AOT from a) the GEOS-5/GOCART intermittent run and b) the GAAS 6-hour forecast sampled with the MODIS/Aqua retrievals. c) Map of time-averaged PM2.5 [μg m^{-3}] surface concentrations. d) Time series of observed (blue) and modeled (red) visibility in Moscow.

Emission and Transport of Carbon Monoxide from the 2010 Russian Fires

Lesley Ott, Sarah Strode, Anton Darmenov, Juying Warner (UMBC), Steven Pawson and Arlindo da Silva

During July and August of 2010, portions of central Russia and Siberia experienced elevated temperatures and severe drought conditions that facilitated the development of a number of large forest fires. During this period, air quality in Moscow was extremely poor with surface carbon monoxide (CO) concentrations reaching levels detrimental to human health. NASA remote sensing resources provided a wealth of observations of the fires and their impact on atmospheric composition. GMAO's operational GEOS-5 system combines near real-time estimates of biomass burning emissions with realistic atmospheric transport to simulate the impact of biomass burning events as they occur. This case provided a unique opportunity to evaluate the performance of the operational trace gas modeling system and to identify areas in need of improvement.

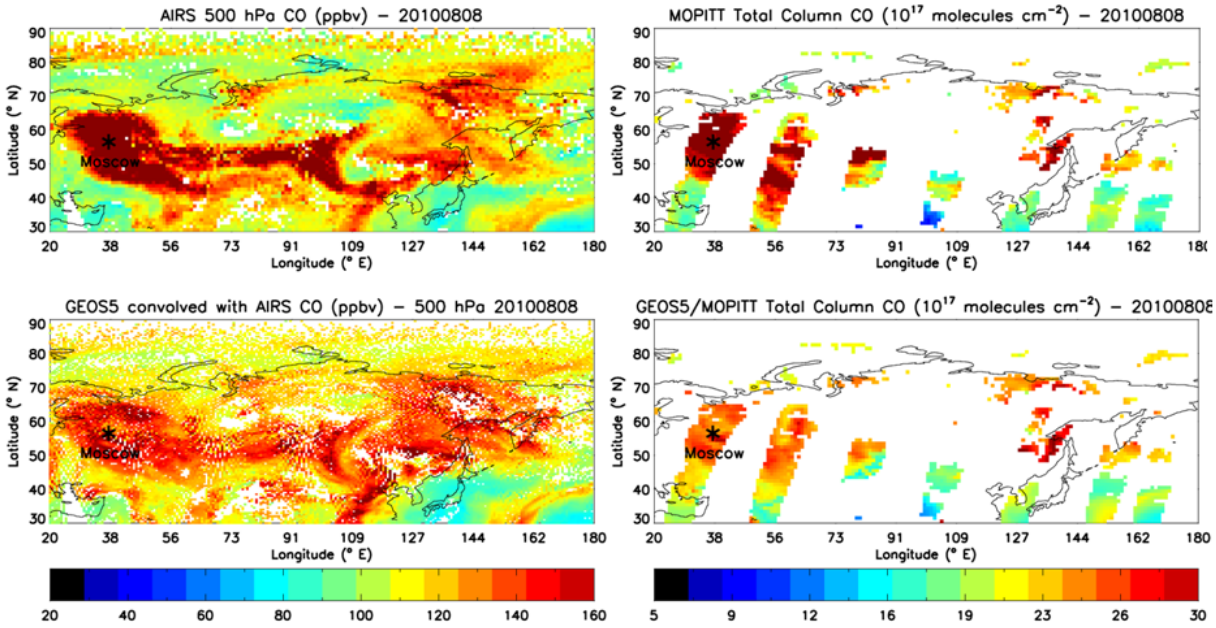

Figure 1: Observed distributions of atmospheric carbon monoxide from the AIRS (top left) and MOPITT (top right) on August 8. GEOS-5 simulated CO distributions are sampled using the averaging kernels of AIRS (bottom left) and MOPITT (bottom right) to estimate comparable quantities.

CO is an excellent tracer of pollution from fires and is observed by several satellite instruments that provide complementary information about atmospheric distributions. The Atmospheric Infrared Sounder (AIRS) provides nearly global daily coverage with peak sensitivity in the mid-troposphere. The Measurements Of Pollution In The Troposphere (MOPITT) instrument provides global coverage every 4-5 days, but provides greater sensitivity to lower levels of the atmosphere that are more strongly affected by recent emissions. Figure 1 shows observed CO from both satellites and simulated CO sampled using the appropriate satellite averaging kernel information. On August 8, both satellites show elevated CO in the Moscow region. GEOS-5 simulated CO shows an increase over typical background levels, but the simulated enhancement is considerably less than observed. Additionally, comparisons between the model and AIRS suggest that simulated background CO mixing ratios over Europe may be overestimated; this is evident in comparisons of days prior to the fire activity (not shown) and in latitudes north of the fire

plume on August 8. Though the magnitude of CO enhancement in the plume is underestimated, the model is able to reproduce the shape of biomass burning plumes observed by AIRS remarkably well.

CO over Moscow may be underestimated because the large contribution of CO from peat fires is not adequately captured by the Quick Fire Emissions Database, version 1 (QFED) used in the operational GEOS-5 system. QFEDv1 combines observations of fire hot spots from the Moderate Resolution Imaging Spectroradiometer (MODIS) with scaling factors derived to match global mean estimates of dry matter burned produced by the Global Fire Emissions Database, version 2 (GFEDv2, van der Werf et al., 2006). These estimates are then transformed into emissions of trace gases and aerosols using biome dependent emission factors. This methodology allows for the near real-time estimation of realistic biomass burning emissions but the system may be challenged by smoldering peat fires because they are more difficult to observe by satellite. Peat fires are particularly important in determining CO emissions because they tend to emit much larger quantities of CO than other types of fires but peat specific emissions factors are not included in GFEDv2 or QFED. To examine the impact of peat burning, we created a new version of emissions that combines information from an updated version of QFED (QFEDv2) with estimates of peat emissions created using estimates of fractional peat coverage in Russia and peat specific emissions factors.

Figure 2 shows the time series of MOPITT column CO abundances during the peak fire period along with results of several GEOS-5 simulations with the bias in simulated background CO removed. The operational GEOS-5 system using QFEDv1 significantly underestimates CO produced by the fires. The revised emissions that include peat burning are more successful in capturing the CO enhancement over Moscow, but continue to underestimate the magnitude of enhancement. In order to understand the magnitude of adjustment in emissions needed to match MOPITT observations, we conducted an experiment that used a number of CO tracers representing emissions from different 5-day period during July and August. Averages of these tracers over the Moscow regions were combined with a linear regression to determine 5-day scaling factors that further improve the comparison with observations. Research is ongoing to understand the underlying physical processes that govern peat emissions and to improve the representation of these processes in future versions of GEOS-5. The refined emissions estimates are currently being used to better understand transport of biomass burning pollution and the impact of boreal biomass burning on atmospheric composition at both local and global scales.

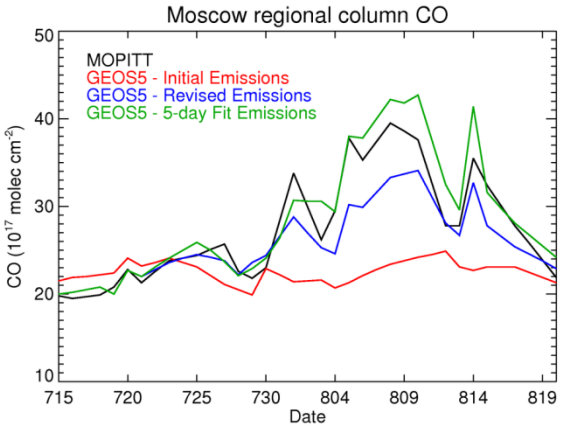

Figure 2: Time series of MOPITT observed column CO (black) averaged over the Moscow region. The GEOS-5 operational system using QFEDv1 (red) significantly underestimates CO produced by Russian fires. A revised emissions inventory including peat burning (blue) performs better, though the peak fire emissions are still underestimated. Tracers of 5-day fire emissions fit with a linear regression to MOPITT provide adjustment factors that further improve the comparison with observations (green).

Reference:

van der Werf, G.R., J.T. Randerson, L. Giglio, G.J. Collatz, P.S. Kasibhatla, and A.F. Arellano Jr., 2006: Interannual variability in global biomass burning emissions from 1997 to 2004. *Atmos. Chem. Phys.*, **6**, 3423-3441, doi:10.5194/acp-6-3423-2006.

Emission and Transport of Cesium-137 from Biomass Burning in the Summer of 2010

Sarah Strode, Lesley Ott, Steven Pawson and Ted Bowyer (PNNL)

Cesium-137 (^{137}Cs) is an anthropogenic radionuclide with a half-life of 30 years, deposited throughout the northern hemisphere by nuclear weapons testing. The Chernobyl accident provided an additional source to the environment in 1986, especially in Europe. Following the nuclear testing era, atmospheric concentrations of ^{137}Cs have decreased to low levels. However, resuspension of ^{137}Cs on dust or during biomass burning can elevate atmospheric concentrations and transport ^{137}Cs away from the source region.

The summer of 2010 was a season of intense biomass burning in western Russia, with high levels of air pollutants from wildfires reaching Moscow. Since ^{137}Cs binds to aerosols in the atmosphere, we examine the relationship between ^{137}Cs observations from the International Monitoring System (IMS) built by the Comprehensive Nuclear-Test-Ban Treaty Organization (CTBTO) and aerosol optical depth (AOD) from the MODIS satellite during this period.

We simulate aerosol distributions in July and August of 2010 using the Goddard Chemistry, Aerosol, Radiation and Transport (GOCART) model online within the Goddard Earth Observing System (GEOS-5) atmospheric general circulation model constrained by meteorology from the Modern-Era Retrospective Analysis for Research Applications (MERRA). The transport of ^{137}Cs on aerosols is then modeled by multiplying the ^{137}Cs to organic carbon emission ratio to the modeled organic carbon. Tracers tagged according to their region of origin provide additional information on the sources of ^{137}Cs measured at a particular station.

The IMS station located in Dubna, Russian Federation, shows increased levels of ^{137}Cs during the peak biomass-burning period in western Russia, concurrent with high levels of AOD (Figure 1). The relationship between increased AOD and ^{137}Cs detections is also evident at an IMS station in Yellowknife, Canada, which is also influenced by biomass burning.

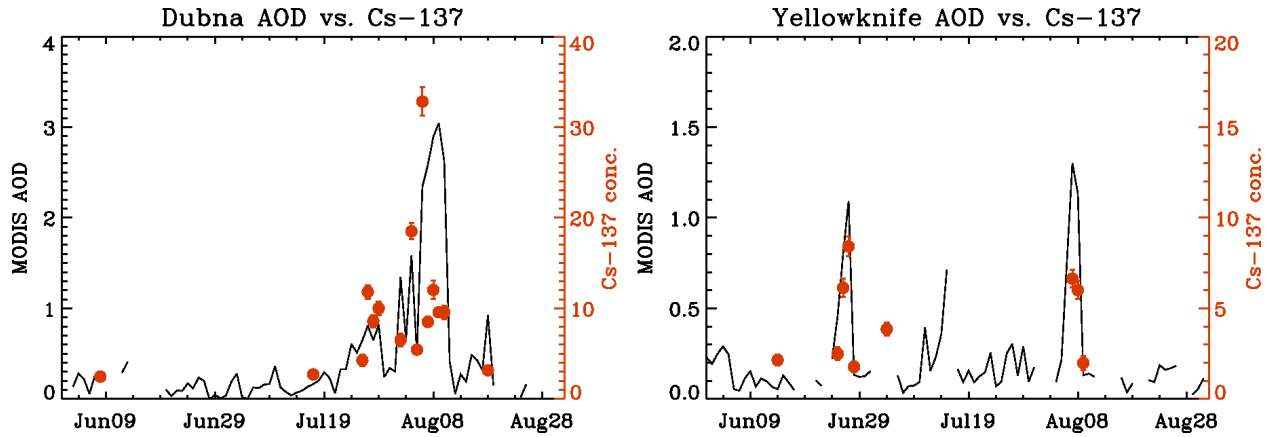

Figure 1: Comparison of MODIS AOD (black line, left axis) and ^{137}Cs concentrations (red dots, right axis) at the Dubna (left) and Yellowknife (right) IMS stations.

Figure 2 shows the modeled ^{137}Cs compared to observations. The model results assume a ^{137}Cs to organic carbon ratio of 0.18 kBq kg^{-1} to minimize the model bias compared to the observed values at Dubna. The model tracer for the Russian biomass burning is the primary contributor to the total tracer at Dubna, and has a correlation of r^2=0.64 with the detected ^{137}Cs concentrations. A higher correlation with the

observations, r^2=0.73, is found for the model tracer emitted in the region southeast of Moscow. At Yellowknife, the total tracer is dominated by the North American biomass burning emissions. The model shows peaks corresponding to the days with detections at Yellowknife, although the magnitude of the peaks is underestimated.

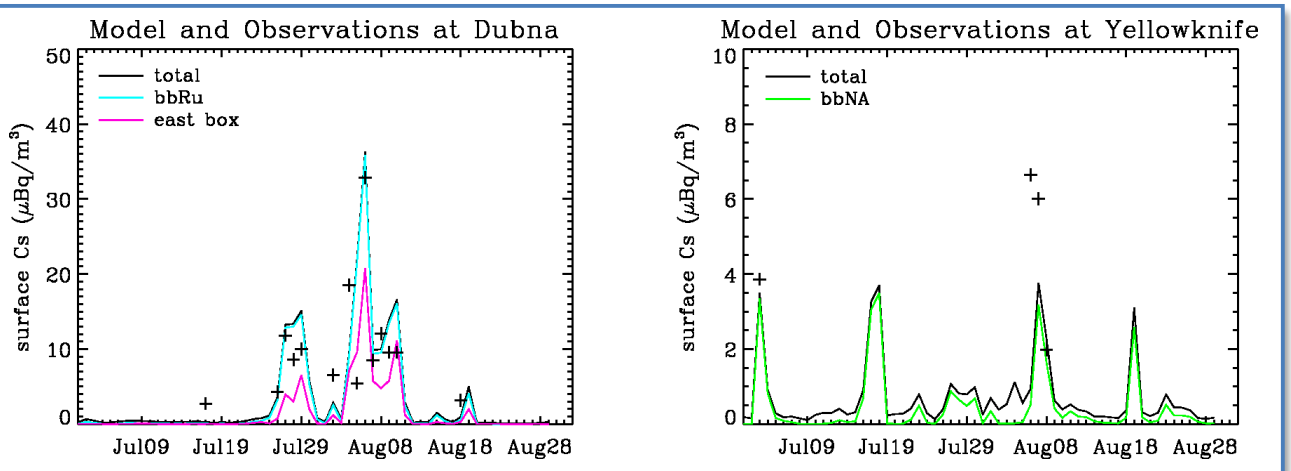

Figure 2: Observations of ^{137}Cs (+) compared to the simulated ^{137}Cs total tracer (black lines), Russian biomass burning tracer (blue line), tracer for the region southeast of Moscow (pink line), and North American biomass burning tracer (green line) at Dubna (left) and Yellowknife (right).

Our best-guess emissions suggest that $1.0*10^{12}$ Bq of ^{137}Cs were released by biomass burning north of 40° during July and Aug. of 2010. Based on burned area from the Global Fire Emissions Database (GFED3) burned area data set (Giglio et al., 2010), we estimate ^{137}Cs emissions of $1.7*10^5$ and $1.6*10^5$ Bq/ha for Russian and Canadian biomass burning, respectively. These values are consistent with the estimate of $2*10^5$ Bq/ha by Wotawa et al. (2006) for biomass burning in 2003 and 2004. The simulated values of ^{137}Cs deposition are small compared to existing surface concentrations, but suggest that biomass burning results in a small northward redistribution of ^{137}Cs.

References:

Giglio, L., J.T. Randerson, G.R. van derWerf, P.S. Kasibhatla, G.J. Collatz, D.C. Morton, and R.S. DeFries, 2010: Assessing variability and long-term trends in burned area by merging multiple satellite fire products. *Biogeosciences*, **7**(3), 1171–1186.

Wotawa, G., L.-E. De Geer, A. Becker, R. D'Amours, M. Jean, R. Servranckx, and K. Ungar, 2006: Inter- and intra-continental transport of radioactive cesium released by boreal forest fires. *Geophys. Res. Lett.*, **33**, L12806. doi:10.1029/2006GL026206.

Development Of Sub-Seasonal Ensemble Forecast Techniques

Yoo-Geun Ham, Siegfried Schubert and Yehui Chang

Using Empirical Singular Vectors (ESVs) we have developed a new ensemble generation strategy tailored to the sub-seasonal forecast range. This method, based on Singular Vectors, uses an empirical linear operator determined by a linear inverse modeling approach instead of a dynamical operator.

In this study, ESVs are calculated from the hindcast output of the GEOS-5 coupled atmosphere-ocean model (AOGCM) for boreal winter season predictions from 1990 to 1999. With a focus on the Madden-Julian Oscillation (MJO), it was found that the optimal time lag for estimating the operator (lag time between initial and final time) is 10 days. The ESV is calculated with respect to the MJO phases (i.e. 8 ESVs are obtained for each MJO phase). The anomalies for sub-seasonal variability are generated by subtracting the climatology and by removal of the previous 120-day mean. To reduce the dimensions of the empirical operator, a Combined EOF analysis is used based on the latitudinally-averaged (15°S-15°N) 850 hPa zonal wind, 200 hPa zonal wind, and 200 hPa velocity potential. The 5 (2) leading principal components (PCs) are used as the initial (final) variables. The ESVs are added and subtracted to the initial conditions (computed from a replay of MERRA data), to produce a 2-member ensemble of predictions for each of the winter seasons from 1990 to 1999. The forecast skill of the ESV-based ensemble predictions is compared to a simple ensemble generation method called the Lagged Averaged Forecast (LAF) method. In the following, the ensemble forecasts with ESV and LAF are called 'ESV predictions', and 'CNTL predictions', respectively.

Figure 1 shows the spatial pattern of the initial ESV at MJO phase 4. In the case of the lower and upper level winds, there are robust anomalies over the Indian Ocean where the MJO is initiated. In addition, positive low-level wind anomalies occur over the maritime continent and far eastern Pacific. The opposite phases of the upper and lower level winds are a clear indication of a baroclinic structure. The circulation anomalies are dynamically linked to the hydrological fields. Over the far western Indian Ocean, a positive moisture anomaly coincides with low-level convergence. Consistently, there is a positive temperature anomaly over the Africa possibly generated by zonal warm-air advection due to easterly wind perturbations.

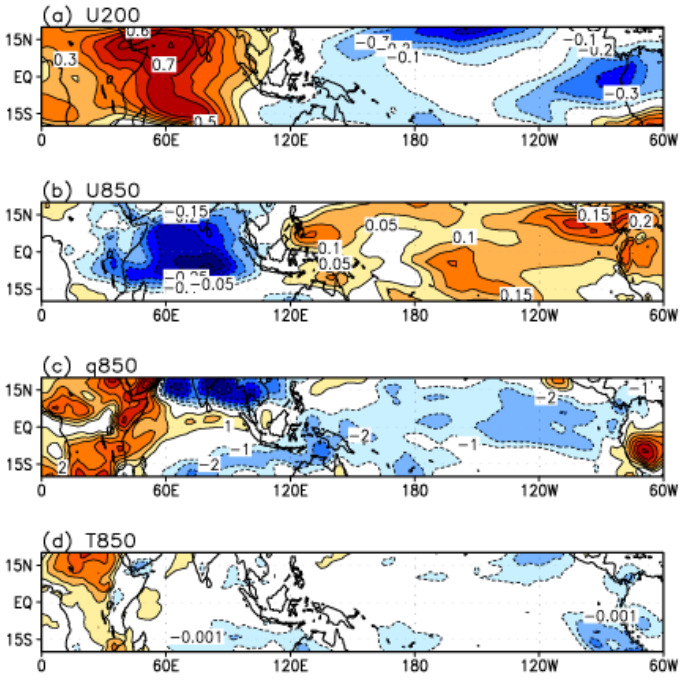

Figure 1: Spatial pattern of initial (a) zonal wind at 200 hPa, (b) zonal wind at 850 hPa, (c) specific humidity at 850 hPa, and (d) air-temperature at 850 hPa from the ESV at MJO phase 4.

igure 1: Spatial pattern of initial (a) zonal wind at 200 hPa, (b) zonal wind at 850 hPa, (c) specific humidity at 850 hPa, and (d) air-temperature at 850 hPa from the ESV at MJO phase 4.

Figure 2 shows the correlation skill of the bi-variate Wheeler-Hendon Real-time Multivariate MJO (RMM) index in CNTL and ESV predictions. The difference of correlation skill between ESV and CNTL is also shown. It is clear that there is robust improvement in the ESV-based predictions, particularly at MJO phases 4-8. For example, the correlation skill improvement at MJO phase 4 is more than 0.2 between 21 and 25 forecast lead days. It is interesting that this improvement is robust for the cases where the correlation skill of CNTL is relatively low. This suggests that the improvement using optimal perturbations is most robust when the forecast target is least predictable.

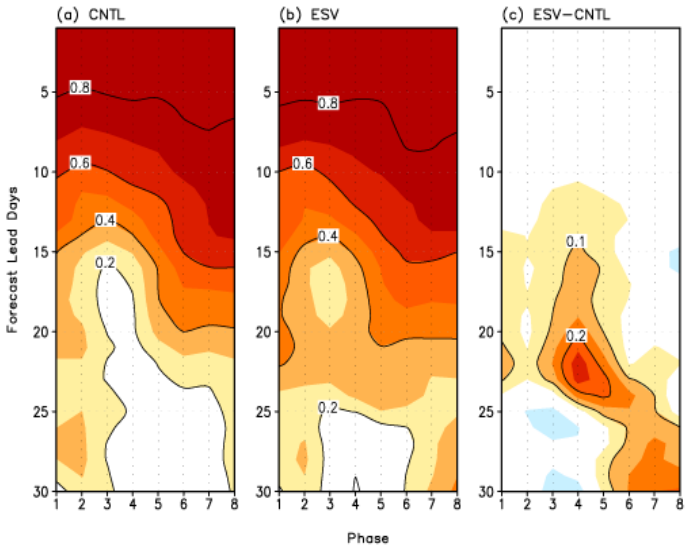

Figure 2: Correlation skill of the bi-variate RMM index in the (a) CNTL and (b) ESV predictions for each MJO phase. The difference in correlation skill between the ESV and CNTL predictions is shown in panel (c).

GEOS-5 Products and Near Real-Time Production Operations

Gi-Kong Kim

Over this period, the GMAO continued the near real-time (NRT) production of the GEOS-5 data assimilation products and forecasts as well as the MERRA products. More details of products are provided at http://gmao.gsfc.nasa.gov/products/. A major upgrade of the NRT GEOS-5 production system, from the current v5.2.0 to v5.7.2, is planned for August 2011.

NRT Products for Operational Users such as EOS Instrument Teams. The GEOS-5 NRT production, which started in January 2007, has gone through several system upgrades. The current system, GEOS-5.2.0, uses 128 processors on an IBM Linux cluster machine in the NASA Center for Climate Simulation (NCCS). It generates assimilation products at ½° horizontal resolution 4 times a day and 5-day forecasts twice a day. Each analysis assimilates about 2 million observations, of which just over 1/3 are AIRS radiance data. Each assimilation cycle generates 169 unique variables. Ten products totaling about 4 GB are sent to Goddard Earth Sciences Data and Information Services Center (GES DISC) (http://disc.sci.gsfc.nasa.gov/) daily for distribution to the operational users. The primary operational users are the EOS instrument teams such as MLS, TES, and MODIS; other NASA and international projects such as CALIPSO, SRB, FlashFLUX, POWER, GLDAS, Flood Warning, and JAXA/SMILES; and research teams at universities and government organizations. The GEOS-5.2.0 system was ported to a new HPC platform in July 2010 to take advantage of the new capabilities. As the new data types and new capabilities are introduced to the GEOS-5 data assimilation, increased computing power is required to keep the real time operations above the minimum performance threshold.

A Major System Upgrade under Way. Many improvements made in the atmospheric data assimilation quickly converged in a succession of GEOS-5 development systems in 2010. The latest version, GEOS-5.7.2, is the candidate system for the GEOS-5 system upgrade and is now running in parallel with the GEOS-5.2.0 NRT system. The system upgrade is scheduled to be completed in August 2011. The new system includes many advances made in the GCM, physics, and GSI. There are also significant structural differences in the GEOS-5.7.2 products.

Salient features of GEOS-5.7.2 products are:
- The horizontal spatial resolution is increased from ½° to ¼°
- File format is changed from HDF-4 to netCDF-4/HDF-5
- Temporal frequency of 3-D products is changed from 6 hourly to 3 hourly
- Temporal frequency of most 2-D products is changed from 3 hourly to 1 hourly
- New variables, such as ocean and aerosols fields, have been added

The new system is capable of assimilating new data types such as AMSR-E, IASI, MHS, and HIRS4. The production run will use 720 processors on the IBM HPC system in the NCCS. This represents about a 6-fold increase in the job size.

MERRA Products: 30+Year Reanalysis. Three separate streams of MERRA data production using GEOS-5.2.0 started in February 2008. Each stream generated about 1 month of MERRA data per week on average. The two streams for the earlier periods were stopped in early 2010 when the production completed the 32-year period from 1979 through 2010. The most recent stream caught up to real-time in April 2010 and continues to generate the analysis data with an intentional lag time of about 3 weeks behind real time, ensuring that the best observations are acquired and used for the analysis. The MERRA data have been available for public access since December 2008 via an online data distribution system

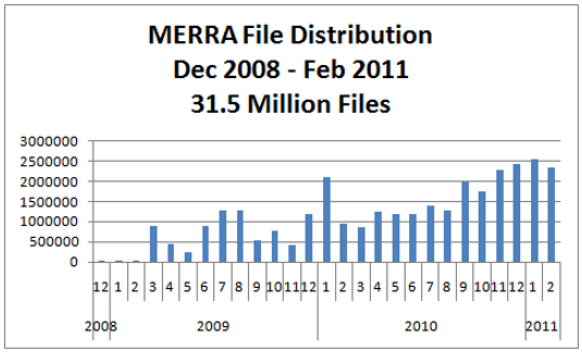

Figure 1: Monthly MERRA file distribution in number of files accessed by users

(http://disc.sci.gsfc.nasa.gov/mdisc/) at GES DISC. Users from all over the globe access the MERRA data at a still increasing pace. A little over 31 million files with a total volume of 530 TB (Figure 1) have been downloaded as of February 2011. We retrospectively generated ocean fields by 'replaying' the GEOS-5 model with the MERRA data. These ocean products will be shipped to MDISC as new additions to the MERRA product suite. Scientific or technical questions about MERRA products are received at a steady pace and fielded by a small user support team. A FAQ web page was built based on communications with users and is regularly updated and expanded. This provides very useful scientific as well technical information on the MERRA data.

G5.4.1-CERES products. GMAO continued to provide the NASA CERES team with GEOS-5.2.0 products that are generated using a reduced set of observations covering 1997 – present. Use of new input observations for this dataset is carefully controlled to minimize potential data shock when a new data type is introduced in mid-stream. In December 2010, we started a new GEOS-5.4.1 data production for the CERES team. The production is performed in two separate streams, one for 1997 – 2000 and another for 2000 – 2012. The GEOS-5.4.1 products are in HDF-4 format and are generated at 1/2° horizontal resolution.

Mission support in 2010-2011. GMAO provided real time support to Global Hawk Pacific Mission (GloPac) in April 2010 and the Genesis and Rapid Intensification Processes (GRIP) mission from August through September 2010. Five-day forecasts were provided not only with meteorological fields, but also chemistry and aerosol products from the latest GEOS-5 system. The data were made available to the mission team on a data portal at the NCCS. The forecast and assimilation products were at ¼° horizontal resolution. An interactive visualization tool available on GMAO experimental forecast page (http://gmao.gsfc.nasa.gov/forecasts/) is customized to meet specific requirements of a particular mission. The GEOS-5 analyses and forecasts, with aerosols and tagged tracers from regions of biomass burning, also supported Phase IV (May 2011) of the HIAPER Pole-to-Pole Observations (HIPPO) of Carbon Cycle and Greenhouse Gases Study.

Publications

Allen, D.A., A.R. Douglass, G.L. Manney, S.E. Strahan, J. Krosschell, J.V. Trueblood, **J.E. Nielsen, S. Pawson, Z. Zhu**, 2011: Modeling the Frozen-In Anticyclone in the 2005 Summer Stratosphere. *Atmos. Chem. Phys.,* **11**, 4557-4576. doi:10.5194/acp-11-4557-2011.

Austin, J., and Coauthors, 2010: Chemistry-climate model simulations of the Antarctic ozone hole. *J. Geophys. Res.*, **115**, D00M11. doi:10.1029/2009JD013577.

Austin, J., and Coauthors, 2010: The decline and recovery of total column ozone using a multi-model time-series analysis. *J. Geophys. Res.*, **115**, D00M10. doi:10.1029/2010JD013857.

Butchart, N., and Coauthors, 2010: Quantifying uncertainty in projections of stratospheric ozone over the 21st century. *Atmos. Chem. Phys.*, **10**, 9473-9486. doi:10.5194/acp-10-9473-2010.

Bosilovich, M.G., F. Robertson and **J. Chen**, 2011: Global energy and water budgets in MERRA. *J. Climate (accepted).*

Brunke, M.A., Z. Wang, X. Zeng, **M. Bosilovich**, C.-L. Shie, 2011: An assessment of the uncertainties in ocean surface turbulent fluxes in 11 reanalysis, satellite-derived, and combined global data sets. *J. Climate (in press).*

Chang, Y., **S. Schubert**, and **M. Suarez**, 2011: Attribution of the extreme U.S. East Coast snowstorm activity of 2010. *J. Climate (in press).*

Cullather, R.I., and **M. Bosilovich**, 2011: The moisture budget of the polar atmosphere in MERRA. *J. Climate*, **24**, 2861-2879. doi:10.1175/2010JCLI4090.1.

Cullather, R.I., and **M. Bosilovich**, 2011: The energy budget of the Polar atmosphere in MERRA. *J. Climate (in press).*

Daescu D.N. and **R. Todling**, 2010: Adjoint sensitivity of the model forecast to data asimilation systemerror covariance parameters. *Q. J. R. Meteorol. Soc.,* **136**, 2000–2012. doi:10.1002/qj.693.

Decker, M., M. Brunke, Z. Wang, K. Sakaguchi, X. Zeng, and **M. Bosilovich**, 2011: Evaluation of the reanalysis products from GSFC, NCEP and ECMWF using flux tower observations. *J. Climate (conditionally accepted).*

De Lannoy, G.J.M., **R.H. Reichle**, K.R. Arsenault, P.R. Houser, S.V. Kumar, N.E.C. Verhoest, and V.R.N. Pauwels, 2011: Multi-scale assimilation of AMSR-E snow water equivalent and MODIS snow cover fraction in northern Colorado. *Water Resources Res. (submitted).*

De Lannoy, G.J.M., **R. Reichle**, P. Houser, K. Arsenault, N. Verhoest, V. Pauwels, 2010: Satellite-scale snow water equivalent assimilation into a high-resolution land surface model. *J. Hydromet.*, **11**, 352-369. doi:10.1175/2009JHM1192.1.

Entekhabi, D., E. Njoku, P. O'Neill, K. Kellog, W. Crow, W. Edelsteing, J. Entin, S. Goodman, T. Jackson, J. Johnson, J. Kimball, J. Piepmeier, R. Koster, K. McDonald, M. Moghaddam, S. Moran, **R. Reichle,** el al., 2010: The soil moisture active and passive (SMAP) mission. *Proc. IEEE*, **98**, 704-716. doi:10.1109/JPROC.2010.2043918.

Entekhabi, D., **R. Reichle**, **R. Koster,** and W. Crow, 2010: Performance metrics for soil moisture retrievals and application requirements. *J. Hydromet.*, **11**, 832-840. doi:10.1175/2010JHM1223.1.

Eyring, V., and Coauthors, 2010: Multi-model assessment of ozone return dates and ozone recovery in CCMVal-2 models. *Atmos. Chem. Phys.*, **10**, 9451-9472. doi:10.5194/acp-10-9451-2010.

Eyring, V., I. Cionni, J.F. Lamarque, H. Akiyoshi, G.E. Bodeker, A.J. Charlton-Perez, S.M. Frith, A. Gettelman, D.E. Kinnison, T. Nakamura, L.D. Oman, **S. Pawson**, Y. Yamashita, 2010: Sensitivity of 21st century stratospheric ozone to greenhouse gas scenarios. *Geophys. Res. Lett.*, **37**, L16807.

doi:10.1029/2010GL044443.

Forman, B.A., **R.H. Reichle**, and M. Rodell, 2011: Assimilation of terrestrial water storage from GRACE in a snow-dominated basin. *Water Resources Res. (submitted).*

Forman, B., and S. Margulis, 2011: Impact of covariance localization on ensemble estimation of surface downwelling longwave and shortwave radiation fluxes. *J. Hydrometeorol. (submitted).*

Frith, R., and Coauthors, 2010: Chemistry-climate model simulations of 21st century stratospheric climate and circulation changes. *J. Climate*, **23**, 5349-5374. doi:10.1175/2010JCLI3404.1.

Gelaro, R., R.H. Langland, S. Pellerin, and **R. Todling**, 2010: The THORPEX observation impact inter-comparison experiment. *Mon. Wea. Rev.*, **138**, 4009-4025. doi:10.1175/2010MWR3393.1.

Gerber, E.P., M.P. Baldwin, H. Akiyoshi, J. Austin, S. Bekki, P. Braesicke, N. Butchart, M.P. Chipperfield, M. Dameris, S.S. Dhomse, S. Frith, R.R. Garcia, H. Garny, A. Gettelman, S.C. Hardiman, O. Morgenstern, **J.E. Nielsen**, **S. Pawson**, et al., 2010: Stratosphere-troposphere coupling and annular mode variability in chemistry-climate models. *J. Geophys. Res.*, **115**, D00M06. doi:10.1029/2009JD013770.

Gettelman, A., M.I. Hegglin, S-W. Son, J. Kim, M. Fujiwara, T. Birner, S. Kremser, M. Rex, J.A. Anel, J. Austin, J.F. Lamarque, H. Akiyoshi, D. Plummer, T.G. Shepard, J. Scinocca, M. Michou, H. Teyssedre, M. Dameris, H. Garny, C. Brühl, P. Jockel, **S. Pawson**, 2010: Multi-model assessment of the upper troposphere and lower stratosphere: tropics and trends. *J. Geophys. Res.*, **115**, D00M08, doi:10.1029/2009JD013638.

Gregg, W., and N. Casey, 2010: Improving the consistency of ocean color data: A step toward climate data records. *Geophys. Res. Letters*, **37**, 1-5. doi:10.1029/2009GL041893.

Gregg, W., N. Casey, 2011: Global ocean carbon estimates in a model forced by MERRA. *J. Climate (submitted).*

Ham,Y-G., I-S. Kang, J-S. Kug, 2011: Coupled bred vectors in the tropical pacific and their application to ENSO prediction. *Prog. Oceanogr. (submitted).*

Ham, Y-G, S. Schubert, and Y. Chang, 2011: Optimal initial perturbations for ensemble prediction of the Madden-Julian oscillation during Boreal winter. *J. Climate (submitted).*

Ham, Y.-G., I.-S. Kang, 2010: Growing-error correction of ensemble Kalman filter using empirical singular vectors. *Q. J. Roy. Meteorol. Soc.*, **136**, 2051-2060. doi:10.1002/qj.711.

Hardiman, S., N. Butchart, A. Charlton-Perez, T. Shaw, H. Akiyoshi, A. Baumgaertner, S. Bekki, P. Braesicke, M. Chipperfield, M. Dameris, R. R. Garcia, M. Michou, **S**. **Pawson**, E. Rozanov, and K. Shibata, 2011: Improved predictability of the troposphere using stratospheric final warmings. *J. Geophys. Res.* doi:10.1029/2011JD015914 *(in press).*

Hardiman, S., N. Butchart, A. Charlton-Perez, T. Shaw, H. Akiyoshi, A. Baumgaertner, S. Bekki, P. Braesicke, M.Cipperfield, M. Dameris, R.R. Garcia, M. Michou, **S. Pawson**, E. Rozanov, K. Shibata, 2011: Improved Predictability of the NAO using Stratospheric Final Warmings. *J. Geophys. Res. (submitted).*

Hegglin, M. I., and Coauthors, 2010: Multimodel assessment of the upper troposphere and lower stratosphere: Extratropics. *J. Geophys. Res.,* **115**, doi:10.1029/2010JD013884.

Holmes, T. R. H., T. Jackson, **R. Reichle**, and J. Basara, 2011: An assessment of surface soil temperature products from numerical weather prediction models using ground-based measurements. *Water Resources Res. (submitted).*

Jiang, J.H., H. Su, **S. Pawson**, H.-C. Liu, W. Read, J.W. Waters, M. Santee, D.L. We, M. Schwarz, A. Lambert, R. Fuller, J. Lee, N. Livesey, 2010: Five-year climatology (2003-2009) of upper tropospheric

water vapor and cloud ice from MLS and comparisons with GEOS-5 analyses. *J. Geophys. Res.*, **115**, D15103. doi:10.1029/2009JD013256.

Jiang, J., Su, H., **S. Pawson**, H.-C. Liu, W.G. Read, J. Waters, M.L. Santee, D.L. Wu, M.J. Schwartz, N.J. Livesey, A. Lambert, R.A. Fuller, J.N. Lee, 2010: Five year (2004–2009) observations of upper tropospheric water vapor and cloud ice from MLS and comparisons with GEOS-5 analyses. *J. Geophys. Res.*, **115**, D15103. doi:10.1029/2009JD013256.

Jimenez, C., C. Prigent, B. Mueller, S.I. Seneviratne, M.F. McCabe, E.F. Wood, W.B. Rossow, G. Balsamo, A.K. Betts, P.A. Dirmeyer, J.B. Fisher, M. Jung, M. Kanamitsu, **R.H. Reichle**, et al., 2011: Global inter-comparison of 12 land surface heat flux estimates. *J. Geophys. Res.*, **116**, D02102. doi:10.1029/2010JD014545.

Koster, R.D., S. Mahanama, B. Liveneh, D.P. Lettenmaier, R. Reichle, 2010: Skill of streamflow forecasts derived from large-scale estimates of soil moisture and snow. *Nature - Geoscience*, **3**, 613-616. doi: 10.1038/NGEO944.

Koster, R.D., S. Mahanama, T.J. Yamada, G. Balsamo, M. Boisserie, P. Dirmeyer, F. Doblas-Reyes, C.T. Gordon, Z. Guo, J.-H. Jeong, D. Lawrence, Z. Li, L. Luo, et al., 2010: The contribution of land surface initialization to subseasonal forecast skill: first results from the GLACE-2 project. *Geophy. Res. Letters*, **37**, L02402. doi:10.1029/2009GL04167.

Koster, R. D., and 21 co-authors, 2011: The second phase of the global land-atmosphere coupling experiment: Soil moisture contributions to subseasonal forecast skill. *J. Hydromet.* (*in press*). doi: 10.1175/2011JHM1365.1.

Kug, J-S., **Y-G. Ham,** E-J. Lee, I-S. Kang, 2011: Empirical Singular Vector (ESV) method for Ensemble ENSO prediction with a coupled GCM. *J. Geophys. Res. (submitted).*

Kumar, S.V., **R.H. Reichle**, K.W. Harrison, C.D. Peters-Lidard, S. Yatheendradas, and J.A. Santanello, 2011: Model parameter estimation for a priori bias correction in land data assimilation: A soil moisture case study. *Water Resources Res. (submitted).*

Lee, M.-I., **S.D. Schubert**, and D. Kim, 2011: Representation of tropical storms in the Northwestern Pacific by the Modern-Era Retrospective Analysis for Research and Applications. *Asia-Pacific J. Atmos. Sci.*, **47**, 245-253. doi: 10.1007/s13143-011-0013-z.

Lee, M-I., I. Choi W-K. Tao, **S.D. Schubert**, and I-S. Kang, 2010: Mechanisms of diurnal precipitation over the US Great Plains: A cloud resolving model perspective. *Clim. Dyn.* **34**, 419–437. doi: 10.1007/s00382-009-0531-x.

Lee, T. F., and Coauthors, 2010: NPOESS: Next-generation operational global earth observations. *Bull. Amer. Meteor. Soc*., **91**, 727–740. doi:10.1175/2009BAMS2953.1.

Li, F., R.S. Stolarski**, S. Pawson**, P.A. Newman, and D. Waugh, 2010: Narrowing of the upwelling branch of the Brewer.Dobson circulation and Hadley cell in chemistry-climate model simulations of the 21st century. *Geophys. Res. Lett.*, **37**, L13702. doi:10.1029/2010GL043718.

Liang, Q., J.M. Rodriguez, A.R. Douglass, J.H. Crawford, E. Apel, H. Bian, D.R. Blake, W. Brune, M. Chin, P.R. Colarco, **A. da Silva**, G.S. Diskin, B.N. Duncan, L.G. Huey, D.J. Knapp, D.D. Montzka, **J.E. Nielsen**, J.R. Olson, **S. Pawson**, A.J. Weinheimer, 2011: Reactive Nitrogen, Ozone and Ozone Production in the Arctic Troposphere and the Impact of Stratosphere-Troposphere Exchange. *Atmos. Chem. Phys*. *(submitted).*

Liu, Q., **R. Reichle**, R. Bindlish, M. Cosh, W. Crow, R. de Jeu, **G. De Lannoy**, G. Huffman, T. Jackson, 2010: The contributions of precipitation and soil moisture observations to the skill of soil moisture estimates in a land data assimilation system. *J. Hydromet. (in press).*

Lim, Y.-K., L. Stefanova, S. Chan, **S.D. Schubert**, J.J. O'Brien, 2011: High-resolution subtropical

summer precipitation derived from dynamical downscaling of the NCEP/DOE reanalysis: How much small-scale information is added by a regional model?, *Clim. Dyn.* doi:10.1007/s00382-010-0891-2 *(in press)*.

Lim, Y.-K., and **S.D. Schubert**, 2011: The Impact of ENSO and the Arctic Oscillation on winter temperature extremes in the Southeast United States. *Geophys. Res. Lett. (submitted)*.

Maggioni, V., **R.H. Reichle**, E.N. Anagnostou, 2011: The effect of satellite-rainfall error modeling on soil moisture prediction uncertainty. *J. Hydromet.*, **12**, 413-428. doi:10.1175/2011JHM1355.1.

McCarty, W., R. Errico, and **R. Gelaro**, 2011: Cloud coverage in the joint OSSE nature run. *Mon. Wea. Rev. (conditionally accepted)*.

Mahanama, S.P.P., B. Livneh, **R.D. Koster**, D. Lettenmaier, and **R.H. Reichle**, 2011: Soil moisture, snow, and seasonal streamflow forecasts in the United States. *J. Hydromet. (submitted)*.

Menon, S., H. Akbari, **S. Mahanama**, I. Sednev, and R. Levinson, 2010: Radiative forcing and temperature response to changes in urban albedos and associated CO_2 offsets. *Env. Res. Letters*, **5**, 014005. doi:10.1088/1748-9326/5/1/014005.

Morgenstern, O., and Coauthors, 2010: Review of present-generation stratospheric chemistry-climate models and associated external forcings. *J. Geophys. Res.*, **115**, D00M02. doi:10.1029/2009JD013728.

Mueller, B., S.I. Seneviratne, C. Jimenez, T. Corti, M. Hirschi, G. Balsamo, P. Ciais, P. Dirmeyer, J.B. Fisher, Z. Guo, M. Jung, F. Maignan, M.F. McCabe, **R.H. Reichle**, et al., 2011: Evaluation of global observations-based evapotranspiration datasets and IPCC AR4 simulations. *Geophys. Res. Letters*, **38**, L06402. doi:10.1029/2010GL046230.

Nearing, G.S., K.R. Thorp, W.T. Crow, M.S. Moran, **R.H. Reichle**, and H.V. Gupta, 2011: Improving DSSAT wheat yield estimates by assimilating observations of soil moisture and leaf area index. *Rem. Sens. Env*. *(submitted)*.

Ott, L., B. Duncan, **S. Pawson**, P. Colarco, M. Chin, C. Randles, T. Diehl, **J.E. Nielsen**, 2010: Influence of the 2006 Indonesian biomass burning aerosols on tropical dynamics studied with the GEOS.5 AGCM. *J. Geophys. Res.*, **115**, D14121. doi:10.1029/2009JD013181.

Ott, L.E., K.E. Pickering, G.L. Stenchikov, D.J. Allen, A.J. DeCaria, B. Ridley, R.-F. Lin, S. Lang, and W.-K. Tao, 2010: Production of lightning NOx and its vertical distribution calculated from three-dimensional cloud-scale chemical transport model simulations. *J. Geophys. Res.*, **115**, D04301. doi:10.1029/2009JD011880.

Ott, L., S. Pawson, and J. Bacmeister, 2011: An analysis of the impact of convective parameter sensitivity on simulated global atmospheric CO distributions. *J. Geophys. Res. (submitted)*.

Putman, W.M., and **M. Suarez**, 2011: Cloud-system resolving simulations with the NASA Goddard Earth Observing System global atmospheric model (GEOS-5). *Geophys. Res. (accepted)*.

Reichle, R.H., S.V. Kumar, **S.P.P. Mahanama**, **R.D. Koster**, **Q. Liu**, 2010: Assimilation of satellite-derived skin temperature observations into land surface models. *J. Hydromet.*, **11**, 1103-1122. doi:10.1175/2010JHM1262.1.

Reichle, R.H., R.D. Koster, G.J.M. De Lannoy, B.A. Forman, Q. Liu, S. Mahanama, and A. Toure, 2011: Assessment and enhancement of MERRA land surface hydrology estimates. *J. Climate (in press)*.

Rienecker, M. M., and Coauthors, 2011: MERRA - NASA's modern-era retrospective analysis for research and applications. *J. Climate*, 24, 3624-3648. doi:10.1175/JCLI-D-11-00015.1.

Roberts J.B., F.R. Robertson, C.A. Clayson, and **M.G. Bosilovich**, 2011: Characterization of turbulent latent and sensible heat flux exchange between the atmosphere and ocean in MERRA, *J. Climate (in*

revision).

Robertson, F. R., **M. Bosilovich**, **J. Chen**, and T. Miller, 2011: The effect of satellite observing system changes on MERRA water and energy fluxes. *J. Climate*. *(in press)*.

Sahoo, A.K., **G.J.M. De Lannoy, R.H. Reichle**, and P. R. Houser, 2011: Assimilation and downscaling of satellite observed soil moisture over the Little River experimental watershed in Georgia, USA. *Adv. Water Res*. *(submitted)*.

Salawitch, R.J., T. Canty, T. Kurosu, K. Chance, Q. Liang, **A. da Silva**, **S. Pawson**, **J.E. Nielsen,** J.M. Rodriguez, P.K. Bhartia, X. Liu, et al., 2010: A new interpretation of total column BrO during Arctic spring. *Geophys. Res. Letters*, **37**, L21805. doi:10.1029/2010GL043798.

Stolarski, R.S., A.R. Douglass, P.A. Newman, **S. Pawson**, M.R. Schoeberl, 2010: Relative contribution of greenhouse gases and ozone-depleting substances to temperature trends in the stratosphere: a chemistry-climate model study. *J. Climate*, **23**, 28-42. doi:10.1175/2009JCLI2955.1.

Schubert, S., H. Wang and **M. Suarez**, 2011: Warm season subseasonal variability and climate extremes in the northern hemisphere: the role of stationary Rossby waves. *J. Climate (in press)*.

Seneviratne**,** S.I**.,** and **R.D. Koster**, 2011: A revised framework for analyzing soil moisture memory in climate data: Derivation and interpretation. *J. Hydromet. (submitted)*.

Shaw, T.A., J. Perlwitz, N. Harnik, P.A. Newman, **S. Pawson**, 2011: The impact of tratospheric ozone changes on downward wave coupling in the Southern Hemisphere. *J. Climate (in press)*.

Strahan, S.E., A.R. Douglass, R.S. Stolarski, H. Akiyoshi, S. Bekki, P. Braesicke, N. Butchart, M.P. Chipperfield, D. Cugnet, S. Dhomse, S.M. Frith, A. Gettelman, S.C. Hardiman, D.E. Kinnison, J.-F. Lamarque, E. Mancini, M. Marchand, M. Michou, O. Morgenstern, T. Nakamura, D. Olivie, **S. Pawson**, G. Pitari, D.A. Plummer, J.A Pyle, R. Rozanov, J. Scinocca, T.G. Shepherd, K. Shibata, D. Smale, H. Teyssedre, W. Tian, Y. Yamashita, 2011: Using Transport Diagnostics to Understand Chemistry-Climate Model Ozone Simulations. *J. Geophys. Res. (in press)*.

Tedesco, M., **R.H. Reichle**, A. Loew, T. Markus, and J. Foster, 2010: Dynamic approaches for snow depth retrieval from spaceborne microwave brightness temperature. *IEEE Trans. Geosci. Rem. Sens.*, **48**, 1955-1967. doi:10.1109/TGRS.2009.2036910.

Trenberth, K. E., R. Dole, Y. Xue, K. Onogi, D. Dee, M. Balmaseda, **M. Bosilovich, S. Schubert,** W. Large, 2010: Atmospheric reanalyses: A major resource for ocean product development and modeling, In Proc. OceanObs'09: Sustained Ocean Observations and Information for Society Conference (Vol. 2), Venice, Italy, 21-25 September 2009, Hall, J., Harrison D.E. and Stammer, D., Eds., ESA Publication WPP-306.

van den Hurk, B., F. Doblas-Reyes, G. Balsamo, **R.D. Koster**, S.I. Seneviratne, H. Camargo Jr, 2010: Soil moisture effects on seasonal temperature and precipitation forecast scores in Europe. *Clim Dyn*. doi: 10.1007/s00382-010-0956-2.

Vinukollu, R., J. Sheffield, E. F Wood, **M.G. Bosilovich**, and **D. Mocko**, 2011: Multi-model analysis of Energy and Water Fluxes: Intercomparisons between Operational Analyses, Land Surface Model and Remote Sensing. *J. Hydromet. (accepted)*.

Wang, H., S. Schubert, M. Suarez, and **R. Koster**, 2010: The physical mechanisms by which the leading patterns of SST variability impact U.S. precipitation. *J. Climate*, **23**, 1815-1836. doi:10.1175/2009JCLI3188.1.

Wang, J., **S. Pawson**, B. Tian, M.-C. Liang, R.-L. Shia, Y.-L. Yung, and X. Jiang**,** 2011: El Niño-Southern oscillation in tropical and mid-latitude column ozone. *J. Atmos. Sci.,* doi:10.1175/JAS-D-11-045.1 *(in press)*.

Wang, J., **S. Pawson**, B. Tian, M.-C. Liang, R-L, Shia, Y.L. Yung, X. Jiang, 2011: El-Niño-

Southern Oscillation in tropical and mid-latitude column ozone. *J. Atmos. Sci. (in press).*

Wargan, K., S. Pawson, I. Stajner, and V. Thouret, 2010: Spatial structure of assimilated ozone in the upper troposphere and lower stratosphere. *J. Geophys. Res.,* **115**, D24316, doi:10.1029/2010JD013941.

Wu, M.-L. C., O. Reale, **S. Schubert**, **M. Suarez**, and C. Thorncroft, 2011: African easterly jet: barotropic instability, waves and cyclogenesis. *J. Climate (accepted).*

Xianan J., D. Waliser, D. Kim, M. Zha, K.R. Sperber, W. Stern, **S.D. Schubert**, G.J. Zhang, W. Wang, M. Khairoutdinov R.B. Neale, M.-I. Lee 2011: Simulation of the intraseasonal variability over the Eastern Pacific ITCZ in climate models. *Clim. Dyn.* doi:10.1007/s00382-011-1098-x *(in press).*

Xue, Y., F. De Sales, W. K.-M. Lau, A. Boone, J. Feng, P. Dirmeyer, Z. Guo, Kyu-Myong Kim, A. Kitoh, V. Kumar, I. Poccard-Leclercq, N. Mahowald, W. Moufouma-Okia, P. Pegion, D.P. Rowell, J. Schemm, **S.D. Schubert**, A. Sealy, W.M. Thiaw, A. Vintzileos, S.F. Williams, **M.-L.C. Wu**, 2010: Intercomparison and analyses of the climatology of the West African Monsoon in the West African Monsoon Modeling and Evaluation project (WAMME) first model intercomparison experiment. *Clim. Dyn.* doi:10.1007/s00382-010-0778-2 *(in press).*

Yang, S.-C., **M. Rienecker**, **C. Keppenne**, 2010: The impact of ocean data assimilation on seasonal-to-interannual forecasts: A case study of the 2006 El Niño event. *J. Climate*, **23**, 4080-4095. doi:10.1175/2010JCLI3319.1.

Yasunari, T. J., **R. D. Koster**, K.-M. Lau, Te. Aoki, Y. C. Sud, T. Yamazaki, H. Motoyoshi, and Y. Kodama, 2011: Influence of dust and black carbon on the snow albedo in the NASA GEOS-5 land surface model. *J. Geophys. Res.*, **116**, D02210. doi:10.1029/2010JD014861 *(in press).*

Yi, Y., J. Kimball, L. Jones, **R. Reichle**, K. McDonald, 2011: Evaluation of MERRA land surface estimates in preparation for the soil moisture active passive mission. *J. Climate (in press).*